Synthesis of Oxide-based Nanoplates and Nanosheets for Photocatalysis and Optoelectronics

A thesis submitted for the award of degree of Doctor of Philosophy at

University of Technology Sydney

Faculty of Science

School of Mathematical and Physical Sciences

By

Somayeh Rafiezadeh

Supervisors

A/Prof. Cuong Ton-That

Dr. Mohammad B. Ghasemian

EM/Prof. Matthew R. Phillips

April 2025

Certificate of Original Authorship

I, Somayeh Rafiezadeh, declare that this thesis, is submitted in fulfilment of the requirements for the award of Doctor of Philosophy, in the School of Mathematical and Physical Sciences at the University of Technology Sydney.

This thesis is wholly my own work unless otherwise referenced or acknowledged. In addition, I certify that all information sources and literature used are indicated in the thesis. This document has not been submitted for qualifications at any other academic institution.

This research is supported by the Australian Government Research Training Program.

Signature: Production Note:
Signature removed prior to publication.

Date: 27/08/2025

Thesis including published works General Declaration

Chapter 4 in the thesis is presented as one published paper in a peer-reviewed journal. The bibliographic details of the work used in this thesis are listed below. The extent of the contribution to the research and all the authors in the paper have been truthfully stated, and the signature from each author has been sought as permission to include the published material in this thesis.

Title: **Enhanced Luminescence and Photocatalytic Activity in Highly Inverted Spinel $ZnGa_2O_4$ Nanoplates**

Somayeh Rafiezadeh, Curtis Irvine, Amar K. Salih, Maedehsadat Mousavi, Matthew R. Phillips, Mohammad B. Ghasemian, and Cuong Ton-That, ACS Applied Nano Materials 2025, 8, 1033-1041.

Status: Publication

My Contribution: Experiments (90%), Manuscript (90%)

Contribution: The project was supervised by C.T.T. and M. B. G. The experiments were carried out by S.R. All the authors contributed to characterization, analyzing the data, and review the paper.

Name of Author	Signature of Author	Date
Somayeh Rafiezadeh	Production Note: Signature removed prior to publication.	04/04/2025
Curtis Irvine	Production Note: Signature removed prior to publication.	31/03/2025
Amar K. Salih	Production Note: Signature removed prior to publication.	28/03/2025
Maedehsadat Mousavi	Production Note: Signature removed prior to publication.	10/07/2025

Matthew R. Phillips	Production Note: Signature removed prior to publication.	27/03/2025
Mohammad B. Ghasemian	Production Note: Signature removed prior to publication.	27/03/2025
Cuong Ton-That	Production Note: Signature removed prior to publication.	07/04/2025

Chapter 5 of the thesis will be submitted to a peer-reviewed journal. The bibliographic details of the work used in this thesis are listed below. The extent of the contribution to the research and all the authors in the paper have been truthfully stated, and the signature from each author has been sought as permission to include the published material in this thesis.

Title: **Bandgap Tuning of β-$(Al_xGa_{1-x})_2O_3$ Nanosheets via Liquid Metal Interface Engineering**

Somayeh Rafiezadeh, Ali Zavabeti, Jianbo Tang, Andrew J. Christofferson, Nastaran Meftahi, Matthew R. Phillips, Kourosh Kalantar-Zadeh, Mohammad B. Ghasemian, and Cuong Ton- That, Advanced Optical Materials. 2025, e01116.

Status: Published

My Contribution: Experiments (90%), Manuscript (95%)

Contribution: The project was supervised by C.T.T. and M. B. G. The experiments were carried out by S.R. All the authors contributed to characterization, analyzing the data, and review the paper.

Name of Author	Signature of Author	Date
Somayeh Rafiezadeh	Production Note: Signature removed prior to publication.	04/04/2025
Ali Zavabeti	Production Note: Signature removed prior to publication.	27/03/2025
Jianbo Tang	Production Note: Signature removed prior to publication.	27/03/2025
Andrew J. Christofferson	Production Note: Signature removed prior to publication.	27/03/2025
Nastaran Meftahi	Production Note: Signature removed prior to publication.	27/03/2025
Matthew R. Phillips	Production Note: Signature removed prior to publication.	27/03/2025
Kourosh Kalantar-Zadeh	Production Note: Signature removed prior to publication.	
Mohammad B. Ghasemian	Production Note: Signature removed prior to publication.	27/03/2025
Cuong Ton-That	Production Note: Signature removed prior to publication.	07/04/2025

Acknowledgments

I would like to express my deepest gratitude to my supervisor, Assoc. Prof. Cuong Ton-That, and Dr. Mohammad B. Ghasemian, whose invaluable guidance and support have been instrumental in producing quality research, conducting laboratory work and preparing publications. I am also grateful to Prof. Matthew R. Phillips for his feedback on my work.

I extend my appreciation to Dr. Ali Zavabeti from RMIT University, Melbourne for his assistance with XPS and EELS characterisation, and to Dr. Jianbo Tang from the University of New South Wales for his technical support in liquid metals synthesis. I also acknowledge Dr. Bruce Cowie at the Australian Synchrotron, Melbourne, for his expertise and support in NEXAFS measurements.

Furthermore, I would like to thank the staff of the Microstructural Analysis Unit (MAU) and the School of Mathematical and Physical Sciences, particularly Fehmida Kanodarwala, Herbert Yuan, Matthew Arnold, and James Bishop, for their technical support with TEM, XRD, SEM, UV-Vis, and AFM.

I am deeply grateful for the financial support provided by UTS, which made my PhD studies in Australia possible.

Finally, my heartfelt thanks go to my beloved family and parents for their moral support, encouragement, and inspiration. Their love and belief in me have been the foundation of my journey, and this dissertation would not have been possible without them.

List of Publications

Refereed journal publications

1. **Somayeh Rafiezadeh**, Ali Zavabeti, Jianbo Tang, Andrew J. Christofferson, Nastaran Meftahi, Matthew R. Phillips, Kourosh Kalantar-Zadeh, Mohammad B. Ghasemian, and Cuong Ton- That, Advanced Optical Materials. 2025, e01116.

2. Somayeh Rafiezadeh, Curtis Irvine, Amar K. Salih, Maedehsadat Mousavi, Matthew R. Phillips, Mohammad B. Ghasemian, and Cuong Ton-That. "Enhanced Luminescence and Photocatalytic Activity in Highly Inverted Spinel ZnGa2O4 Nanoplates" ACS Applied Nano Materials 2025, 8, 1033-1041.

3. Francois-Marie Allioux, Sahar Nazari, Mohammad B. Ghasemian, Ali Zavabeti, Zengxia Pei, Josh Leverett, **Somayeh Rafiezadeh**, Amar K. Salih, Curtis P. Irvine, Mahroo Baharfar, Laetitia Bardet, Moonika S. Widjajana, Yuan Chi, Dorna Esrafilzadeh, Ali R. Jalili, Nima Haghdadi, Jianbo Tang, Kevin J. Laws, Cuong Ton-That, Torben Daeneke, Rahman Daiyan, Md Arifur Rahim, and Kourosh Kalantar-Zadeh. "Atomic Dispersion via High-Entropy Liquid Metal Alloys" *Small Structures*, ***5*****,** (2024), 2400294.

4. Mohammad B. Ghasemian, Ali Zavabeti, Francois-Marie Allioux, Pankaj Sharma, Maedehsadat Mousavi, Md. Arifur Rahim, Jianbo Tang, Andrew J. Christofferson, Nastaran Meftahi, **Somayeh Rafiezadeh**, Pramod Koshy, Chris F. McConville, Salvy P. Russo, Cuong Ton-That, Jan Seidel, Kourosh Kalantar-Zadeh. "Liquid metal doping induced ferroelectricity in two-dimensional materials" *Small*, 2024, 2309924.

Contents

List of Figures

List of Tables

List of abbreviations

AFM	Atomic force microscopy
BL	Blue luminescence
BSE	Back scattered electrons
CL	Cathodoluminescence
DAP	Donor–acceptor pair
DFT	Density function theory
DUV	Deep ultraviolet
E_a	Activation energy
EDS	Energy dispersive spectroscopy
EELS	Electron energy loss spectroscopy
E_F	Fermi level
FWHM	Full width at half maximum
GL	Green luminescence
HRTEM	High-resolution transmission electron microscope
LED	Light emitting diode
MOCVD	Metal-organic chemical vapour deposition
NBE	Near band edge

NEXAFS	Near-edge X-ray absorption fine structure
RL	Red luminescence
RhB	Rhodamine B
SAED	Selected area electron diffraction
SE	Secondary electron
SEM	Scanning electron microscope
TEY	Total electron yield
TFY	Total fluorescence yield
TEM	Transmission electron microscope
UPS	Ultraviolet photoelectron spectroscopy
UV	Ultraviolet
VBM	Valence band maximum
V_O	Oxygen vacancies
XPS	X-ray photoelectron spectroscopy
XRD	X-ray diffraction
YL	Yellow luminescence
$ZnGa_2O_4$	Zinc gallate

Abstract

Gallium oxide (Ga_2O_3) is an emerging ultrawide bandgap semiconductor with strong potential for optoelectronic and power electronic applications. However, its intrinsic n-type conductivity and the challenge of achieving stable p-type doping hinder its suitability for bipolar devices. This motivates the exploration of alternative materials such as $ZnGa_2O_4$, which exhibits both n-type and p-type conductivity, making it strong candidate for next-generation electronics. Additionally, bandgap engineering in Ga_2O_3 alloys is constrained by high- temperature deposition techniques and limited dopant incorporation. To address these challenges, this thesis synthesises $ZnGa_2O_4$ nanoplates via hydrothermal method and investigates the role of native defects, particularly cation site conversion, in tuning luminescence and photocatalytic properties. The second part of this work develops low-temperature synthesis approach for fabricating Al-enriched β-$(Al_xGa_{1-x})_2O_3$ nanosheets, enabling compositional tuning for bandgap engineering without complex fabrication techniques. The effect of Al incorporation on electronic structure, defect formation, and optical properties is examined, providing insights into defect engineering strategies for optimising material performance.

$ZnGa_2O_4$ nanoplates with a pure spinel phase, lateral dimensions up to 10 μm, and thicknesses around 40 nm were synthesized. Photoemission and Raman spectroscopy revealed significant cation inversion, with Ga^{3+} occupying tetrahedral sites (Ga_{Zn}) and Zn^{2+} occupying octahedral sites (Zn_{Ga}), forming anti-site defects. The inversion parameters were 0.36 ± 0.04 (Ga_{Zn}) and 0.25 ± 0.02 (Zn_{Ga}). These nanoplates exhibited stable, bright broadband luminescence, including UV emission at 3.2 eV (self-trapped holes) and three visible defect bands. Furthermore, $ZnGa_2O_4$ nanoplates demonstrated superior photocatalytic efficiency in degrading Rhodamine B (RhB) under ultraviolet A

(UVA) irradiation compared to Ga_2O_3. Band structure analysis revealed strong tail states extending the valence and conduction band edges, reducing the bandgap to 3.9 eV and enhancing hydroxyl radical production.

To address the challenge of compositional tuning at the nanoscale, this thesis investigates low-temperature liquid metal-based synthesis method for selective Al enrichment in β-Ga_2O_3 nanosheets. This approach yielded β-$(Al_xGa_{1-x})_2O_3$ nanosheets with monoclinic crystal structure and dominant (- 201) orientation. The synthesised nanosheets exhibited large lateral dimensions (> 100 μm) and average thickness of 3.2 ± 0.5 nm, making them suitable for nanoscale device applications. By varying the Al content in liquid metal from 0 to 10 at%, bandgap modulation was achieved from 4.5 eV (pure β-Ga_2O_3) to 6.4 eV (β-$(Al_{0.88}Ga_{0.12})_2O_3$). Cathodoluminescence spectroscopy revealed that the β-$(Al_xGa_{1-x})_2O_3$ nanosheets exhibit broadband luminescence, retaining the characteristic self-trapped hole emission of β-Ga_2O_3 around 3.2 eV, while Al incorporation introduces an additional distinct deep-UV emission.

Chapter 1. Overview of the Research Project

1.1. Background

Wide bandgap (WBG) transition metal oxides have attracted growing interest due to their exceptional properties, including bandgaps exceeding 3 eV, high breakdown electric fields, broad optical transparency, and excellent chemical and thermal stability. These features enable reliable device operation under harsh conditions, making them highly promising for deep-ultraviolet (DUV) optoelectronics and high-power electronic applications.[1, 2]. Among WBG oxides, materials such as Ga_2O_3 and its alloys stand out due to their availability as bulk crystals and their potential for bandgap and defect engineering. In particular, gallium oxide (Ga_2O_3) offers a unique combination of a wide bandgap (4.5–4.9 eV), high breakdown electric field (> 8 MV/cm), and robust thermal and chemical stability, positioning it as a key material for next-generation semiconductor technologies [3, 4] However, despite these advantages, Ga_2O_3 faces some major challenges that limit its widespread application: (i) its inherent n-type conductivity and the difficulty of achieving p-type doping due to deep acceptor levels (>1 eV above the valence band for most dopants) and self-trapping of holes, which restrict its potential in homojunction bipolar devices such as light-emitting diodes (LEDs) and transistors [5-7] and (ii) limited bandgap engineering in Ga_2O_3 alloys using conventional methods, which involve complex high-temperature deposition techniques and constrain dopant incorporation.

To address the first challenge, $ZnGa_2O_4$ has been explored as a potential alternative due to its tuneable conductivity, which can switch between n-type and p-type conductivity depending on synthesis conditions. [8, 9] Unlike Ga_2O_3, which naturally exhibits inherent n-type conductivity, $ZnGa_2O_4$ offers greater flexibility in electrical

properties, making it a strong candidate for next-generation electronic applications. In addition, $ZnGa_2O_4$ exhibits high chemical stability and enhanced optical properties, including multi-wavelength emission. [10] However, the role of native defects, particularly cation anti-site defects (Ga_{Zn} and Zn_{Ga}), in the electronic and optical performance of $ZnGa_2O_4$'s is not fully understood. Anti-site defects, arising from the inversion of Zn^{2+} and Ga^{3+} ions between tetrahedral and octahedral sites, introduce localized electronic states within the bandgap and can significantly affect the material's conductivity, optical emissions, and photocatalytic efficiency. While theoretical studies suggest that these defects, such as Ga_{Zn} and Zn_{Ga}, influence the electronic structure and charge carrier dynamics, [11] their exact impact on the material's performance remains unclear. Furthermore, the relationship between defect states and the photocatalytic activity of $ZnGa_2O_4$ has not yet to be fully explored. Therefore, understanding the role of the anti-site defects is essential for optimizing $ZnGa_2O_4$'s photocatalytic performance.

The second challenge is achieving bandgap engineering through compositional tuning, which restricts its versatility in optoelectronic applications. Bandgap engineering is crucial for tailoring the material's electronic and optical properties, particularly for deep-UV applications. [12] One effective approach to overcoming this limitation is alloying Ga_2O_3 with Al_2O_3, resulting in $(Al_xGa_{1-x})_2O_3$, which expands the bandgap range beyond that of pure Ga_2O_3 (4.5 eV), enabling a wider range of applications. [13] Density functional theory (DFT) calculations predict that the monoclinic β-phase of $(Al_xGa_{1-x})_2O_3$ remains stable up to 71% Al incorporation. [14] However, experimentally achieving high Al content while maintaining the β-phase structure has proven challenging. Conventional methods such as molecular beam epitaxy (MBE) and metal-organic chemical vapor deposition (MOCVD) achieving only 48% and 61% Al incorporation, respectively. [15-17] These techniques require high-temperature and complex vacuum-based deposition conditions,

limiting scalability and hindering further bandgap tuning. [16, 17] To address these limitations, liquid metal-based synthesis has emerged as a promising alternative due to its ability to produce β-$(Al_xGa_{1-x})_2O_3$ nanosheets with controlled Al content at low temperatures and without the need for vacuum environments. Liquid metals, such as gallium and its alloys, spontaneously form self-limiting oxide layers on their surfaces under ambient conditions. These surface oxides can be exfoliated to yield two-dimensional nanosheets with tuneable composition and thickness [18]. This approach offers a scalable, low-cost, and efficient route for synthesizing high-purity β-$(Al_xGa_{1-x})_2O_3$ with tailored electronic and optical properties. Given these advantages, liquid metal-based synthesis serves as a core methodology throughout this work. Furthermore, while defects and self-trapped hole states in Ga_2O_3 have been extensively studied, their impact in high-Al-content β-$(Al_xGa_{1-x})_2O_3$ remains insufficiently explored. Understanding these defect-related electronic transitions is essential for optimizing the material's properties for high-performance optoelectronic and power device applications.

1.2. Aims of the project

This research aims to investigate the synthesis, structural properties, and optical and electronic behaviour of $ZnGa_2O_4$ nanoplates and β-$(Al_xGa_{1-x})_2O_3$ nanosheets. The key objectives of this work are:

- Develop a hydrothermal method to grow $ZnGa_2O_4$ nanoplates with controlled morphology and chemical composition.
- Investigate the effects of anti-site defects in $ZnGa_2O_4$ nanoplates on optical, electronic, and photocatalytic properties.
- Develop a low-temperature liquid metal-based synthesis method to exfoliate β-$(Al_xGa_{1-x})_2O_3$ nanosheets with controllable Al incorporation.

- Investigate the effect of Al incorporation on the electronic band structures of β-$(Al_xGa_{1-x})_2O_3$ nanosheets.

By achieving these objectives, this research contributes to the fundamental understanding of $ZnGa_2O_4$ nanoplates and β-$(Al_xGa_{1-x})_2O_3$ nanosheets, paving the way for their implementation in next-generation optoelectronic and energy applications. The findings will provide valuable insights into the role of native defects, bandgap modulation, and scalable synthesis methods for advanced semiconductor technologies.

1.3. Thesis Layout

The thesis is organised into six chapters as outlined below.

Chapter 1: Background and Motivation

This chapter provides an overview of the PhD project, including $ZnGa_2O_4$ and $(Al_xGa_{1-x})_2O_3$ nanoplates and nanosheets. The background, motivation and objectives are briefly discussed.

Chapter 2: Ga_2O_3-based Materials and Alloys: Theoretical Background and Literature Review

This chapter provides a comprehensive overview of Ga_2O_3-based materials, including $ZnGa_2O_4$ and β-$(Al_xGa_{1-x})_2O_3$, their properties, synthesis methods, and optical characteristics, focusing on intrinsic defects, optical properties, and bandgap engineering.

Chapter 3: Experimental Details

This chapter outlines the main experimental techniques employed in this project, including the hydrothermal method and a low-temperature liquid metal-based synthesis method.

Chapter 4: Enhanced Luminescence and Photocatalytic Activity in Highly Inverted Spinel $ZnGa_2O_4$ Nanoplates

This chapter investigates the synthesis of inverted $ZnGa_2O_4$ nanoplates via hydrothermal method. It examines the role of anti-site defects in enhancing the luminescence and photocatalytic performance of the $ZnGa_2O_4$.

Chapter 5: Bandgap Engineering of β-$(Al_xGa_{1-x})_2O_3$ Nanosheets Derived from Liquid Metals Interface

This chapter investigates the synthesis of β-$(Al_xGa_{1-x})_2O_3$ nanosheets via a liquid metal-based approach, focusing on Al incorporation and its effect on bandgap modulation. The structural, optical, and electronic properties are analysed to understand their suitability for high-power and deep-UV applications.

Chapter 6: Conclusions and outlook

This chapter presents the summary of the key findings of the research and provide suggestions for future research directions.

Chapter 2. Ga_2O_3-Based Materials: Synthesis, Properties, and Applications

Chapter 2 provides a comprehensive literature review of wide-bandgap oxide semiconductors relevant to this thesis, namely β-Ga_2O_3, $ZnGa_2O_4$, and β-$(Al_xGa_{1-x})_2O_3$ alloys. These materials have attracted increasing interest due to their promising optical, electronic, and photocatalytic properties, particularly in the context of deep-UV optoelectronics, power electronics, and environmental remediation. This chapter begins by examining the crystallographic and electronic structure of β-Ga_2O_3, followed by an overview of the spinel $ZnGa_2O_4$ and its defect-driven behavior. It also explores the bandgap engineering potential of β-$(Al_xGa_{1-x})_2O_3$ alloys and the emerging role of liquid metal-based synthesis routes. The chapter aims to contextualize the experimental work presented in subsequent chapters by summarizing the state-of-the-art research, highlighting knowledge gaps, and identifying how the synthesis and characterization techniques used in this thesis contribute to the development of next-generation oxide semiconductors.

2.1. Properties and Applications of Ga_2O_3

Gallium oxide (Ga_2O_3), an ultrawide bandgap (UWBG) semiconductor with a bandgap ranging from 4.6 to 4.9 eV at room temperature and a high electric breakdown field (> 8 MV/cm). These properties make it a strong candidate for a variety of applications, including high-power electronics (e.g., field-effect transistors and Schottky barrier diodes), optoelectronic devices (e.g., solar-blind photodetectors, electroluminescent components), and phosphors. Additionally, Ga_2O_3 has been widely investigated for gas sensing, DUV transparent electrodes, and photocatalysis due to its wide bandgap and chemical stability. [19-23]

Ga_2O_3 exists in five polymorphic forms—α, β, γ, δ, and ϵ—with the β-phase being the most thermodynamically stable, both chemically and structurally, both chemically and thermally, up to its melting point of 1800 °C. β-Ga_2O_3 can be obtained by annealing any other polymorphs of Ga_2O_3 at temperatures above 500 -700 °C, as shown in Figure 2.1. [12] This transformation pathway is important for phase control during synthesis. This phase transition pathway supports scalable production of the β-phase and allows tuning of structural features relevant to material stability and functional properties. The primary structural characteristics of each Ga_2O_3 polymorph, along with their experimentally obtained lattice parameters, are summarized in Table 2.1.

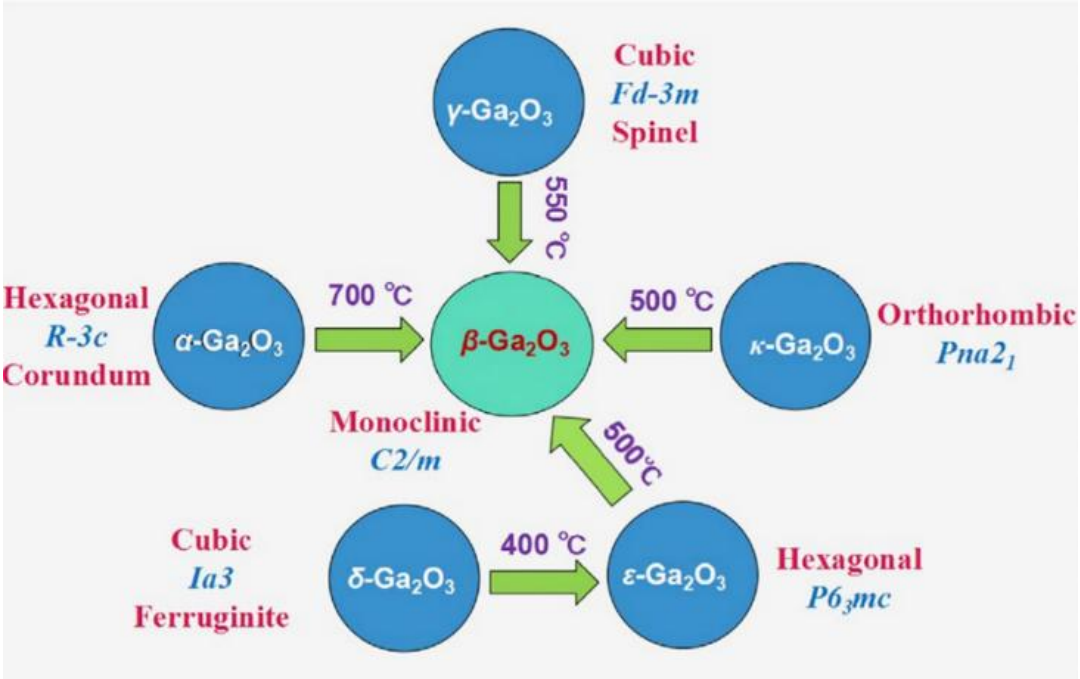

Figure 2.1. Interconversion relationships among Ga_2O_3 polymorphs. [12]

Table 2.1. Structural characteristics and lattice parameters of the five phases of Ga_2O_3: α, β, γ, δ, and ϵ. [12]

Polymorph	Structure	Space Group	Lattice Parameter
α	Hexagonal	*R*3̄c	*a* = *b* = 4.98 Å, *c* = 13.43 Å, *α* = *β* = 90°, *γ* = 120°
β	Monoclinic	*C2/m*	*a* = 12.23 Å, *b* = 3.04 Å, *c* = 5.80 Å, *α* = *γ* = 90°, *β* = 103.8°
γ	Cubic	*Fd*3̄m	*a* = *b* = *c* = 8.24 Å, *α* = *β* = *γ* = 90°
δ	Cubic	*Ia3*	*a* = *b* = *c* = 9.52 Å, *α* = *β* = *γ* = 90°
ε	Hexagonal	*P63mc*	*a* = *b* = 2.90 Å, *c* = 9.26 Å, *α* = *β* = 90°, *γ* = 120°
κ	Orthorhombic	*Pna2₁*	*a = 5.05 Å, b = 8.70 Å, c = 9.28 Å, α = β = γ = 90°*

The crystal structure of β-Ga_2O_3 is monoclinic (space group C_2/m) with a base- centered unit cell containing 20 atoms. It comprises two crystallographically inequivalent gallium sites: Ga(I), which is tetrahedrally coordinated, and Ga(II), which is octahedrally coordinated. Additionally, it features three distinct oxygen sites: O(I), O(II), and O(III), as illustrated in Figure 2.2. These unique coordination environments influence the material's electrical and optical behavior, particularly through the formation of native defects such as oxygen vacancies and self-trapped holes, which can impact its conductivity, photoconductivity, and luminescence characteristics. [24]

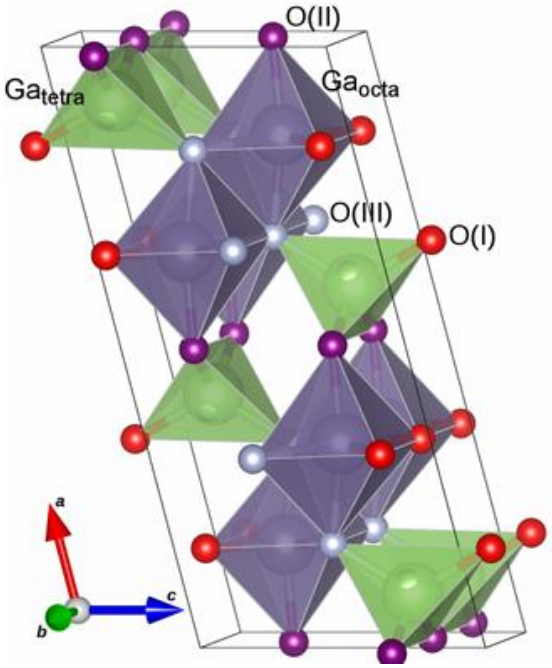

Figure 2.2. The monoclinic β-Ga_2O_3 unit cell shows two inequivalent Ga sites: a tetrahedral Ga(I) site and an octahedral Ga(II) site, along with three inequivalent O sites. [24]

2.2. Optical Properties of Ga_2O_3

β-Ga_2O_3 is a wide-bandgap semiconductor with a fundamental indirect bandgap of ~4.7–4.8 eV, and a closely spaced direct transition approximately 0.1 eV higher, as established by theoretical calculations and optical studies. [25, 26] Its luminescence properties are strongly influenced by intrinsic (native defects) and extrinsic defects, including vacancies, interstitials, and deep-level defects. Unlike typical semiconductors, β-Ga_2O_3 does not exhibit near-bandgap emission. Instead, its cathodoluminescence (CL) spectrum exhibits a peak near 3.4 eV. [27]

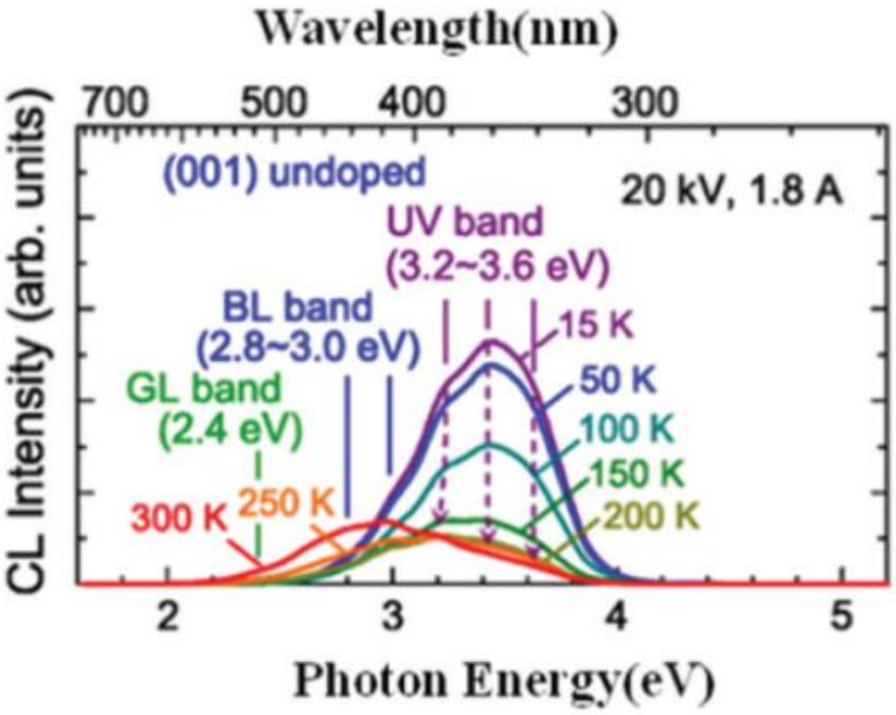

Figure 2.3. Temperature-dependent cathodoluminescence (CL) spectra of (001) undoped β-Ga_2O_3 crystal samples, showing a decrease in UV luminescence with increasing temperature. [28]

Figure 2.3 illustrates the cathodoluminescence (CL) spectra of β-Ga_2O_3 single crystals, revealing three primary emission bands: ultraviolet luminescence (UV, 3.2–3.6 eV), blue luminescence (BL, 2.8–3.0 eV), and green luminescence (GL, 2.4 eV). The UV emission is attributed to the recombination of free electrons and self-trapped holes (STHs). The BL emission is linked to donor-acceptor pair (DAP) transitions, which involve deep-level donors and acceptors. Potential donors include intrinsic defects such as oxygen vacancies (V_O) and interstitial gallium (Ga_i), while acceptors may include gallium vacancies (V_{Ga}) and V_O-V_{Ga} complexes. The green emission (2.4 eV) is primarily associated with oxygen vacancies (V_O). [28-30] Thus, deep-level defects, particularly oxygen and gallium vacancies, can play a crucial role in determining the emission properties of β-Ga_2O_3. In addition, the CL spectrum of β-Ga_2O_3 single crystals is influenced by temperature, as shown in Figure 2.3. At lower temperatures, the UV band is more

prominent in undoped β-Ga_2O_3 single crystals. However, as the temperature increases, the intensity of the UV band decreases. In contrast, the intensities of the GL and BL bands gradually increase relative to the UV band, which may be attributed to enhanced recombination processes involving deep-level defects at elevated temperatures. [28] In the following section, various defects in β-Ga_2O_3, including vacancies, interstitial, and deep-level defects, will be discussed in detail.

2.2.1. Self-Trapped Holes (STHs)

In β-Ga_2O_3, self-trapped holes (STHs) originate from lattice distortions that confine them to specific oxygen atoms rather than allowing delocalization throughout the crystal. [31] This phenomenon is also observed in other wide-bandgap oxides such as SnO_2 and In_2O_3.[32] As a result, the wave function of STHs remains confined near oxygen atoms, as illustrated in Figure 2.4, which has been confirmed using techniques like deep-level transient spectroscopy (DLTS) and deep-level optical spectroscopy (DLOS). [32, 33]

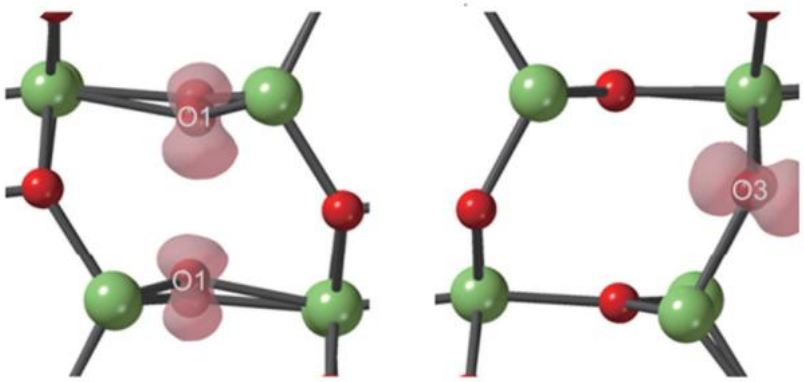

Figure 2.4. Optimized atomic configurations and iso-surfaces of the squared wave functions for self-trapped holes (STHs) at the O1 and O3 sites in β-Ga_2O_3. [33]

When β-Ga_2O_3 is excited with photons having energy greater than its bandgap, electron-hole pairs are generated (Figure 2.5). Due to strong electron-lattice interactions, holes in the lattice become self-trapped, leading to lattice distortions. As a result, lower-

energy emissions can occur when conduction band electrons recombine with self-trapped holes (STHs). Additionally, if an electron becomes Coulombically bound to an STH, a self-trapped exciton (STE) may form at low temperatures, further reducing the emission energy by an amount corresponding to the exciton binding energy. Studies on wide-bandgap oxides indicate that β-Ga_2O_3 exhibits both the highest self-trapping energy (E_{ST}) and the lowest barrier to trapping energy (E_B), suggesting that hole self-trapping occurs instantaneously, which aligns with experimental findings. [29, 34] These self-trapped holes (STHs) play a critical role in determining the optical and electronic behavior of β-Ga_2O_3. In particular, they are associated with broad sub-bandgap luminescence and can act as recombination centers that reduce carrier mobility in optoelectronic devices. Understanding STH behavior is therefore essential for interpreting emission features and improving the performance of Ga_2O_3-based LEDs, detectors, and photocatalysts.

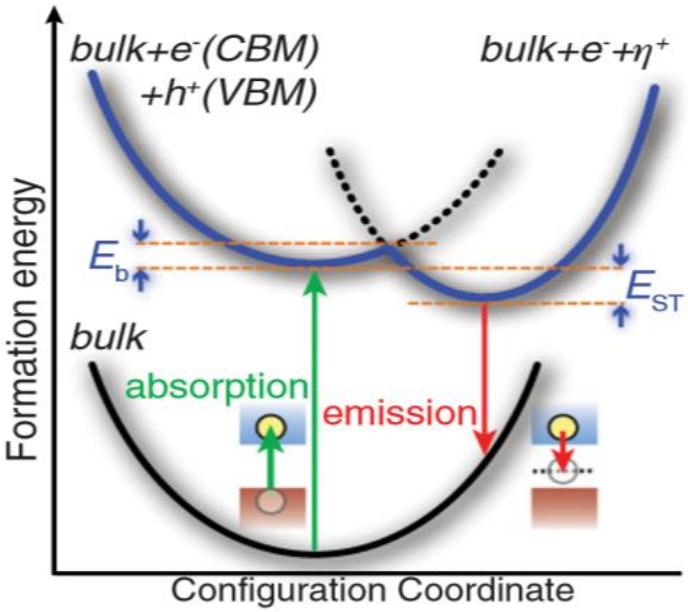

Figure 2.5. A schematic illustrating the self-trapping process, where EB represents the trapping barrier and EST denotes the self-trapping energy. [34]

2.2.2. Oxygen Vacancy (V_O)

N-type conductivity is a well-known characteristic of many wide bandgap oxides, typically attributed to native donor defects such as oxygen vacancies or metal interstitials. In β-Ga_2O_3, oxygen vacancies (V_O) have been widely studied due to their potential role in conductivity and optical properties, although their exact contribution to free electron generation remains under debate. Under stoichiometric conditions, β-Ga_2O_3 is an insulator, but deviations in oxygen stoichiometry, such as oxygen deficiency or excess, can lead to the formation of V_O or oxygen interstitials (O_i), respectively. [35, 36] V_O and O_i can act as donor or acceptor centres, respectively, thus altering conductivity of β-Ga_2O_3 as shown in Figure 2.6. [37]

β-Ga_2O_3 has high conductivity at a low O_2 flow rate, and it decreases with increasing O_2 content. Therefore, the conductivity of β-Ga_2O_3 depends on the O_2 content in the atmosphere, which is linked to the concentration of oxygen vacancies (V_O) in.

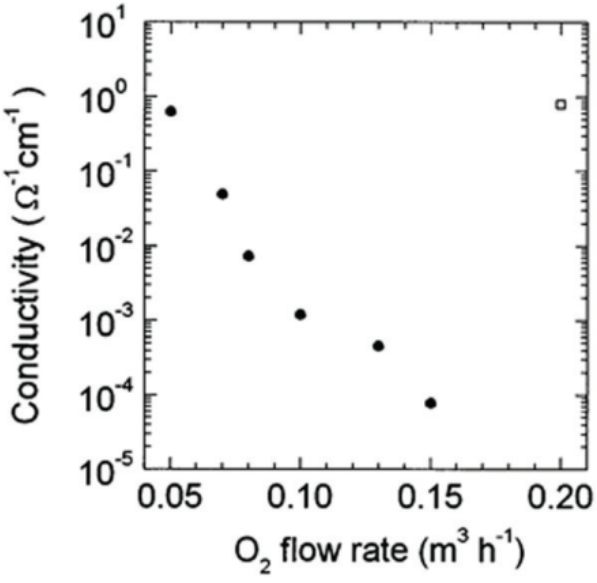

Figure 2.6. The relationship between the electrical conductivity of β-Ga_2O_3 single crystals along the b axis and the O_2 flow rate during the crystal growth. [37]

In addition, the conductivity of the as-grown Ga_2O_3 film is particularly sensitive to the O_2 content in the annealing atmosphere. Films annealed in oxygen-poor environments (e.g., nitrogen or vacuum) exhibit higher V_O concentrations and increased conductivity, while oxygen-rich conditions result in lower conductivity due to reduced V_O concentrations. [38, 39] The underlying mechanism involves oxygen vacancies (V_O) capturing two electrons to maintain a neutral state. In β-Ga_2O_3, oxygen vacancies (V_O) can be ionized—transitioning from a neutral to a singly or doubly charged state—releasing one or two free electrons into the conduction band. This process enables β-Ga_2O_3 to generate excess electrons, making it an electron-rich oxide. Consequently, β-Ga_2O_3 exhibits conductivity when annealed in an oxygen-deficient atmosphere.

It has been shown that V_O defects can form deep-level states located more than 1 eV below the conduction band minimum (CBM), which do not contribute to an increase in electron concentration. [36, 40] Studies have shown that V_O defects can transition from neutral to ionized states, forming deep-level defects that influence optical properties, but are less effective as donors for n-type conductivity. [41, 42] Despite their impact on conductivity, the role of V_O as the primary source of n-type conductivity remains uncertain, as deep-level defects are too far from the conduction band to significantly affect electron flow under typical conditions.

2.2.3. Gallium Vacancy (V_{Ga})

Gallium vacancies (V_{Ga}) are p-type acceptor defects that theoretically form under oxygen-rich growth conditions. The formation energy and defect levels of V_{Ga} was reported by DFT calculation, as shown in Figure 2.7a, b. [43] Theoretically, V_{Ga} could promote p-type behaviour in β-Ga_2O_3 by shifting the Fermi level closer to the valence band. However, the high formation energy of V_{Ga} makes its occurrence rare, and β-Ga_2O_3 typically remains n-type due to the presence of oxygen vacancies (V_O). In oxygen-poor

(gallium-rich) conditions, gallium interstitials (Ga_i) act as shallow donors, compensating for unintentional doping and reducing V_{Ga} concentrations, thus maintaining n-type conductivity. While V_{Ga} could theoretically promote p-type conductivity, its high formation energy and the presence of Ga_i prevent its significant effect, making it a minor factor in the material's electronic properties. [43]

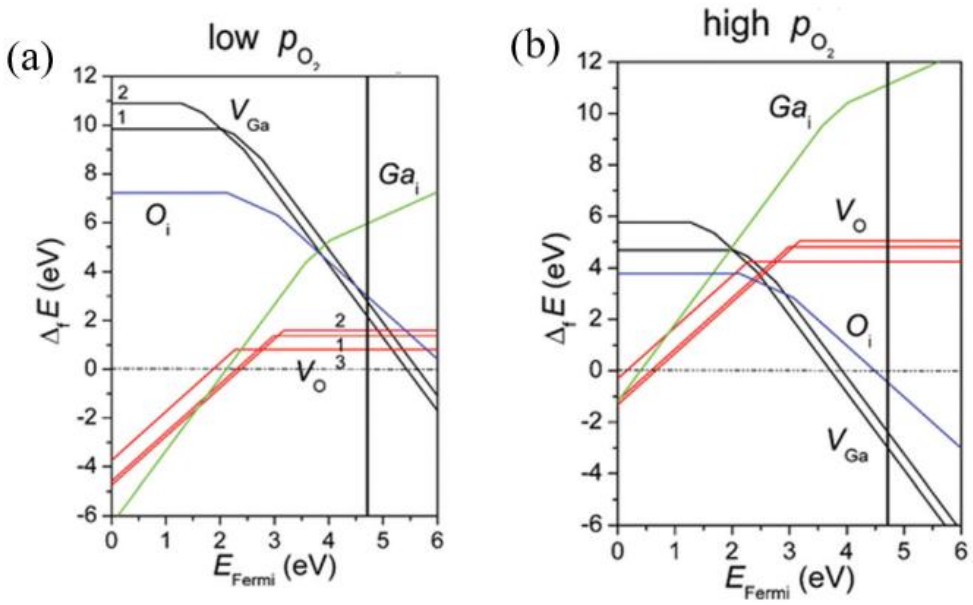

Figure 2.7. Formation energies of V_{Ga} point defects in β-Ga_2O_3 as a function of Fermi energy under (a) oxygen-poor and (b) oxygen-rich conditions. [43]

2.2.4. Oxygen and Gallium Interstitials (Oi and Gai)

Oxygen interstitials (O_i) and gallium interstitials (Ga_i) act as acceptors and donors, respectively. However, their high formation energies result in low concentrations, making their effects on optical properties limited. While their influence on optical characteristics is minimal, they can contribute to complex defect interactions under specific growth conditions. [36, 43]

2.3. $ZnGa_2O_4$ Nanostructures

Zinc gallate ($ZnGa_2O_4$) is an ultra-wide bandgap semiconductor with an optical bandgap ranging from 4.6 to 5.2 eV and a high breakdown voltage, making it a promising material for light-emitting and power electronic devices. [44-46] It exhibits a high carrier concentration of 9×10^{19} cm^{-3}, a room-temperature electron mobility of 102 $cm^2/V \cdot s$, and a high dielectric constant of 10.4, along with a large breakdown voltage. $ZnGa_2O_4$ is an alloy of Ga_2O_3 and ZnO, crystallizing in a normal cubic spinel structure (Fd-3m space group), which is one of the new transparent and semiconductor materials. [47-49] In normal spinels, Zn^{2+} and Ga^{3+} cations occupy tetrahedral and octahedral sites, respectively, with a lattice parameter of 8.3342 Å , as shown in Figure 2.8. [50] However, $ZnGa_2O_4$, like other spinel compounds, can exhibit an inverted cation distribution due to the partial exchange of Ga and Zn ions between the tetrahedral and octahedral sites. This leads to a partial inverse spinel structure, where both divalent Zn^{2+} and trivalent Ga^{3+} cations are present on both tetrahedral and octahedral sites.

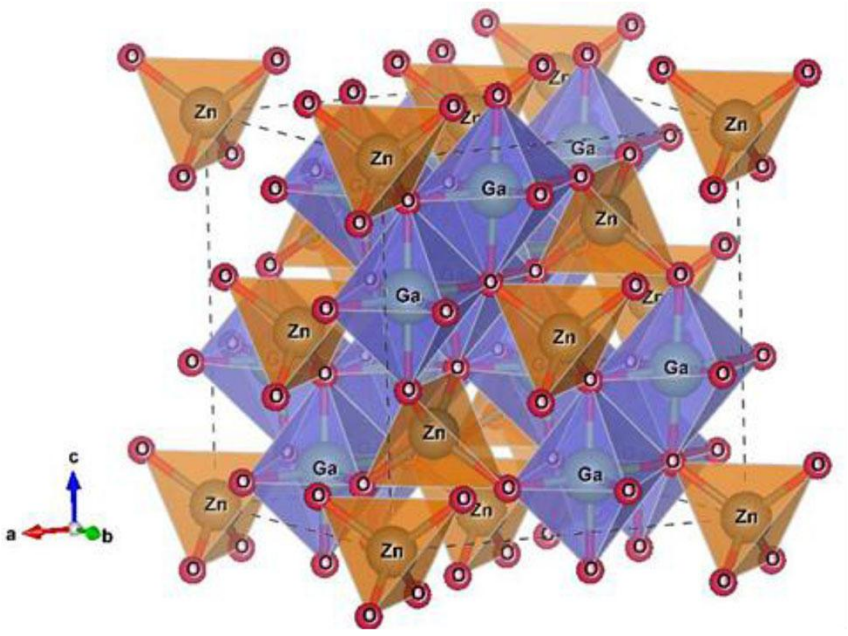

Figure 2.8. Normal spinel structure of $ZnGa_2O_4$ that Zn^{2+} cations occupy tetrahedral sites and Ga^{3+} cations occupy octahedral sites. [51]

2.3.1. Optical Properties of $ZnGa_2O_4$

$ZnGa_2O_4$, with its wide bandgap of approximately 5 eV, is a promising material for optoelectronic and photocatalytic applications. [45] Its optical and electronic properties are strongly influenced by intrinsic defects, including oxygen vacancies, anti-site defects, and self-trapped holes, which introduce localized states within the bandgap. These defects play a critical role in photoluminescence (PL), cathodoluminescence (CL), and other optical responses, significantly impacting emission spectra and luminescence efficiency.

While extensive research has been conducted on transition metal-doped $ZnGa_2O_4$ (e.g., Cr, Mn, and Eu doping) for phosphor applications, its intrinsic defect structure remains less explored. Point defects such as vacancies (V_O, V_{Zn}, V_{Ga}), anti-sites (Ga_{Zn}, Zn_{Ga}), and interstitials (Zn_i, Ga_i, O_i) are essential in shaping the material's optical characteristics and electronic behaviour. [52] In its ordered-normal spinel structure, Zn and Ga cations occupy tetrahedral (T_t) and octahedral (O_p) sites, respectively. However, variations in synthesis conditions can induce cation disorder, leading to anti-site defects, which significantly modify the conductivity and optical response of $ZnGa_2O_4$, as shown in Figure 2.9. [53]

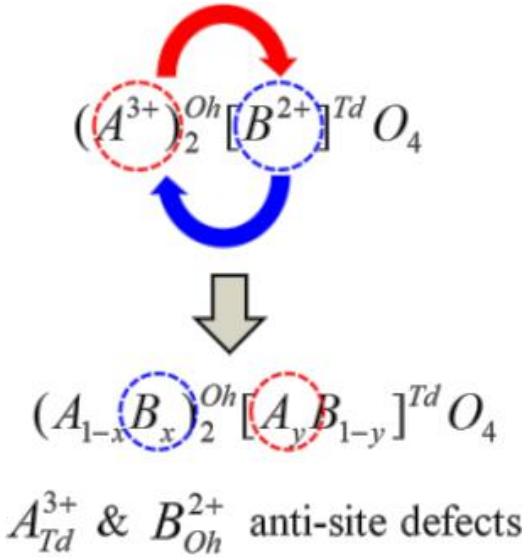

Figure 2.9. A diagram illustrating the exchange of cations leading to the formation of anti-site defects. [53]

Photoluminescence studies indicate that oxygen vacancies (V_O) and anti-site defects (Zn_{Ga} and Ga_{Zn}) strongly influence the emission spectra, making $ZnGa_2O_4$ a strong candidate for UV-emitting applications. Understanding these defect-induced effects is crucial for optimizing the material's performance in LEDs, photocatalysis, and other optoelectronic devices.

2.3.1.1. Oxygen Vacancy (V_O)

Oxygen vacancies (V_O) are significant intrinsic defects in $ZnGa_2O_4$ that strongly influence its optical, electronic, and photocatalytic properties. These vacancies create deep-level states within the bandgap, and they are unlikely to contribute to unintentional n-type conductivity. Instead, they lead to noticeable emissions in the visible to near-infrared region, particularly around 1.7 eV, as observed in CL studies. [54, 55] V_O defects typically form under oxygen-deficient conditions, such as during high-temperature synthesis or in reducing atmospheres. Their formation energy is highly sensitive to the local oxygen chemical potential. Density functional theory (DFT) simulations, as well as

experimental studies, have linked V_O defects to blue luminescence in $ZnGa_2O_4$, underscoring their role in shaping the material's luminescent properties. Controlling the concentration and distribution of these vacancies is therefore crucial for optimizing $ZnGa_2O_4$ for applications in optoelectronics and photocatalysis. [9, 52]

2.3.1.2. Gallium Anti-site Defects (Ga_{Zn})

The Ga anti-site defect (Ga_{Zn}) occurs when Ga atoms occupy Zn sites at tetrahedral sites within the crystal structure of $ZnGa_2O_4$. This substitution introduces localized states within the bandgap, influencing both the electronic and optical properties of the material. [56] A emission peak around 2.32 eV, observed in CL spectra, has been attributed to the Ga_{Zn}, indicating its role in defect-related luminescence. [57] Theoretical studies indicate that Ga_{Zn} defects exhibit the lowest formation energy among intrinsic donor defects under both oxygen-rich and oxygen-poor conditions. [52] The low formation energy of Ga_{Zn} has been experimentally measured to facilitate high Ga incorporation in tetrahedral sites. [8, 9, 58] When the Ga/Zn ratio is greater than the stoichiometric value (Zn/Ga < 1/2), Ga_{Zn} defects form preferentially, leading to unintentional n-type conductivity. This self-doping effect has been observed in $ZnGa_2O_4$ thin films, with reported conductivity reaching $\sigma = 1.78 \times 10^2$ S/cm. [52, 59]

2.3.1.3. Zinc Anti-site Defects (Zn_{Ga})

The Zn anti-site defect (Zn_{Ga}) occurs when Zn atoms occupy Ga sites within the crystal structure of $ZnGa_2O_4$. This defect introduces localized states within the bandgap, affecting the material's electronic and optical properties. [56] Zn_{Ga} defects primarily form under Zn-rich synthesis conditions, but their formation energy is generally higher than that of Ga_{Zn} anti-sites, making them less prevalent. Zn_{Ga} acts as an intrinsic acceptor, capturing free electrons and compensating for n-type conductivity, potentially reducing electrical conductivity. Under oxygen-rich conditions, Zn_{Ga} and Zn vacancies (V_{Zn}) have

the lowest formation energies, making them dominant acceptor defects. Their presence counteracts unintentional n-type doping, but hole transport remains limited due to polaron formation, which inhibits effective charge carrier mobility. [52] Additionally, Zn_{Ga} defects introduce deep-level states, contributing to broad luminescence peaks and modifying the material's optical absorption.[8, 9, 58] Zn_{Ga} acts as an intrinsic acceptor, compensating for n-type conductivity by capturing free electrons and potentially reducing electrical conductivity.

2.3.1.4. Self-Trapped Holes (STHs)

Self-trapped holes (STHs), previously discussed in the context of β-Ga_2O_3, are also relevant in $ZnGa_2O_4$ and play a distinct role in its optical behavior. Self-trapped holes (STHs) are localized charge carriers that significantly impact the luminescence properties of $ZnGa_2O_4$. These states influence recombination processes and contribute to emission features distinct from those arising from vacancies and anti-site defects. The presence of STHs alters both the intensity and lifetime of luminescence, affecting the material's optical and photocatalytic performance. Small hole polarons in $ZnGa_2O_4$ produce ultraviolet light with a photon energy around 3.18 eV corresponding to localized states within the bandgap caused by hole self-trapping. [52]

2.3.2. Hydrothermal Synthesis of $ZnGa_2O_4$ Nanostructures

Hydrothermal synthesis is a highly effective method for producing spinel $ZnGa_2O_4$ nanostructures, enabling precise control over morphology, structure, and properties, which enhances their suitability for a range of applications. The first reports on hydrothermal synthesis of $ZnGa_2O_4$ nanostructures emerged in the late 1990s and early 2000s, with Li et al. proposing a self-regulating hydrothermal reaction to synthesize nanocrystalline $ZnGa_2O_4$. [60] In this process, Ga was dissolved in hydrochloric acid to

form a $GaCl_3$ aqueous solution as a source of Ga^{3+} ions, and zinc powder was used as a source of Zn^{2+} ions. These were placed into a Teflon-lined hydrothermal reactor and maintained at 150 °C for 10 hours.

The hydrothermal synthesis of $ZnGa_2O_4$ is highly sensitive to various parameters that significantly influence the resulting particle size, morphology, crystallinity, and composition. Key synthesis factors include temperature, time, solution pH, cation concentration, and the ZnO/Ga_2O_3 molar ratio. These variables control the morphology of $ZnGa_2O_4$ particles, which can range from cubic nanoparticles to elongated rods, depending on conditions. Typically, higher temperatures and longer reaction times promote larger crystallite sizes and more defined structures. [49, 61]

The precursor concentrations and the ZnO/Ga_2O_3 ratio play crucial roles in determining morphology, stoichiometry, and stability of $ZnGa_2O_4$ nanostructures. Lower precursor concentrations have been reported to favour the formation of ultrafine nanoplatelets. [62] Additionally, substitution of cations can induce structural transformations, as observed in other spinel materials like $Ni_{1-x}Cu_xFe_2O_4$, where increasing Cu content shifts the structure from inverse to mixed spinel. [63]

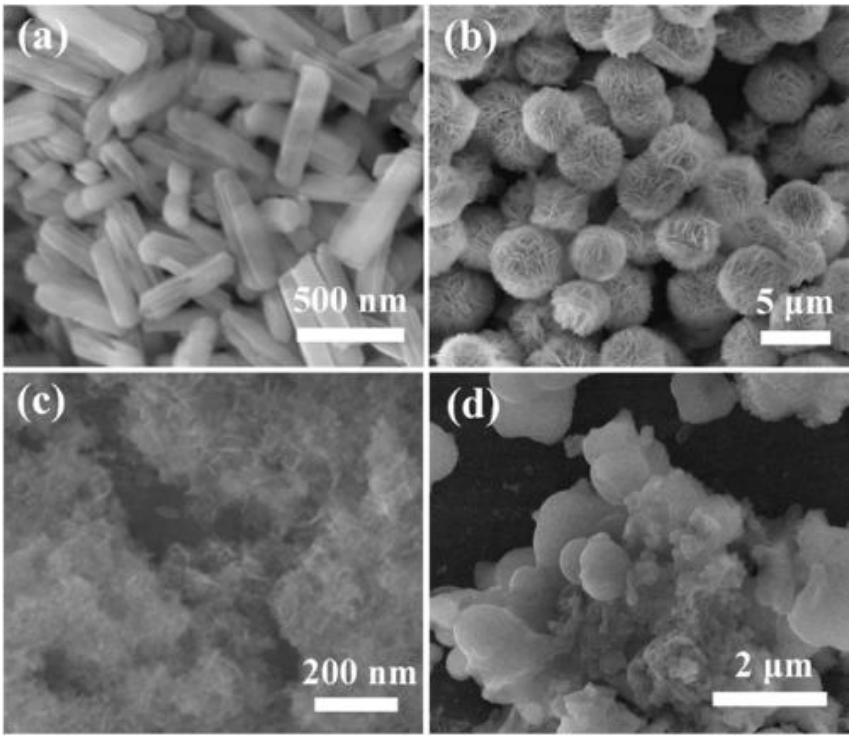

Figure 2.10. FE-SEM images of the products synthesized using various solvents: (a) pure water as the solvent; (b) V_{en}/V_{water} volume ratio of 1:4; (c) V_{en}/V_{water} volume ratio of 1:1; (d) pure En as the solvent. [64]

The pH of the solution is also critical in defining particle morphology and composition. [49] Ethylenediamine (en) has been effectively used as a structure-directing agent, with studies showing that varying the en-to-water ratio (V_{en}/V_{water}) systematically alters $ZnGa_2O_4$ morphology. A water-only solvent yields monodisperse GaOOH nanorods, while adding en at different ratios to water results in dramatic changes: a 1:4 en-to-water ratio forms large $ZnGa_2O_4$ nanosheet-based microcrystals; a 1:2 ratio yields well-defined nanosheet microstructures; and a 1:1 ratio produces smaller, aggregating nanoplates. Pure en as the solvent, however, leads to irregular particle formation, as shown in Figure 2.10. [64] Adjustments in pH, such as through the addition of aqueous ammonia, have also been used to control the formation of spinel $ZnGa_2O_4$ particles.

By carefully tuning these parameters, $ZnGa_2O_4$ nanostructures with controlled properties and uniform spinel structures can be obtained, making hydrothermal synthesis highly adaptable to specific application requirements. While stoichiometric $ZnGa_2O_4$ can be produced through optimized synthesis, the fabrication of inverted spinel $ZnGa_2O_4$, with Ga^{3+} and Zn^{2+} ions distributed across both octahedral and tetrahedral sites, has yet to be achieved and remains an ongoing challenge.

To contextualize the selection of hydrothermal synthesis for $ZnGa_2O_4$ nanostructures, a comparative analysis of alternative synthesis techniques is presented in Table 2.2. This table evaluates hydrothermal synthesis alongside other commonly reported methods, including sol-gel, chemical vapor deposition (CVD), metal–organic CVD (MOCVD), and atomic layer deposition (ALD) [61, 65-68]. Each method is compared based on reaction temperature, morphology, key features, and limitations. The analysis underscores hydrothermal synthesis as a low-temperature, scalable, and cost-effective route with precise morphological control, while also outlining the specific strengths and drawbacks of competing methods. This framework reinforces the rationale for the methodology employed in this study and situates it within the broader landscape of $ZnGa_2O_4$ synthesis strategies.

Table 2.2. Comparison of hydrothermal synthesis with alternative methods for $ZnGa_2O_4$ nanostructures, highlighting reaction conditions, morphological outcomes, key features, and limitations.

Method	Temperature (°C)	Morphology	Key Features	Limitations	Ref.
Hydrothermal	100–180 °C	Nanoparticles, rodlike particles	Low-temperature, scalable, morphology control	Difficult to synthesize inverted spinel form	[61]

Sol-gel	500 °C, annealing at 500-600 °C	thin film	Simple, economical process, a formation of homogeneous oxides	Limited control over stoichiometry, batch-to-batch variation	[65]
CVD	1000 °C	Nanorods, high-purity single-crystalline	Widely used, scalable, high deposition rate	High equipment cost, complex process, two step method	[66]
ALD	200°C, annealing at 1000 °C	Nanowires	Atomic-level thickness control, excellent conformality	Slow deposition rate, requires precise control, two-step process	[67]
MOCVD	-	Thin films	High-quality films, precise doping control	Expensive precursors, complex process	[68]

2.3.3. Photocatalytic Activity of $ZnGa_2O_4$

A semiconductor is a material with electrical resistivity that lies between that of an insulator and a conductor. Its electronic band structure includes a valence band (VB), which is the highest occupied energy band, and a conduction band (CB), which is the lowest unoccupied band. These two bands are separated by an energy gap known as the band gap (Eg). [69] Photocatalytic activity in semiconductors is initiated when they absorb photons with energy equal to or greater than their band gap. This absorption excites electrons from the valence band to the conduction band, leaving behind positively charged holes in the valence band (see Figure 2.11). [70]

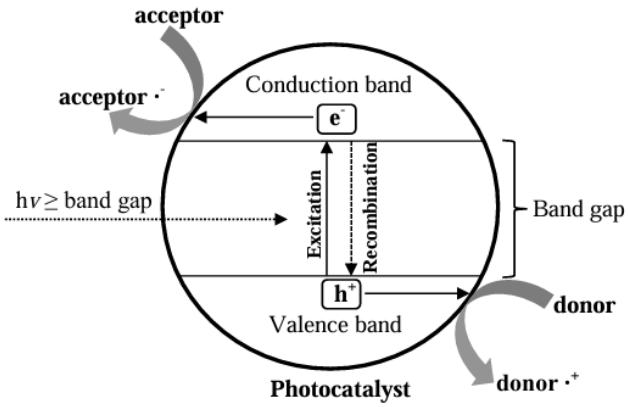

Figure 2.11. Diagram depicting the generation of photoinduced electron-hole pairs in a semiconductor photocatalyst upon photon activation. [70]

The basic process of photocatalysis begins with photon absorption, which can be described by the following equation:

$$\lambda(\text{nm}) = \frac{1240}{Eg\ (eV)} \tag{2.1}$$

where λ is the wavelength of light required to excite the semiconductor. Once excited, the generated electron-hole pairs (e^--h^+) can either recombine within the semiconductor, releasing energy as heat, or diffuse to the surface, where they participate in redox reactions. To achieve efficient photocatalysis, minimizing recombination and promoting interfacial electron processes is crucial.

In photocatalysis, photogenerated electrons in the conduction band reduce electron acceptors, such as adsorbed oxygen molecules, to form reactive oxygen species like superoxide radicals ($O_2^{\bullet-}$). Simultaneously, the holes in the valence band oxidize donor species, such as water or hydroxyl groups, generating highly reactive hydroxyl radicals ($OH^{\bullet}$) with an oxidation potential of +2.80 V. These radicals are key in the degradation of organic pollutants. [71]

For efficient photocatalytic reactions, the semiconductor's band positions must align with the redox potentials of the reactants. Specifically, the valence band must have a sufficiently positive potential to oxidize donor species, while the conduction band must be sufficiently negative to reduce electron acceptors. This alignment ensures the efficient generation of reactive species that drive oxidation and reduction reactions, such as organic matter degradation or water splitting into hydrogen (H_2) and oxygen (O_2).

Photocatalytic efficiency depends on several factors, including the material's ability to absorb photons effectively ($h\nu \geq E_g$), a high surface area with active sites for reactant adsorption, and stability against photocorrosion and electron-hole pair recombination. Additionally, the photocatalyst must be environmentally safe, cost-effective, and easy to produce to ensure practical applicability and long-term performance. [72]

The photogenerated holes oxidize organic pollutants directly or produce hydroxyl radicals that degrade the pollutants. Meanwhile, electrons in the conduction band reduce adsorbed oxygen to superoxide radicals, further enhancing oxidative degradation. If these processes do not occur simultaneously, electron-hole recombination can decrease photocatalytic efficiency. Therefore, designing an efficient photocatalyst requires optimizing its band structure, surface properties, and stability to enhance redox reactions while minimizing recombination, ensuring effective degradation of organic pollutants.

Several semiconductors, such as TiO_2, ZnO, GaP, and CdS, have been used in photocatalytic applications. [73] $ZnGa_2O_4$, particularly, exhibits strong redox reactions, and its absorption band gap aligns well with UV light sources, making it an excellent candidate for photocatalysis. In this study, β-Ga_2O_3 was selected as a reference photocatalyst due to its well-established UV-responsive photocatalytic activity and its

compositional similarity to $ZnGa_2O_4$. Both are oxide-based semiconductors containing Ga^{3+}–O coordination, making β-Ga_2O_3 an appropriate benchmark for evaluating the influence of defect states—particularly anti-site disorder—on the photocatalytic performance of $ZnGa_2O_4$. Various factors, such as film thickness, grain size, and hydrothermal temperature, have been explored in literature for their effect on the photocatalytic activity of $ZnGa_2O_4$ materials. [74-76] However, defect engineering has emerged as a promising method for tuning the photocatalytic performance of nanocatalysts, drawing significant attention in recent studies.

In 2017, Tu et al. synthesized $ZnGa_2O_4$ nanoparticles using a microwave-hydrothermal method, both with and without Hexadecyltrimethylammonium bromide (CTAB). They found that $ZnGa_2O_4$ particles synthesized with CTAB, which induced numerous defects such as dislocations on the (222) plane (the inset in Figure 2.12d), exhibited superior photocatalytic activity compared to samples without CTAB and defects. [77]

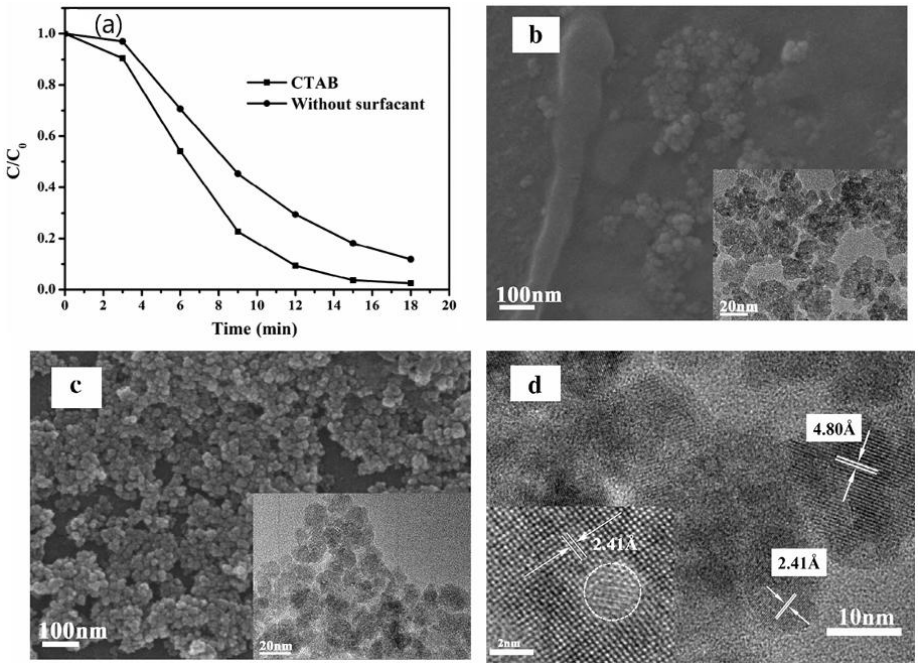

Figure 2.12. a) Photocatalytic performance of $ZnGa_2O_4$ nanoparticles in the degradation of methyl orange. SEM and TEM images (inset) of $ZnGa_2O_4$ particles synthesized at 120°C without CTAB (b) and with CTAB (c), along with HRTEM images (d) of the sample shown in (c). [77]

Oxygen vacancies are common defects in oxide materials and play a crucial role in photocatalytic activity. Experimental studies have shown that oxygen vacancies in $ZnFe_2O_4$ and $ZnGa_2O_4$ nanostructures can facilitate the recombination of photogenerated electron-hole pairs, thereby decreasing photocatalytic efficiency. [78, 79] However, oxygen vacancies in oxides such as TiO_2 and ZnO are known to enhance photocatalytic performance by improving the separation efficiency of photogenerated charge carriers, thus increasing photocatalytic efficiency. [80, 81] A study on $ZnGa_2O_4$ nanowires synthesized via a direct vapor transport process demonstrated that oxygen vacancies improved light absorption, enhanced electron-hole pair separation, and generated more hydroxyl radicals on the surface, thereby improving photocatalytic activity for methyl blue (MB) degradation under UV light, as shown in Figure 2.13. [75] Therefore, oxygen vacancies can

have both beneficial and detrimental effects on photocatalytic activity, depending on the specific material and context.

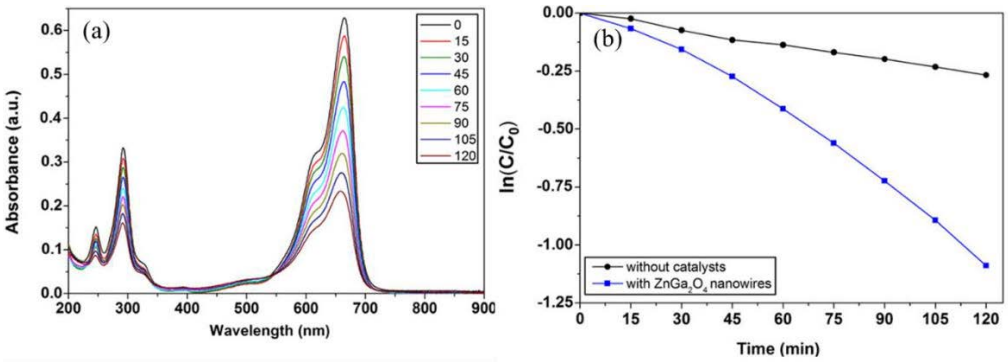

Figure 2.13. (b) Absorption spectrum of the MB solution with $ZnGa_2O_4$ nanowires under UV light exposure for varying durations. (c) Photocatalytic performance of $ZnGa_2O_4$ nanowires under UV light irradiation. [75]

Additionally, anti-site defects, where atoms in the lattice swap positions (e.g., Ga^{3+} substituting Zn^{2+} to form Ga_{Zn}), also significantly affect photocatalytic activity. Research has shown that Ga-doped ZnO (Ga_{Zn}) exhibits enhanced photocatalytic performance compared to pure ZnO. This enhancement is attributed to the improved separation of photoinduced charge carriers, which generates more hydroxyl radicals, increasing photocatalytic efficiency for organic pollutant degradation. [82, 83] In this work, the photocatalytic performance of $ZnGa_2O_4$ nanostructures—particularly the effect of anti-site defects—was evaluated by monitoring the UV-driven degradation of Rhodamine B (RhB), a widely used organic dye and model pollutant. The decrease in RhB concentration over time serves as an indicator of photocatalytic efficiency, reflecting the material's ability to generate reactive oxygen species and promote oxidative decomposition. Similarly, Zn-doped Ga_2O_3 nanocrystals have shown better photodegradation efficiency compared to undoped Ga_2O_3. The increased Zn^{2+} concentration in the material extends

the lifetime of trapped carriers and improves the separation of photogenerated carriers, leading to enhanced photocatalytic activity for degrading organic pollutants, as shown in Figure 2.14. [84, 85] Thus, the formation of defects, including oxygen vacancies and anti-site defects, plays a crucial and complex role in the photocatalytic activity of $ZnGa_2O_4$ and similar materials. While these defects can enhance the material's photocatalytic performance by improving charge separation and generating reactive species, their effects are context dependent and still a subject of ongoing research.

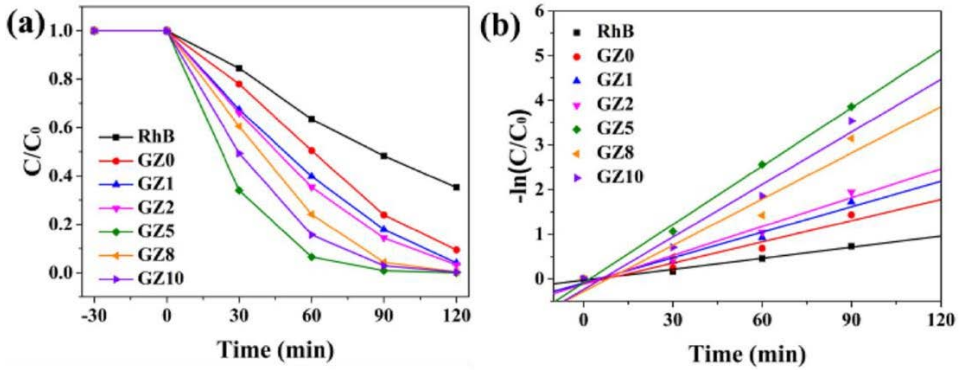

Figure 2.14. Photodegradation curves (a) and degradation rates (b) of pristine RhB solution and RhB solutions with GZ0, GZ1, GZ2, GZ5, GZ8, and GZ10 catalysts under Xe lamp irradiation. [84]

2.4. $(Al_xGa_{1-x})_2O_3$ Alloys

The $(Al_xGa_{1-x})_2O_3$ alloy systems offer a combination of advantageous properties, including a wide and tuneable bandgap, high dielectric constants, high breakdown electric fields and the potential for forming a high-density two-dimensional electron gas (2DEG). These attributes make the $(Al_xGa_{1-x})_2O_3$ alloys highly desirable for ultraviolet optoelectronics, deep-ultraviolet photodetectors, and high-power applications. Multiple polymorths, including α, β, γ, and κ, have been observed, with the monoclinic phase (similar to Ga_2O_3) and the corundum phase (similar to Al_2O_3) being the most

thermodynamically stable crystal structures for lower and higher Al concentrations, respectively (Figure 2.15). [86-88]

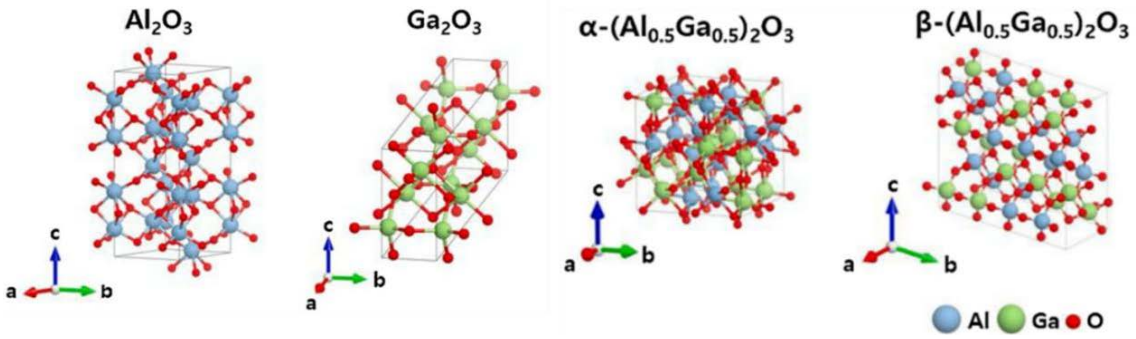

Figure 2.15. Atomic structures for Al_2O_3 in the corundum phase, Ga_2O_3 in the monoclinic phase, and $(Al_{0.5}Ga_{0.5})_2O_3$ in both monoclinic (β) and corundum (α) forms. The Al, Ga, and O atoms are represented in light blue, light green, and red, respectively. [88]

The $(Al_xGa_{1-x})_2O_3$ alloy system generally favours the monoclinic structure over the corundum structure based on enthalpy of mixing as a function of molar concentration. [16, 89, 90] The alloy system generally favours the monoclinic structure up to about 71% Al concentration, due to a lower enthalpy of mixing, as demonstrated by hybrid density functional theory calculations (Figure 2.16a). Beyond this concentration, the alloy increasingly adopts the corundum structure, which becomes more energetically favourable, especially at higher temperatures where Gibbs free energy favours the phase transition. This structural preference is attributed to the coordination environments preferred by Al atoms, which strongly favour occupying octahedral sites at Al concentrations below 0.5 as shown in Figure 2.16b. As the Al concentration exceeds 0.5, Al atoms begin to fill tetrahedral sites, leading to structural changes and an increase in the enthalpy of mixing. [14, 91] For x values near 0.71, the energy difference between the corundum and monoclinic structures is small, and high temperatures can easily overcome this difference. This explains why some experiments observe the monoclinic structure for

Al concentrations above 71% and the corundum structure for concentrations below 71%. [13, 16, 92-95]

The bandgap of $(Al_xGa_{1-x})_2O_3$ alloys also exhibits substantial tunability, spanning approximately 4.5 eV in Ga-rich compositions to about 8.8 eV in Al-rich compositions. This enables control over the material's absorption edge, making it adaptable for a wide range of deep-UV and power electronic applications. While this trend is generally linear with increasing Al content, a notable non-linear "bowing" effect occurs due to the structural mismatch between Ga_2O_3 and Al_2O_3, especially around 50% Al content. This tunability, encompassing both linear and non-linear shifts, makes $(Al_xGa_{1-x})_2O_3$ alloys adaptable for applications requiring adjustable optical properties. [88]

While all $(Al_xGa_{1-x})_2O_3$ compositions are classified as wide-bandgap semiconductors, their electrical conductivity varies with Al content. Al_2O_3-rich alloys are generally highly insulating due to their wide bandgap and low intrinsic carrier concentration, whereas Ga-rich compositions can exhibit measurable semiconducting behavior under appropriate doping or controlled defect conditions. Although $(Al_xGa_{1-x})_2O_3$ alloys have not been widely explored as conventional photocatalysts, their wide and tunable bandgaps enable deep-UV light absorption, suggesting potential for UV-driven photocatalytic applications. However, their actual photocatalytic performance depends on additional factors such as doping, nanostructuring, and defect engineering, and further research is needed to establish their practical viability.

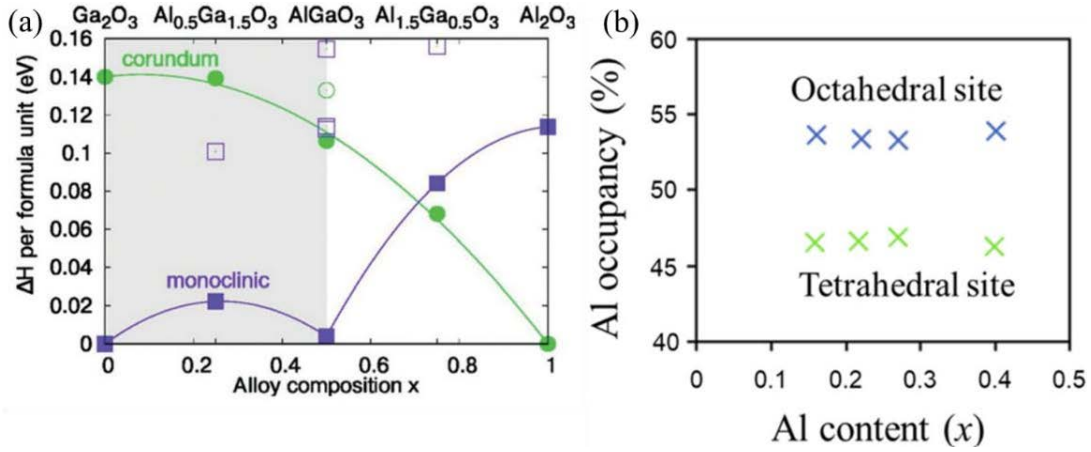

Figure 2.16. (a) Formation enthalpy as a function of alloy composition for both corundum and monoclinic structures. The shaded region indicates the composition range where Al prefers to occupy the octahedral sites in the monoclinic phase. [14] (b) Percentage of Al occupancy on tetrahedral and octahedral sites as a function of Al content (x) in β-$(Al_xGa_{1-x})_2O_3$ alloys. [91]

2.4.1. Bandgap Engineering of Ga_2O_3

Band gap engineering is a fundamental strategy in semiconductor materials science, enabling the precise design and optimization of materials to enhance their functional potential for specific applications. The band gap plays a foundational role in device physics and technology, and the ability to tune it provides flexibility for developing advanced semiconductor devices. With a native band gap of approximately 4.8 eV, Ga_2O_3 is highly suitable for applications such as solar-blind UV photodetectors, power devices, and photocatalysis for solar water splitting. Over recent decades, its band gap has been efficiently engineered through compositional tuning and alloying with materials possessing similar crystal structures or properties.

The band gap of β-Ga_2O_3 can be tailored significantly by alloying it with materials such as In_2O_3, ZnO, GaN, or I_2O compounds (where I = Li, Cu, or Ag). [96] For instance, alloying Ga_2O_3 with In_2O_3 has demonstrated a systematic reduction in the band gap from

4.8 eV to as low as 2.9 eV. [7] Among alloy systems, the Ga_2O_3–Al_2O_3 solid solution has garnered particular attention due to the high solubility of Al_2O_3 in Ga_2O_3 and its broad band gap tunability. This solid solution exploits the structural and compositional flexibility between the monoclinic β-phase of Ga_2O_3 and the trigonal α-phase corundum structure of Al_2O_3. [14] The equilibrium phase diagram predicts an aluminium solubility of approximately 67% at 1625 °C, a value closely aligning with the 71% solubility determined using hybrid density functional theory. [14] These findings suggest that $(Al_xGa_{1-x})_2O_3$ ternary alloys with high aluminium content are both feasible and stable under appropriate conditions.

The structural evolution of $(Al_xGa_{1-x})_2O_3$ alloys plays a pivotal role in their properties. Calculations indicate that the monoclinic phase of $(Al_xGa_{1-x})_2O_3$ remains energetically favourable and stable for aluminium incorporation levels up to 71%. Beyond this composition, the alloy transitions to the corundum phase, which becomes the thermodynamically stable structure. [97] This structural transformation significantly influences the crystalline and energy band properties of the material. Increasing the aluminium composition (x) in $(Al_xGa_{1-x})_2O_3$ profoundly modifies both its crystalline structure and band gap, enabling precise control over its electronic and optical behaviour. [98] Al_2O_3, with its exceptionally large band gap of 6.4 eV for amorphous films and 8.8 eV for bulk material, further enhances the band gap tuning potential of $(Al_xGa_{1-x})_2O_3$. The similar electron configurations of Al and Ga atoms facilitate the preparation of aluminium gallium oxide (AGO) materials, which exhibit band gaps ranging from 5 to 7 eV, making them suitable for a wider range of applications. [99]

Various deposition techniques, such as pulsed laser deposition (PLD), [13, 100] chemical vapor deposition (CVD), [92] sputtering, [101, 102] and molecular beam epitaxy (MBE), [103] have been employed to synthesize AGO films. β-$Al_{2x}G_{2-2x}O_3$ thin films have

been successfully grown on (100)-oriented Ga_2O_3 single-crystal substrates using plasma-assisted MBE. The substrates were thermally annealed at 1100 °C to enhance surface quality, and the films, deposited at a growth temperature of 800 °C, maintained the β-phase structure up to an aluminum content of x = 0.61. [16]

Similarly, bandgap-tuneable $(AlGa)_2O_3$ films were deposited on (0001) sapphire substrates using pulsed laser deposition (PLD) with a KrF excimer laser source. The PLD chamber was evacuated to a base pressure below 9×10^{-6} Pa, with an oxygen pressure of 0.1 Pa and a substrate temperature of 400°C during growth. Targets with varying Al content (mole ratios of Al/(Ga + Al): 0.22 to 1.0) were used to deposit films. Films grown with varying aluminium contents demonstrated band gap values of 5.2, 5.6, 6.1, 6.3, and 6.8 eV for Al mole fractions of 0.24, 0.54, 0.76, 0.89, and 0.98, respectively. (Figure 2.17). [13]

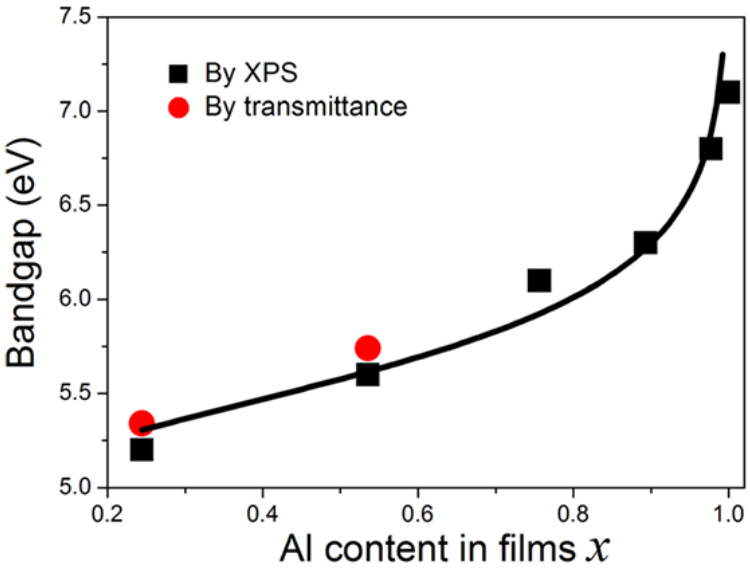

Figure 2.17. The bandgap as a function of Al content (x) in the PLD-grown (201) β- $(Al_xGa_{1-x})_2O_3$ layers. [13]

β-$(Al_xGa_{1-x})_2O_3$ thin films were successfully grown on (201) β-Ga_2O_3 substrates via metal-organic chemical vapor deposition (MOCVD) to explore the solubility of Al in the β-phase structure, achieving Al compositions as high as 48%. The growth process involved varying chamber pressures (80 and 20 Torr) and temperatures (880°C and 920°C), while maintaining a consistent [TMAl] / [TMAl+TEGa] molar flow rate ratio of 3.82%. The films exhibited Al compositions of 21%, 28%, 35%, 41%, and 48%, corresponding to energy bandgap values of 5.20, 5.35, 5.44, 5.54, and 5.72 eV, respectively. [4] The bandgap energies were found to be slightly influenced by the Al content, as illustrated in Figure 2.18. Due to current material growth limitations, β-$(Al_xGa_{1-x})_2O_3$ offers a relatively narrow tuneable bandgap range from 4.9 to 5.7 eV. These results demonstrate the potential of β-$(Al_xGa_{1-x})_2O_3$ for optoelectronic applications, with its bandgap tunability enabling targeted design for specific device needs (Figure 2.18). [104] To summarize, a comparison of key synthesis parameters and corresponding bandgap values for β-$(Al_xGa_{1-x})_2O_3$ thin films reported in literature is provided in Table 2.3.

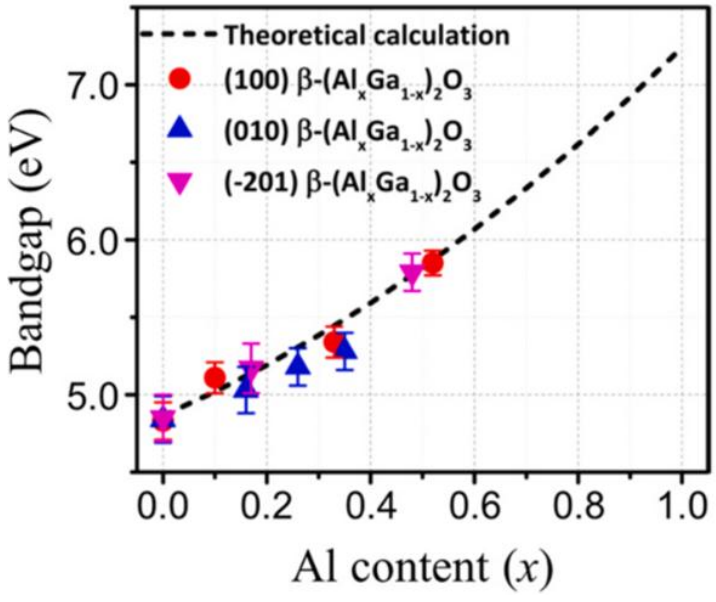

Figure 2.18. Bandgap of β-$(Al_xGa_{1-x})_2O_3$ as a function of Al content. [104]

Table 2.3. Summary of synthesis methods, conditions, and resulting bandgap values for β-$(Al_xGa_{1-x})_2O_3$, providing context for the chosen experimental approach.

Method	Substrate	Growth temp	Al content (x)	Bandgap (eV)	Pressure	Ref.
PLD	Sapphire (0001)	400°C	0.24-0.98	5.2-6.5	O_2 (0.1 Pa), high vacuum	[13]
MOCVD	β-Ga_2O_3(201)	880-920°C	0.21-0.48	5.2-5.72	20-80 Torr	[4]
MBE	β-Ga_2O_3(100)	800°C	Up to 0.61	No reported	Plasma-assisted, vacuum	[16]

2.4.2. Optical Properties of $(Al_xGa_{1-x})_2O_3$

Aluminium gallium oxide $(Al_xGa_{1-x})_2O_3$ is an emerging material with significant potential for optoelectronic applications due to its tuneable bandgap and distinctive luminescence characteristics. By incorporating aluminium into Ga_2O_3, the material's electronic and optical properties can be tailored. Understanding the influence of native defects on its optical properties and band structure is crucial for optimizing performance in devices such as ultraviolet (UV) photodetectors, power electronics, and optical coatings.

Photoluminescence studies provide valuable insights into the defect states within $(Al_xGa_{1-x})_2O_3$ primarily by analysing electron recombination mechanisms. When excited with a 266 nm laser, $(Al_xGa_{1-x})_2O_3$ samples exhibit emission bands across the UV, blue (BL), and green spectral regions, with weak red luminescence observed in some cases, as shown in Figure 2.19. The intensity of luminescence correlates strongly with defect

density, with higher defect concentrations enhancing the UV and green emission bands. [98]

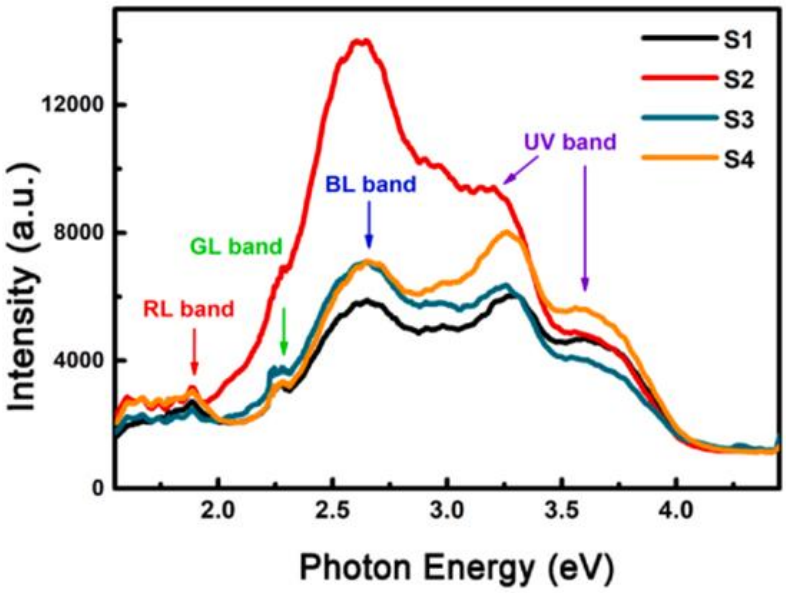

Figure 2.19. PL spectra of various $(Al_xGa_{1-x})_2O_3$ samples with an excitation wavelength of 266 nm. [98]

Gaussian peak fitting analysis of PL spectra identifies five dominant emission peaks occurring at approximately 3.64–3.67 eV, 3.22–3.26 eV, 2.97–3.00 eV, 2.62–2.65 eV, and 2.23–2.25 eV. The high-energy UV emissions (3.2–3.7 eV) originate from recombination events between free electrons and self-trapped holes. [28, 36, 105] The blue luminescence (2.7–3.0 eV) is attributed to donor-acceptor recombination, where donors typically include oxygen vacancies (V_O) and interstitial gallium (Ga_i), while acceptors consist of gallium vacancies (V_{Ga}) and gallium-oxygen vacancy complexes (V_O-V_{Ga}). [29, 30] Green emissions near 2.25 eV remain less well understood but are likely linked to neutral oxygen interstitials or clusters of oxygen vacancies, [28, 106] which have been observed in other materials like ZnO.

As the aluminium concentration in $(Al_xGa_{1-x})_2O_3$ increases to approximately 70%, its electronic band structure shifts closer to that of Al_2O_3. The separation between the Fermi level and the valence band top varies with aluminium content and the Fermi level moves toward the conduction band as Al content decreases. These shifts are indicative of changes in charge carrier dynamics and defect state distributions which are essential for tailoring the material's properties for specific optoelectronic applications. [98]

Native point defects significantly influence the optical and electronic behaviour of $(Al_xGa_{1-x})_2O_3$, particularly in modifying its conduction characteristics and introducing new emission pathways in the PL spectrum. Oxygen vacancies, gallium interstitials, and vacancy complexes contribute to optical transitions and can be leveraged for bandgap engineering through controlled defect manipulation. These defects also affect nonlinear optical properties, similar to those observed in other wide-bandgap materials such as $LiNbO_3$, ZnO, Al_2O_3, and TiO_2. [107-110] While β-Ga_2O_3 has been extensively studied, systematic investigations into Al-doped β-Ga_2O_3 remain limited. Further experimental and theoretical studies are necessary to elucidate defect formation mechanisms and their impact on optoelectronic properties. Future research should focus on defect control strategies, such as doping optimization, or surface passivation, to optimize $(Al_xGa_{1-x})_2O_3$ for advanced photonic and electronic applications.

To complement these optical studies, a summary of synthesis conditions and corresponding bandgap values reported for β-$(Al_xGa_{1-x})_2O_3$ thin films is presented in Table 2.3. Conventional methods such as MOCVD, PLD, and MBE require complex infrastructure, vacuum systems, and elevated processing temperatures. In contrast, the liquid-metal-based approach adopted in this thesis provides a low-temperature, scalable, and composition-tunable alternative for synthesizing ultrathin β-$(Al_xGa_{1-x})_2O_3$

nanosheets. These features make it a compelling platform for investigating the influence of aluminum content and defect states in wide-bandgap semiconductors.

2.4.3. Liquid-Metal Exfoliation of β-$(Al_xGa_{1-x})_2O_3$ Nanosheets

2.4.3.1. Introduction to Post-Transition Metals

Post-transition metals occupy a unique position in the periodic table, situated between transition metals and metalloids. This group includes elements such as gallium (Ga), aluminium (Al), indium (In), tin (Sn), lead (Pb), and Bismuth (Bi), all of which exhibit distinctive physical and chemical properties. [111, 112] These metals are characterized by relatively low melting points, weak metallic bonding, and a propensity for covalent or ionic behaviour due to their electron configurations.

The distinct electronic properties of post-transition metals, including increased ionization energies and reduced atomic radii due to higher nuclear charges, reduce the availability of electrons for metallic bonding and make these elements prone to covalency. As a result, these properties contribute to their semiconducting behaviour and other remarkable features. [50, 113] Post-transition metals are typically characterized by low mechanical strength, limited malleability and ductility, as well as relatively low melting points.

Among these metals, gallium stands out due to its unique properties. It has a melting point of 29.7 °C, allowing it to transition into a liquid state near room temperature, while its high boiling point (~2403 °C) ensures stability over a broad temperature range. These characteristics make gallium an ideal material for flexible, stretchable, and self-healing devices. [114, 115] However, since its melting point is slightly higher than room temperature, alloying gallium with other elements—most commonly post-transition metals—has led to the development of eutectic alloys with even lower

melting points. For example, adding 14 wt% indium to gallium produces the eutectic alloy Ga-In (EGaIn), which melts at just 15 °C, as shown in Figure 2.20, and This concentration is known as the eutectic point of the Ga–In system. [116] Similarly, the addition of tin forms the eutectic alloy EGaInSn (Galinstan), which remains liquid down to -19 °C. These alloys are highly soluble within each other, forming a monophasic system. Members of the post-transition metal family form many eutectic alloys with melting points below 330°C, including many that melt below 100 °C. [117] These alloys are not only accessible and thermally stable but are also safer to handle compared to alkali metals and less toxic than mercury, making them valuable for material synthesis, catalysis, and flexible optoelectronic applications. [117-121]

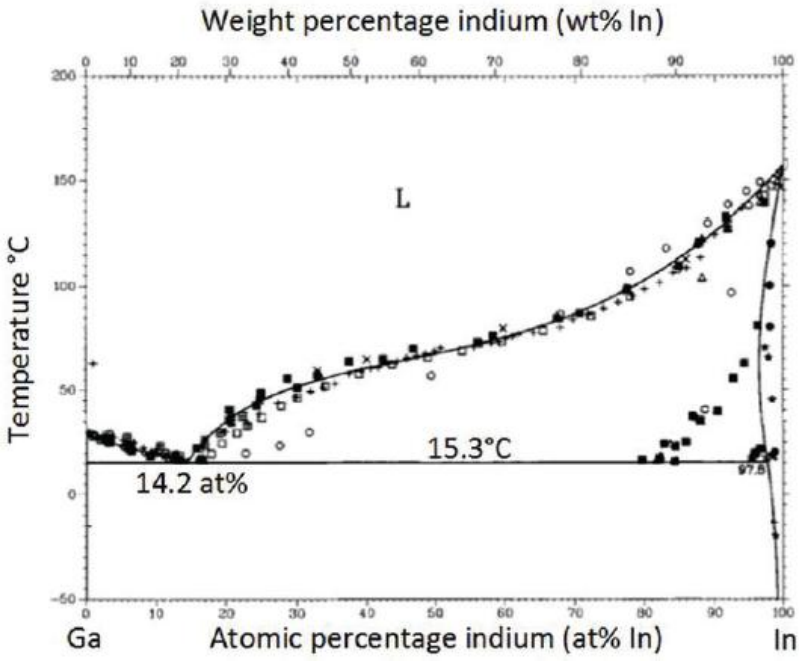

Figure 2.20. Phase diagram of the Ga–In binary system, with various experimentally determined data points. [116]

A unique feature of post-transition metals is their capacity to promote interface atomic layering on the surfaces of liquid metals. [122] The surfaces of liquid metals, such as gallium, are known to be atomically smooth due to their low viscosity and high surface tension. Upon exposure to ambient conditions, a thin, self-limiting oxide layer form spontaneously, creating a stable and uniform platform for nanosheet synthesis. [123] This surface layering minimizes positional fluctuations of near-surface ion cores, resulting in atomically smooth surfaces. These properties make liquid metals excellent templates for the synthesis of 2D materials. [124, 125]

Upon exposure to oxygen, an ultrathin, uniform, and atomically flat oxide layer forms on liquid metal surfaces. This surface oxidation significantly affects their physical properties and offers convenient pathways for the easy synthesis of 2D materials. [126-128] According to thermodynamic principles, the oxide layer composition is determined by the metal oxide with the lowest Gibbs free energy (ΔG_f), allowing for controlled synthesis of metal oxide layers on liquid metals. [18] For instance, the surfaces of pure gallium (Ga) or eutectic gallium-based alloys oxidize rapidly, forming an amorphous oxide layer typically 0.5–3 nm thick. This oxide layer reduces the liquid metal's surface tension, prevents further oxidation, and enhances its stability. A well-known example is the Ga_2O_3 coating on the surface of the galinstan (EGaInSn) alloy, where Ga_2O_3 dominates due to its lower Gibbs free energy compared to In_2O_3 and SnO_2 in an oxygen atmosphere. [129-131] These ultrathin oxide layers maintain their atomic flatness, enabling the production of uniform 2D materials. The synthesized 2D surface layers can be readily exfoliated and transferred to different substrates using mechanical or chemical methods, as shown in Figure 2.21. The weak interaction between the 2D layer and the liquid core, combined with van der Waals forces between the 2D material and polar substrates, facilitates low-temperature exfoliation for creating thin films on various surfaces. [18, 132]

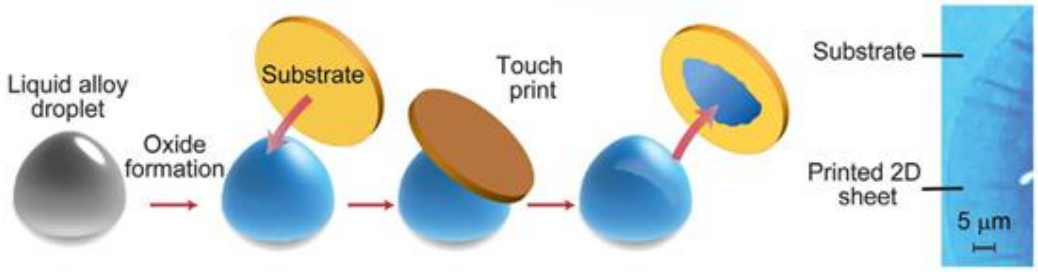

Figure 2.21. Schematic of van der Waals exfoliation: An oxide layer forms on a liquid metal droplet upon exposure to oxygen. Contact with a substrate enables transfer of this interfacial layer. Optical image shown on right. [18]

Unlike bulk materials, 2D materials—comprising single or few atomic layers—exhibit unique electronic, optical, and mechanical properties, making them highly valuable for electronic and optical devices as dielectric layers, conductors, semiconductors, or piezo-responsive materials. They also play a crucial role in catalysis, energy storage, and the fabrication of flexible optoelectronic devices. [128] The ability of post-transition metals, particularly Ga-based liquid metals, to form eutectic alloys with low melting points and remain stable under ambient conditions further enhances their potential for material innovation. The liquid state of these metals provides an ideal platform for the scalable synthesis of atomically thin layers and ultrathin metal oxides, enabling the efficient production of high-quality 2D materials.

2.4.3.2. Properties of Gallium-Based Liquid Metals

Gallium-based liquid metals exhibit remarkable electrical, thermal, mechanical, and fluidic properties. Their low melting points, unique surface behaviours, and oxidation characteristics make them highly versatile for applications in functional electronics, flexible devices, and 2D material synthesis. The following sections explore the

fundamental origins of their low melting points, the distinct surface phenomena that enable novel applications, and the role of surface oxidation in 2D material synthesis.

The melting points of metals are influenced by multiple factors, including valence electron delocalization, ionization extent, and crystal structure in the solid state. [117] Metals with pseudo-noble gas configurations, such as the group 12 elements (Zn, Cd, Hg), exhibit low melting and boiling points. This is due to their fully filled d and s shells, which reduce their tendency to form strong interatomic bonds, leading to weak metallic interactions. [111, 133] In contrast, post-transition metals—characterized by fully occupied d shells and partially filled p shells—generally display low melting points but relatively high boiling points, resulting in an extended liquid-state temperature range. The presence of unpaired p-electrons enables the formation of metallic or covalent bonds, particularly in lighter post-transition metals, contributing to their higher boiling points. [134, 135]

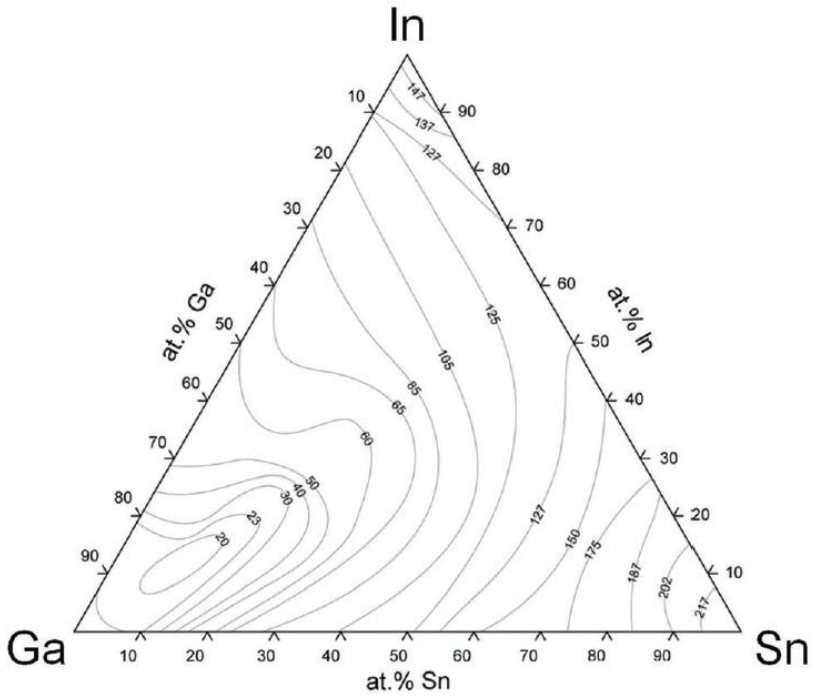

Figure 2.22. Liquidus phase diagram of the Ga–In–Sn system. [136]

Gallium, a post-transition metal with the lowest melting point in its group, exhibits both metallic and covalent bonding in its solid phase. The crystal structure and electron delocalization of gallium significantly impact its melting temperature. The formation of eutectic alloys further reduces melting points, as observed in the Ga-In system, which has a eutectic point at ~16 °C with 14.2% indium concentration (figure 2.20). [116] Adding tin (Sn) to create a ternary alloy lowers the melting point even further (figure 2.22). [136] Computational studies attribute this reduction to two key effects: increased atomic disorder from the addition of In and Sn, and localized charge density differences (figure 2.23), where In atoms possess tightly bound, low-energy valence electrons that act as atomic-scale lubricants, reducing interatomic interactions within the alloy. [137] The solubility of metals in liquid gallium, governed by Hume–Rothery rules, further influences melting behaviour, requiring similar atomic diameters, crystal structures, valencies, and electronegativities for high solubility. These unique low-melting properties of Ga-based systems not only underscore their complex bonding behaviour but also pave the way for innovative applications, including the development of liquid metals and thermally tuneable materials.

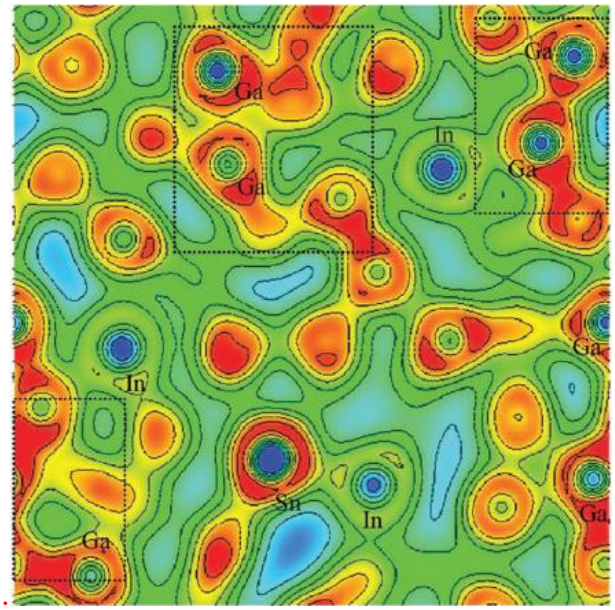

Figure 2.23. Electron density distribution map of Galinstan based on DFT calculations. Regions in red indicate high electron density, while blue areas represent low electron density. [137]

In addition to their tunable melting behavior, gallium-based liquid metals exhibit extraordinary surface phenomena that make them ideal candidates for advanced materials engineering and nanotechnology. Liquid metals exhibit remarkable surface phenomena, including atomic layering, surface segregation, and surface freezing, which have profound implications for materials science and nanotechnology. [138, 139] While the bulk of liquid metals lacks both long- and short-range atomic order due to their fluid nature, their surfaces often display a quasi-crystalline arrangement of atoms. This surface-induced atomic layering, first predicted theoretically in the early 1980s, arises from the unique electronic structure of liquid metals and the steep variation in electron density across the liquid-vapor or liquid-solid interface. [124, 125, 140] Surface layering has been experimentally observed in various metals, including gallium and mercury, and later in alloys such as Ga–In, Ga–Sn, and Ga–Bi. [126, 141-145] These surface layers, typically a few nanometres thick, provide liquid metals with atomically flat surfaces, making them excellent templates for synthesizing ultrathin 2D materials. Notably, de Vries et al. demonstrated

that the phenomenon persists even when liquid metals, such as gallium, are in contact with solid surfaces, including the (111) surface of diamond, not only when in contact with vapor. This property has been instrumental in advancing the use of liquid metals as templates for 2D material fabrication. [146]

In addition to atomic layering, liquid metal alloys exhibit surface segregation, a phenomenon where elements with lower surface energy concentrate at the surface, leading to distinct compositional gradients between the surface and the bulk. [139] This effect is particularly pronounced in alloys such as Ga–In and Ga–Sn, where the surface becomes enriched with indium or tin, despite their lower bulk concentrations. The interplay of surface segregation and atomic layering enables precise control over surface composition, offering novel pathways for tailoring surface chemistry in catalysis, electronics, and energy applications. [126, 143] Another notable phenomenon, surface freezing or surface crystallization, occurs in certain liquid metal alloys at temperatures slightly above their melting points. In this state, a solid crystalline layer forms on the liquid metal's surface, as observed in eutectic Au-Si alloys through grazing incidence X-ray diffraction measurements. [138]

Together, these surface phenomena—atomic layering, surface segregation, and surface freezing—highlight the exceptional properties of liquid metals and their alloys. These unique characteristics enable their use in advanced applications, including the templating of atomically precise materials, the synthesis of ultrathin structures, and the creation of compositional gradients or crystalline surface layers.

2.4.3.3. Surface Oxidation of Liquid Metals for 2D Material Synthesis

Surface oxidation of liquid metals provides a versatile and innovative approach for synthesizing 2D materials. [122] The unique properties of liquid metals—including their fluidity, minimal interfacial energy, and ability to form atomically smooth surfaces—

facilitate the clean exfoliation of ultrathin oxide films without compromising structural integrity. By controlling reaction conditions and alloy compositions, this method enables tuneable synthesis, opening new possibilities in materials science.

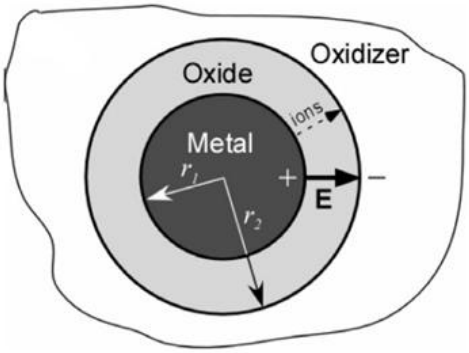

Figure 2.24. Spherical models illustrating the oxidation process of a metal particle in an oxidizing environment. [147]

Liquid metals are highly reactive and rapidly oxidize upon exposure to ambient oxygen, a property extensively utilized for fabricating 2D metal oxides. [122] The oxidation behaviour typically involves a rapid initial rate that diminishes over time, forming a stable oxide layer. This behaviour aligns with the Cabrera-Mott model, which describes how an electrostatic potential (Mott potential) forms between the oxide-metal and oxygen-oxide interfaces (Figure 2.24). [147, 148] This potential facilitates the diffusion of metal ions through the oxide layer, promoting growth until a self-limiting thickness is reached. The relationship between oxidation time and oxide thickness follows the equation $1/X = A\text{-}B \times \ln t$, where X is the oxide thickness, t is oxidation time, and A and B are constants. [147] While this process is often described as 'self-limiting,' it is more accurately characterized as kinetically limited by the Cabrera–Mott mechanism, in which oxide growth slows dramatically and effectively saturates under ambient conditions. Though some minimal continued growth may occur over long timescales, the rate becomes negligible for most

practical purposes. This self-limiting oxidation behaviour underpins the synthesis of ultrathin, uniform 2D metal oxides such as Ga_2O_3, PbO, and ZnO (Figure 2.25). [149-151]

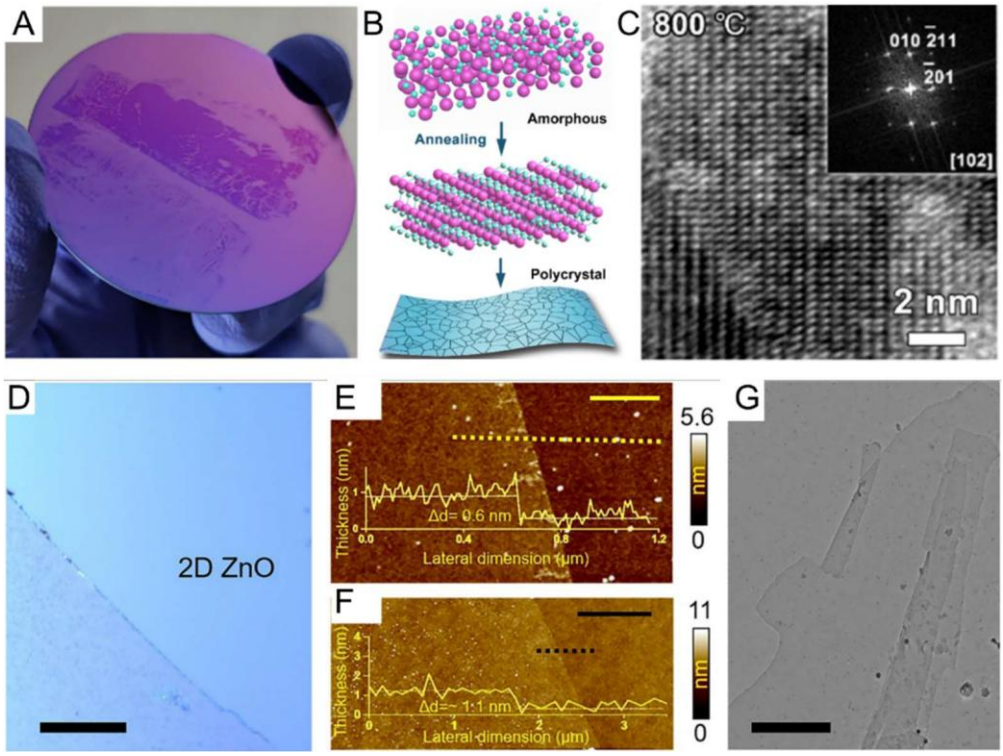

Figure 2.25. Controlled oxide surface layer growth on liquid metal for 2D metal oxide deposition (Ga_2O_3 and ZnO). (A) A large-area amorphous 2D Ga_2O_3 layer deposited on a 2-inch Si-SiO_2 substrate. (B) Atomic model schematic illustrating the structural transition of the amorphous 2D Ga_2O_3 layer into crystalline 2D β-Ga_2O_3 through thermal annealing. (C) High-resolution TEM image of the 2D crystalline Ga_2O_3, with an inset showing the corresponding SAED pattern. (D) Optical microscopy image of a uniform, millimeter-scale ZnO sheet deposited on a Si-SiO_2 wafer (scale bar: 100 μm). (E) AFM image of a 0.6-nm-thick ZnO sheet (scale bar: 500 nm). (F) AFM image of a 1.1-nm-thick ZnO sheet (scale bar: 4 μm). (G) TEM image of a ZnO sheet, highlighting its preferred growth direction in the wurtzite phase (scale bar: 1 nm). [150, 151]

While the Cabrera-Mott model applies to many liquid metals, others-such as Sn, In, and Bi-do not follow Cabrera-Mott kinetics and exhibit continuous oxidation, leading

to porous or unstable oxide layers that grow continuously and leading to thicker, non-uniform oxide layers. For instance, molten tin exposed to air undergoes progressive oxidation, forming a sequence of tin oxides (SnO, SnO_2, Sn_2O_3, Sn_3O_4). The oxidation process influences the resulting oxide layer's color, composition, and morphology (Figure 2.26 A-E). By adjusting oxygen concentrations to 10–100 ppm, it is possible to reproducibly deposit monolayer SnO films over large areas (Figure 2.26 F-I). [152-154]

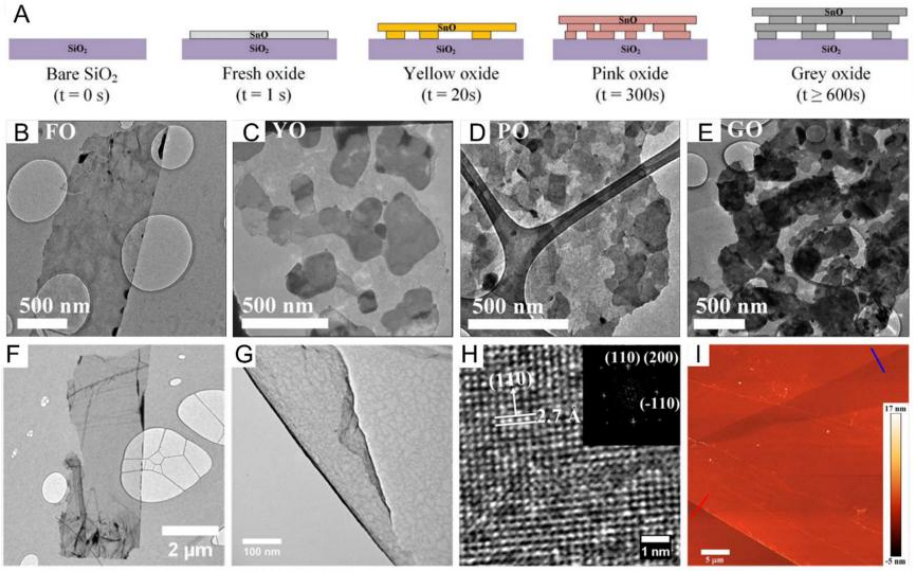

Figure 2.26. (A) Schematic representation of tin oxide layers with varying thickness, morphology, and color, formed by exposing molten tin to ambient air for different durations. (B-E) TEM images of fresh, yellow, pink, and grey tin oxides synthesized at different reaction times. (F) TEM image of a nanosheet produced in a continuously purged glovebox (N_2 atmosphere, with O_2 concentration typically between 10 and 100 ppm). (G) TEM image of a freestanding edge of a tin oxide nanosheet. (H) High-resolution TEM image of a sample synthesized under reduced oxygen conditions, with an inset displaying the Fast Fourier Transform (FFT) image indexed to SnO. (I) AFM image of tin oxide grown under reduced oxygen conditions, showing step heights of 1.1 nm (red line) and 0.4 nm (blue line). [152, 154]

Liquid metal alloys introduce additional versatility through selective oxidation, governed by thermodynamic principles. The surface oxide of an alloy is dominated by

the metal oxide with the lowest Gibbs free energy of oxidation. [18] For example, in gallium-based eutectic alloys like EGaIn and Galinstan, the surface is predominantly covered by Ga_2O_3 due to gallium's high reactivity. This allows for the deposition of high purity 2D Ga_2O_3. [155]

For alloys containing metals with comparable reactivity, oxidation can lead to mixed oxides or compositions influenced by surface energy effects. Notably, alloying gallium with high-melting-point metals like Al, Gd, or Hf enables the synthesis of ultrathin Al_2O_3, Gd_2O_3, and HfO_2**.** These oxides, with thicknesses ranging from 0.5 to 1.1 nm, extend 2D material synthesis to non-layered structures materials (Figure 2.27). [18]

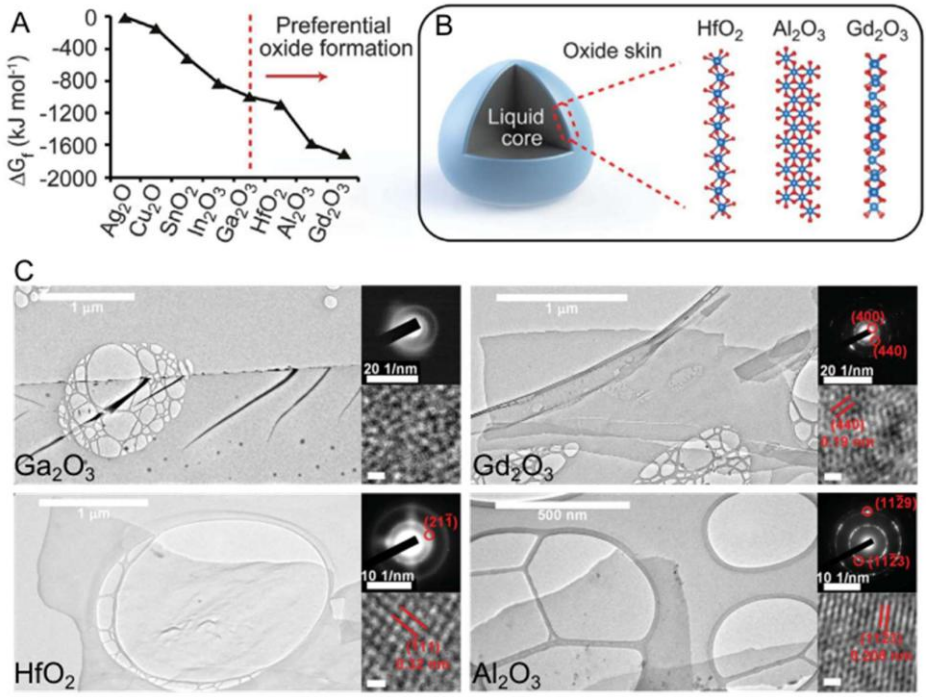

Figure 2.27. (A) Gibbs free energy of formation for selected metal oxides, with those to the right of the red dashed line likely to dominate the surface of gallium-based liquid metals. (B) Cross-sectional schematic of a liquid metal droplet, depicting the possible crystal structures of ultrathin HfO_2, Al_2O_3, and Gd_2O_3 layers. (C) TEM images, high-resolution TEM images, and corresponding SAED patterns of Ga_2O_3, HfO_2, Al_2O_3, and Gd_2O_3 nanosheets formed via liquid alloy oxidation. [18]

Beyond oxides, exposing liquid metals to other reactive gases, such as hydrogen sulfide (H_2S)**,** facilitates the synthesis of 2D metal sulfides, demonstrating the method's adaptability across diverse material classes. The oxide layer can be exfoliated and transferred onto substrates using techniques such as touch printing or squeeze printing. These methods rely on the weak van der Waals forces at the oxide-metal interface, allowing clean separation and preserving structural integrity. Touch printing involves briefly contacting the oxide surface with a substrate, enabling uniform transfer over large areas. Alternatively, Bubbling and sonication can be used to produce high-yield nanoflakes with smaller lateral dimensions. [18, 156] For ternary oxides like indium-tin oxides (ITOs), competitive oxidation of indium-tin alloys yields transparent, conductive films suitable for flexible substrates. The touch-printing method has also been adapted to produce such complex oxides, showcasing its versatility in synthesizing both binary and ternary 2D materials with exceptional control over thickness and uniformity.

The surface oxidation of liquid metals presents a scalable and innovative method for synthesizing high-quality 2D materials with exceptional uniformity and tuneable thickness, overcoming previous challenges in fabricating high-melting-point oxides. This approach enables precise thickness control through self-limiting growth, facilitates high-purity material deposition via selective oxidation, and supports large-area production using scalable exfoliation techniques. Furthermore, its compatibility with diverse chemistries beyond oxides expands its potential applications. These advantages position liquid metal oxidation as a foundational technique for next-generation materials in electronics, optoelectronics, catalysis, and energy storage, driving transformative advancements in nanoscale science and technology.

In summary, this chapter has outlined the fundamental properties and recent developments in β-Ga_2O_3, $ZnGa_2O_4$, and β-$(Al_xGa_{1-x})_2O_3$ alloys, including their crystal structures, optical behavior, and photocatalytic potential. The review highlights the significance of intrinsic and extrinsic defects, cation disorder, and compositional tuning in governing their performance across various applications. Additionally, the emergence of liquid-metal-based synthesis methods offers a low-temperature, scalable pathway for fabricating ultrathin oxide semiconductors with controlled properties. The insights from this chapter provide a critical foundation for understanding the motivation, methodology, and interpretation of the experimental studies presented in Chapters 3 and 4, which focus on the hydrothermal synthesis of $ZnGa_2O_4$ nanostructures and the liquid-metal-assisted exfoliation of Al-enriched β-$(Al_xGa_{1-x})_2O_3$ nanosheets.

Chapter 3. Experimental details

This chapter presents the experimental methodologies employed for the synthesis, transfer, and characterization of oxide-based nanostructures explored in this thesis. Two main fabrication techniques are detailed: a hydrothermal synthesis route used to grow stoichiometric $ZnGa_2O_4$ microplates, and a low-temperature, liquid-metal-based exfoliation method to produce two-dimensional (2D) β-$(Al_xGa_{1-x})_2O_3$ nanosheets. The chapter also outlines the key post-synthesis treatments and photocatalytic measurements conducted on $ZnGa_2O_4$, as well as the environmental conditions used to control oxide growth on liquid Ga–Al alloys. Following the synthesis sections, a comprehensive overview of the characterization techniques—including Raman spectroscopy, AFM, XRD, SEM, and cathodoluminescence (CL)—is provided to demonstrate how the structural, morphological, and optical properties of the materials were evaluated. Together, these experimental approaches form the foundation for the results and discussion presented in subsequent chapters.

3.1. Hydrothermal method

The hydrothermal synthesis method is a widely used wet chemical technique that offers several advantages, including affordability and high efficiency. By allowing precise control over synthesis parameters such as temperature, time, and pressure, this method produces single crystals. It is particularly effective for creating stoichiometric $ZnGa_2O_4$ microplates. The duration of the hydrothermal reaction significantly impacts the formation of nanocrystalline structures, with microplates of varying crystallite sizes being achieved at different reaction times.

3.1.1. Synthesis of $ZnGa_2O_4$ microplates

All the chemicals were used as received without further purification. Gallium nitrate ($Ga(NO_3)_3$, 99.9%), zinc acetate ($Zn(CH_3CO_2)_2$, 99.99%), and ethylenediamine ($C_2H_4(NH_2)_2$) were purchased from Sigma-Aldrich.

The synthesis procedure to produce $ZnGa_2O_4$ nanoplates in this work is illustrated in the schematic shown in Figure 3.1. In a typical synthesis, 2 mmol of $Ga(NO_3)_3$ and 1 mmol of $Zn(CH_3CO_2)_2$ were dissolved in 26 mL of deionized water to obtain a Zn:Ga molar ratio of 0.5. Subsequently, an aqueous solution of ethylenediamine $C_2H_4(NH_2)_2$ was added dropwise to the mixture while stirring magnetically, adjusting the pH to 12. This pH was selected based on previous studies that identified it as optimal for the formation of high-quality, single-phase $ZnGa_2O_4$. [157] The resulting solution was stirred continuously for 60 minutes to ensure homogeneity before being transferred to a Teflon-lined autoclave and heated at 180 °C for up to 48 hours. The product was collected by centrifugation, washed with methanol, and dried under vacuum at 60 °C for 12 hours. The $ZnGa_2O_4$ microplates were subjected to annealing to enhance their crystallinity. The annealing process was conducted in an argon (Ar) atmosphere at a temperature of 800 °C. The temperature was increased at a rate of 5 °C per minute, and the microplates were maintained at this temperature for a duration of 2 hours to achieve the desired improvement in crystallinity.

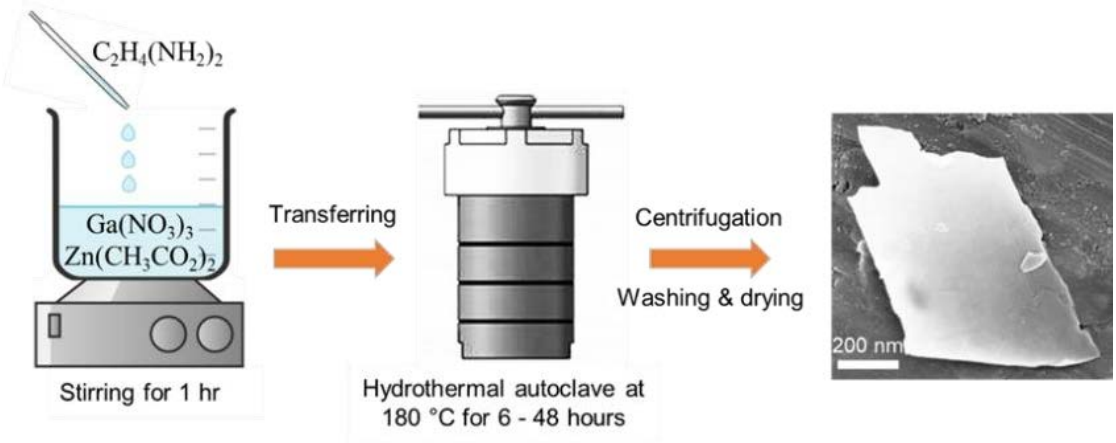

Figure 3.1. Schematic illustration of the hydrothermal synthesis procedure used to fabricate $ZnGa_2O_4$ microplates.

3.1.2. Photocatalytic activity of $ZnGa_2O_4$ microstructures

The photocatalytic activity of $ZnGa_2O_4$ nanoplates was evaluated through the photodegradation of Rhodamine B (RhB) under irradiation from an Eagtac ultraviolet A (UVA) 12 W torch, which emits light in the 350–385 nm range with a peak intensity at 365 nm. All photocatalytic measurements were conducted at room temperature. For comparison, Ga_2O_3 nanorods (radius ~ 0.5 μm, sourced from Sigma-Aldrich) were tested under identical conditions. In a typical experiment, 2 mg of $ZnGa_2O_4$ nanoplates were dispersed in 4 mL of a 5 μM RhB solution; this RhB concentration was chosen to provide absorbance below 1 for optimal light quantification using a Cary 60 UV-Vis spectrometer. The suspension was stirred in the dark for 30 mins to establish adsorption-desorption equilibrium. Following the irradiation, the $ZnGa_2O_4$ photocatalyst was separated by centrifugation in a 4 mL glass vial and the remaining RhB concentration was measured by monitoring its characteristic absorption peak at 554 nm in a polystyrene cuvette using the UV-Vis spectrometer. To maintain consistency, a fresh RhB solution was prepared for each irradiation interval. The degradation rate of RhB was expressed as $\ln(A/A_0)$, where

A is the absorbance at each time interval and A_0 is the initial absorbance at the adsorption–desorption equilibrium. The entire measurement process took 90 minutes to complete, with photocatalytic activity recorded every 15 minutes.

3.2. Exfoliation of Two-Dimensional β-$(Al_xGa_{1-x})_2O_3$ from Liquid Metals

3.2.1. Introduction

The liquid metal-based exfoliation method is a transformative approach for synthesizing two-dimensional (2D) nanosheets. This technique leverages the unique properties of liquid metals or their alloys, where selective oxidation occurs at the liquid metal surface, forming atomically thin oxide layers. Key parameters, such as the composition of the liquid metal alloy and the ratio of elements, are precisely controlled to achieve desired compositions and structures. This method is particularly advantageous for producing doped 2D materials, as the spontaneous migration of elements with lower Gibbs free energy of oxide formation (ΔG_f) allows for efficient and selective doping.

Unlike conventional methods, the liquid metal-based approach eliminates the need for high temperatures or complex, multi-step processes. It offers a one-step, low-temperature synthesis route that enables precise control at the atomic scale, facilitating the production of high-quality nanosheets with tuneable properties. This method not only simplifies the synthesis process but also enables access to a broader range of compositions, making it a pivotal technique in advancing the field of 2D material research.

3.2.2. Extraction and Transfer of β-$(Al_xGa_{1-x})_2O_3$ from Liquid Metals

All the chemicals were used as received without further purification. Gallium (round shots, 99.9%) was purchased from Roto metals, USA, and Aluminium (wire with

a diameter of 1.0 mm, 99.999%) was purchased from Thermo Fisher Scientific. Thermally oxidised Si substrates with a ~300 nm SiO_2 layer were employed for nanosheet exfoliation and transfer.

To investigate the correlation between Al concentration in the Ga–Al liquid alloy and the resulting nanosheet composition, Ga–Al alloys with Al concentrations ranging from 0.01 to 10 at% were prepared by mixing and melting high-purity Ga and Al metals at 250 °C in a nitrogen-filled glovebox. Once the alloy was homogenized, a small droplet was transferred onto a preheated Si/SiO_2 substrate. A second substrate, also preheated, was then used to gently compress the droplet, spreading the alloy into a thin film and promoting surface oxidation. This process, known as squeeze printing, enabled the transfer of $(Al_xGa_{1-x})_2O_3$ oxide layers from the liquid metal surface to the substrate, as illustrated in Figure 3.2. Layers of Ga_2O_3 were produced from pure liquid Ga. Sample preparation and nanosheet harvesting were conducted in a nitrogen glove box with an oxygen level maintained at 0.1 – 0.2% to regulate interfacial oxidation. This controlled environment facilitates the formation of an ultrathin, self-limited oxide layer on the liquid metal surface via the Cabrera–Mott mechanism.[156] The nonpolar nature of the liquid metal prevents strong adhesion to the surface oxide, allowing the weakly adhering oxide layer to be readily transferred onto a substrate via van der Waals attractive forces. [18]

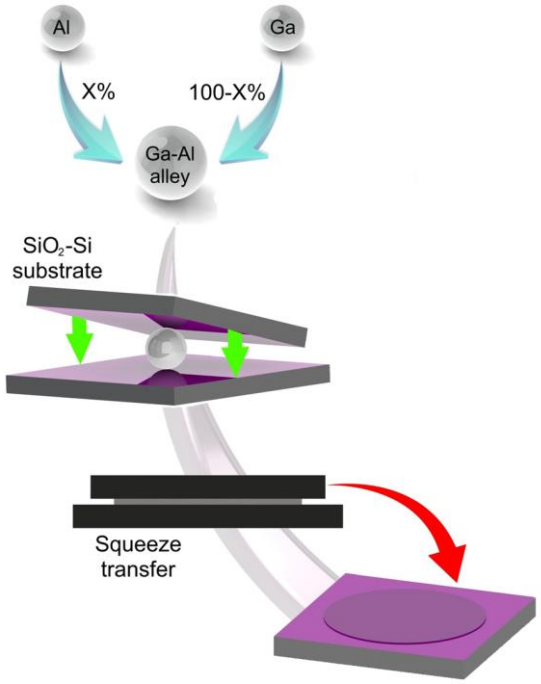

Figure 3.2. Schematic illustration of a liquid Ga-Al droplet and the van der Waals squeeze printing process for the fabrication of 2D β-$(Al_xGa_{1-x})_2O_3$ sheets on Si/SiO_2 substrates.

3.3. Characterisation Techniques

A range of characterization tools and techniques was employed in this research for the morphological, structural, and optical analysis of the samples. The details of these methods are described in the subsequent sections.

3.3.1. Raman Spectroscopy

Confocal Raman spectroscopy was conducted in a backscattering configuration using a Horiba LabRAM HR Evolution Raman spectrometer to analyse the crystal structure of synthesized $ZnGa_2O_4$ and 2D β-$(Al_xGa_{1-x})_2O_3$. The samples were excited with a 532 nm laser at room temperature, enabling detailed characterization of the vibrational modes and structural properties of the microplates.

3.3.2. Atomic force microscopy (AFM)

Atomic Force Microscopy (AFM) is a versatile and powerful technique for analysing the three-dimensional surface morphology of thin films and nanostructured materials. Unlike other microscopy techniques, AFM does not require the material to be conductive, making it suitable for semiconductors, insulators, and conductive samples. AFM operates by measuring the interaction forces between a sharp probing tip and the sample surface, allowing for high-resolution imaging of topographical and structural features. A schematic view of the AFM setup and tip image (SEM) is shown in Figure 3.3.

In AFM, a sharp tip at the end of a cantilever is raster-scanned across the sample surface. The tip height typically ranges from 3–6 μm, with a radius smaller than 10 nm for precise measurements. A laser beam is focused on the back of the cantilever, and the reflected light is captured by a quadrant photodiode. Variations in the deflection of the cantilever, caused by the interatomic forces between the tip and the sample, are monitored and translated into detailed topographical maps. AFM can operate in various modes, including contact and non-contact. In contact mode, the tip maintains physical contact with the surface, which may cause sample degradation. In contrast, non-contact mode uses oscillating tips to detect Van der Waals forces without touching the surface, minimizing potential damage.

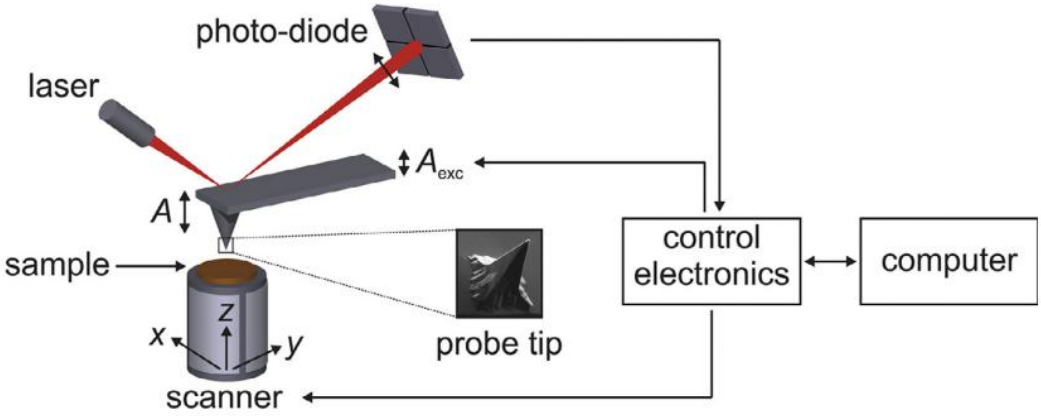

Figure 3.3. Schematic of a typical AFM setup. [158]

In this study, a Park XE7 AFM (figure 3.4) and a Nanoscope IIIa Dimension 3100 Scanning Probe Microscope (Digital Instruments) were used to investigate the morphology of $ZnGa_2O_4$ microplates and 2D β-$(Al_xGa_{1-x})_2O_3$. The non-contact mode was selected to ensure accurate imaging while preserving the integrity of the samples. The Olympus AC160TS cantilever, designed for non-contact applications, was utilized. This cantilever features a high resonant frequency and a backside reflective coating, ensuring high sensitivity and resolution.

The analysis provided detailed insights into the surface topography, including the root-mean-square roughness and structural features of the samples. Software tools such as XEI and NanoScope Analysis were employed to process the AFM images and extract quantitative data. This comprehensive approach enabled precise characterization of the $ZnGa_2O_4$ microplates and the thickness of 2D β-$(Al_xGa_{1-x})_2O_3$, highlighting the potential of AFM for studying nanoscale materials.

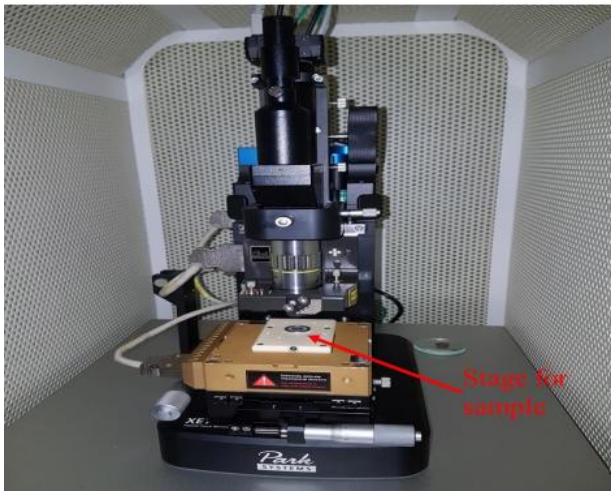

Figure 3.4. The Park XE7 AFM system was set up on a vibration-isolated optical table within the Microstructural Analysis Unit (MAU) at UTS.

3.3.3. X-ray diffraction (XRD)

To characterize the structures of $ZnGa_2O_4$ microplates and β-$(Al_xGa_{1-x})_2O_3$ materials, X-ray diffraction (XRD) analysis was performed. A Bruker D8 Discovery diffractometer with Cu Kα radiation (λ = 1.54 Å) and a scanning step size of 0.02° was used for $ZnGa_2O_4$ microplates. For the bulk and 2D β-$(Al_xGa_{1-x})_2O_3$ materials, phase compositions were analyzed using a multi-purpose XRD system and an Empyrean thin-film XRD instrument, both employing Cu Kα radiation (λ = 1.54 Å).

3.3.4. Scanning Electron Microscopy (SEM)

Scanning Electron Microscopy (SEM) is a powerful technique that utilizes a focused beam of high-energy electrons (typically 1–30 keV) to interact with the surface of solid materials, resulting in the emission of various signals. These include secondary electrons (SE), backscattered electrons (BSE), characteristic X-rays, and cathodoluminescence (CL). The interaction between the electron beam and the material generates signals that provide detailed insights into different properties of the sample. Secondary electrons, with low energy (1–3 eV), are emitted from the near-surface region

of the sample, offering high-resolution topographical information. In contrast, backscattered electrons, which are higher in energy, originate from deeper within the material and provide compositional and crystal structure details. Characteristic X-rays, emitted due to the ionization of inner-shell electrons, reveal the elemental composition and concentration within the sample. CL, another signal generated during electron beam interaction, provides information on electronic transitions and the electronic structure of the material. Figure 3.5 illustrates the interaction of an electron beam with a material and the various signals generated. In this study, a Field Emission Scanning Electron Microscope (FESEM) system, the Zeiss Supra 55VP, was employed for high-resolution surface imaging of the samples.

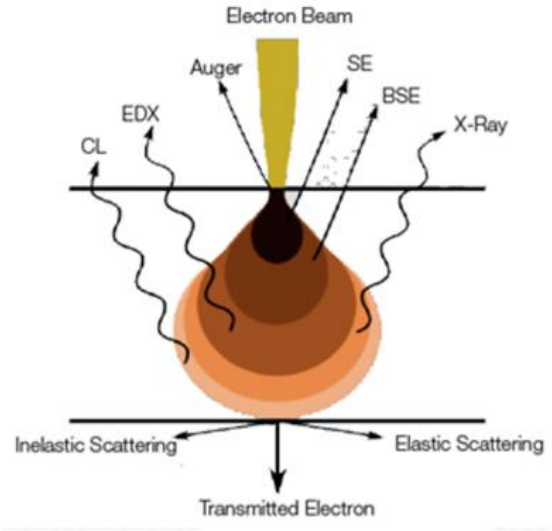

Figure 3.5. Schematic illustration of the incident electron beam, the resulting emitted electronic and photonic signals, and their interaction volumes within the material. [159]

3.3.5. Luminescence spectroscopy

Cathodoluminescence (CL) spectroscopy is a non-invasive method frequently used to explore the optical and electronic characteristics of materials. This technique involves bombarding a material with high-energy electrons, which promotes electrons

from the valence band to the conduction band, leaving holes in the valence band. As the electrons recombine with the holes, light is emitted, which is collected to form a CL spectrum. CL spectra provide crucial insights into material features like defects, dopants, impurities, and bandgap energies. The emission mechanisms can be categorized into intrinsic, where recombination occurs directly between conduction band electrons and valence band holes, and extrinsic, which involves localized states within the bandgap, such as donor and acceptor levels, deep-level defects, and bound excitons.

Figure 3.6 illustrates the various recombination processes responsible for cathodoluminescence (CL) emissions. The first channel shows the direct band-to-band transition, where an electron in the conduction band recombines with a hole in the valence band, producing light with energy equal to the bandgap. Channels 2, 3, and 4 encompass excitonic recombination— free (FX) and bound (BX)—as well as neutral donor to free hole recombination and the recombination of free electrons with neutral acceptors. Channel 5 focuses on donor-acceptor pair (DAP) transitions, while Channel 6 highlights internal transitions within emission centres, such as point defects, transition metals, or rare earth elements. Lastly, Channel 7 represents non-radiative recombination, where energy is released without the emission of light. These various emission processes enable CL to provide detailed information about a material's electronic and luminescent behaviour, especially for wide bandgap semiconductors, with high spatial resolution at the nanoscale.

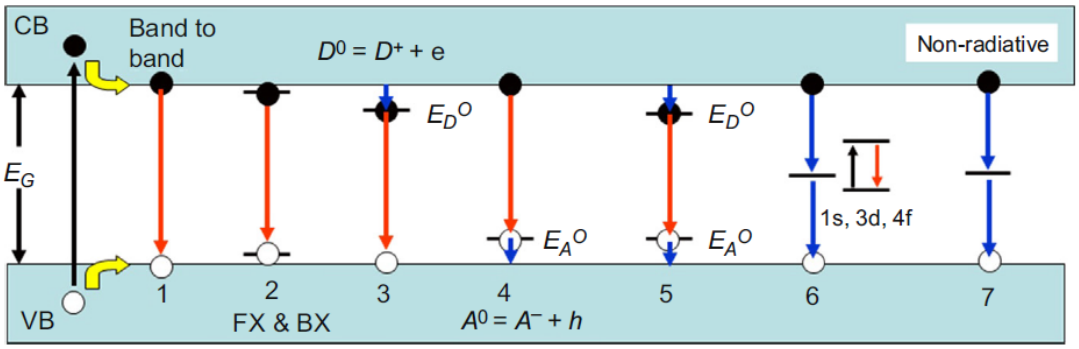

Figure 3. 6. Schematic of recombination channels among electrons, holes and defect states in a semiconductor. [160]

3.3.5.1. Experimental setup of cathodoluminescence

The cathodoluminescence (CL) setup used for measuring the optical and electrical properties of $ZnGa_2O_4$ microstructures and 2D β-$(Al_xGa_{1-x})_2O_3$ consists of a FEI Quanta 200 scanning electron microscope (SEM) integrated with an Ocean Optics QE65000 CCD array spectrometer. A schematic diagram of the experimental setup for CL is shown in Figure 3.7. This system includes a parabolic light collector positioned above the sample, optical monochromators, and a hot/cold sample stage for temperature control during CL spectroscopy. The high-energy electron beam, with a diameter smaller than 3 nm, is rastered across the sample surface by the SEM's electron beam scanning system, operating at variable electron energies ranging from 1 to 30 keV.

The parabolic mirror collects the emitted light from the sample and directs it through an optical system to the spectrometer for analysis. The spatial resolution of CL is influenced by factors such as electron beam energy, beam diameter, the stopping power of the sample, and the recombination length of injected carriers. For highly luminous samples, the recombination length (L), determined by carrier lifetime and mobility (both temperature-dependent), defines the spatial resolution. Additionally, a Hamamatsu spectrometer with various grating configurations is used to obtain high-resolution spectra,

especially useful for fine spectral structure examination. The setup allows for sample characterization over a temperature range of 300 K to 10 K using liquid nitrogen, liquid helium, and a cold SEM stage.

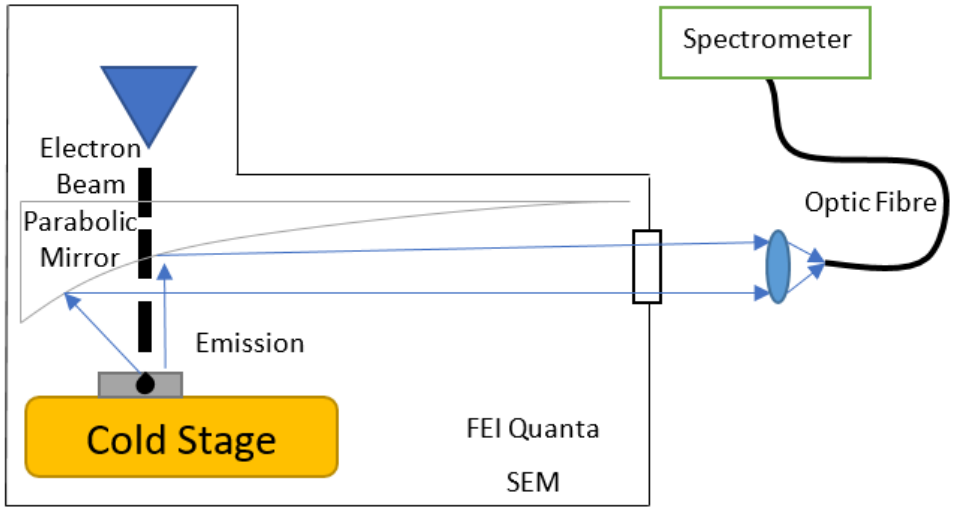

Figure 3.7. Schematic diagram of the experimental setup for CL. [160]

3.3.5.2. Cathodoluminescence Spectrum Correction

All cathodoluminescence (CL) spectra were corrected to account for the overall response of the collection system, using an Oriel 63358 45W quartz tungsten halogen (QTH) lamp. This lamp, with a known emission intensity spectrum versus wavelength, was utilized to correct the intensity of the CL spectral data. The calibration of the lamp was performed by the National Institute of Standards and Technology (NIST) in the United States. The following equation was used to obtain the corrected intensity values:

$$\text{Corrected data} = \text{correction curve} \times \text{measured data} \tag{3.1}$$

For high-resolution wavelength correction, atomic spectral lines from a mercury lamp were measured. The calibrated wavelengths were then converted into energy units (eV) using the equation:

$$E_{photon} = \frac{1239.841856}{\lambda(nm)} \tag{3.2}$$

The conversion of CL intensities to energy space was performed using:

$$I(eV) = \lambda^2 I(nm) \tag{3.3}$$

This equation was then used to convert the wavelength spectra of CL/PL to their corresponding energy spectra.

3.3.5.3. Power-dependent CL

In this study, power-dependent cathodoluminescence (CL) measurements were conducted to examine the recombination kinetics of luminescence centres under varying excitation conditions. The beam current was adjusted while keeping the accelerating voltage constant, allowing the effect of changing excitation power on emission intensity to be assessed. The integrated intensity of each emission peak was calculated through Gaussian fitting of the spectrum.

The relationship between the integrated CL intensity (I_{CL}) and excitation power (P_b) follows a power law, expressed as: [161]

$$I_{CL}\ \alpha\ P_b^n \tag{3.4}$$

Here, n is a power law exponent that reveals the nature of the recombination process. To determine n, the logarithmic values of the integrated intensity log (I_{CL}) and excitation power log (I_b) are plotted, and a linear fit is applied. The value of n indicates the type of recombination: $n \geq 1$ [162] suggests fast processes such as excitonic or band-to-band recombination, while $n < 1$ [163, 164] is indicative of slower processes related to deep-level defects, which may saturate at high excitation powers due to slower recombination rates.

By analysing the power dependence of the CL intensity, we gain valuable insights into the dynamics of the recombination channels, differentiating between rapid band-to-band transitions and slower defect-related recombination processes.

3.3.5.4. Temperature-resolved CL

Temperature-resolved cathodoluminescence (CL) measurements are employed to explore the origins of excitons, optical bandgaps, and defect-related luminescence in semiconductor materials. In this study, the CL system operates over a temperature range from 5 K to 600 K. For temperatures below 80 K, liquid helium is used, while temperatures between 80 K and 300 K are achieved using liquid nitrogen, along with two different thermal controllers and stages.

Typically, as the temperature increases, the luminescence emission peaks broaden due to enhanced electron-phonon interactions. Conversely, at lower temperatures, the peaks narrow. The temperature rise leads to thermal shrinkage of the bandgap, causing a redshift in the emission peaks associated with free excitons and donor-bound excitons. During temperature-dependent CL measurements, there is a competition between bound and free exciton recombination. Bound excitons generally exhibit higher intensity at lower temperatures (below 100 K), while free excitons become more prominent at higher temperatures (above 100 K).

The activation energy for excitonic or non-excitonic recombination processes can be determined through temperature-resolved CL analysis using the Arrhenius relationship:

$$\frac{I}{I_0} = \frac{1}{1+Ce^{E/(kT)}} \tag{3.5}$$

Where I is the intensity at temperature T, I_0 is the intensity at the lowest temperature measured, C is a constant, E is the activation energy, and k is the Boltzmann

constant. This approach provides insights into the temperature-dependent behaviour of the luminescence centres and their associated recombination processes.

Chapter 4. Enhanced Luminescence and Photocatalytic Activity in Highly Inverted Spinel $ZnGa_2O_4$ Nanoplates

In this chapter, a comprehensive characterization of $ZnGa_2O_4$ nanoplates synthesized via the hydrothermal method is presented. The focus is on investigating the effect of anti-site defects on the electronic and optical properties of $ZnGa_2O_4$ nanoplates, and how these properties correlate with the material's photocatalytic performance in degrading Rhodamine B (RhB). Various characterization techniques, such as XRD, TEM, XPS, Raman spectroscopy, and CL, are employed to analyse these properties.

4.1 Abstract

Zinc gallate ($ZnGa_2O_4$) has recently emerged as a promising wide-bandgap material for light emitting and power electronic devices. This study investigates the impact of cation site inversion on the luminescence and photocatalytic properties of $ZnGa_2O_4$. High-quality nanoplates of $ZnGa_2O_4$ with pure spinel phase, lateral dimensions up to 10 μm and thicknesses around 40 nm are synthesized via hydrothermal reaction. Photoemission and Raman spectroscopies reveal significant cation inversion, where Ga^{3+} ions occupy tetrahedral sites (Ga_{Zn}) and Zn^{2+} occupy octahedral sites (Zn_{Ga}), forming anti-site defects. The cation inversion parameters are measured as 0.36 ± 0.04 for Ga_{Zn} and 0.25 ± 0.02 for Zn_{Ga}. The nanoplates exhibit stable, bright broadband luminescence, featuring a UV band at 3.2 eV associated with self-trapped holes and three visible bands attributed to defects. These optical measurements provide crucial insight into the nature and role of defect states, which are key to understanding and enhancing photocatalytic activity. Furthermore, the $ZnGa_2O_4$ nanoplates demonstrate superior photocatalytic efficiency in degrading Rhodamine B (RhB) under ultraviolet A (UVA) irradiation

compared to Ga_2O_3. Band structure analysis reveals strong tail states extending the valence and conduction band edges of Ga_2O_3, reducing the bandgap to 3.9 eV and facilitating hydroxyl radical production for enhanced photocatalysis.

Keywords: spinel $ZnGa_2O_4$; cation inversion; photoemission; broadband phosphor; photocatalysis

4.2. Introduction

Ga_2O_3 and its alloys are gaining considerable attention for applications in power electronics, deep ultraviolet (UV) optoelectronics and phosphors due to their wide bandgap, high critical breakdown fields and intrinsic radiation hardness.[165, 166] Among these alloys, zinc gallate ($ZnGa_2O_4$) stands out as it exhibits a bright, multi-wavelength emission, along with high chemical and structural stability under electron beam irradiation, making it an promising candidate for color displays and photocatalysis.[58, 167, 168] Recent experimental studies have shown that thin films of $ZnGa_2O_4$ can be switched from n-type to p-type conductivity with a hole concentration up to 10^{15} cm^{-3} by adjusting the relative concentrations of Ga and Zn precursors during growth.[8, 9] This is in contrast to monoclinic Ga_2O_3, which exhibits auto n-type conductivity and presents challenges for p-doping.[7] Consequently, $ZnGa_2O_4$ offers great potential as a superior alternative to Ga_2O_3 in phosphor and electronic applications.

In the normal spinel structure of $ZnGa_2O_4$, Zn occupies tetrahedral sites while Ga resides on octahedral sites. However, this spinel compound has a high degree of freedom in compositional design and can adopt an inverted lattice configuration, where Ga atoms occupy tetrahedral sites (Ga_{Zn}) and Zn atoms occupy octahedral sites (Zn_{Ga}), resulting in anti-site defects. This inversion leads to a partially spinel inverse structure, with trivalent Ga^{3+} on tetrahedral sites acting as donors and divalent Zn^{2+} on octahedral sites acting as

acceptors. These stoichiometric defects can significantly influence the electrical and optical properties of $ZnGa_2O_4$, though their precise roles are not completely understood. Experimental studies have reported n-type conductivity in $ZnGa_2O_4$ thin films grown by metal-organic chemical vapour deposition (MOCVD), with electron densities up to 10^{19} cm^{-3} – three orders of magnitude higher than in Ga_2O_3 – and an electron mobility of 5.3 $cm^2\ V^{-1}s^{-1}$ and this unintentional doping has been attributed to both Ga_{Zn} anti-site defects and oxygen vacancies (V_O).[8, 9] Theoretical calculations have shown that Ga_{Zn} and its defect complexes possess the lowest formation energies among the native defects under oxygen-poor conditions,[52, 167] making them the likely source of unintended n-type conductivity. Conversely, under oxygen-rich conditions, Zn_{Ga} and Zn vacancies (V_{Zn}) have the lowest formation energies and act as acceptors, compensating n-type conductivity.[52] Consequently, engineering cation anti-site defects presents a viable self-doping strategy for $ZnGa_2O_4$, eliminating the need for traditional dopants.

Furthermore, defect engineering in oxides has garnered major interest as a means to enhance their photocatalytic performance, with V_O and anti-site defects playing important roles.[169, 170] In oxides, such as TiO_2 and ZnO, these defects can induce intragap states, modify electron-hole recombination rates, or serve as trapping sites to improve the separation of photogenerated carriers.[80, 170-172] In $ZnGa_2O_4$ nanostructures and junctions, defects particularly oxygen vacancies (V_O) have been shown to play an important role in improving photocatalysis and hydroxyl radical generation at the surface.[75, 173, 174] Anti-site defects also play a significant role in photocatalysis, for example, Ga^{3+}-doped ZnO, where Ga substitutes for Zn, improves photocatalytic performance due to enhanced charge carrier separation and increased hydroxyl radical production.[82, 83] Similarly, Zn-doped Ga_2O_3 exhibits higher photodegradation efficiency compared to undoped Ga_2O_3 due to the extended lifetime of trapped carriers in native defect states.[84, 85]

This work investigates the impact of anti-site defects in $ZnGa_2O_4$ on its optical and photocatalytic properties. The synthesized $ZnGa_2O_4$ nanoplates possess a single-phase spinel structure with a high concentration of anti-site defects and exhibit modified band tail states that enhance UVA absorption and photocatalytic efficiency. Cathodoluminescence (CL) analysis reveals UV emission from self-trapped holes (STHs) and defect-associated optical emissions, underscoring the role of anti-site defects in its luminescence properties. This study highlights defect engineering as a viable self-doping strategy, contributing to advancements in semiconductor processing and photocatalytic technologies.

4.3. Results and discussion

$ZnGa_2O_4$ nanoplates were synthesized via a hydrothermal method using a Zn:Ga molar ratio of 0.5. Aqueous solutions of $Ga(NO_3)_3$ and $Zn(CH_3CO_2)_2$ were mixed and adjusted to pH 12 using ethylenediamine, then reacted in a Teflon-lined autoclave at 180 °C for durations ranging from 6 to 48 hours. After centrifugation and drying, the as-prepared samples were annealed in Ar at 800 °C for 2 hours to improve crystallinity. (Full synthesis details are provided in Chapter 3.)

Figure 4.1a show the XRD patterns of the $ZnGa_2O_4$ nanoplates synthesized with hydrothermal treatment times ranging from 6 and 48 hours. The patterns closely match the spinel phase of $ZnGa_2O_4$, with the main diffraction peaks corresponding to the (220), (311), (400), (511) and (440), which are indexed to the spinel structure (JCPDS No. 38-1240). The absence of any detectable ZnO and Ga_2O_3 impurity phases confirms the high phase purity and homogeneity of the spinel phase of the $ZnGa_2O_4$ nanoplates. The similarity between the XRD patterns across different reaction times indicates the successful formation of single-phase spinel $ZnGa_2O_4$ through hydrothermal synthesis.

The average crystallite size (D) of the $ZnGa_2O_4$ nanoplates is analysed using the Sherrer equation,[175] based on the most intense (311) XRD peak obtained from standard Bragg–Brentano geometry. The FWHM values are extracted by fitting the XRD peak with a Lorentzian function (Figure 4.1b). The (311) peak is shifted to a higher 2θ angle for 48 hours reaction time, indicating a reduction in the lattice parameter. The lattice parameter a is determined to be 0.8290, 0.8281, 0.8292, and 0.8254 nm for the 6, 12, 24, and 48 hours reaction times, respectively, using the d311 spacing. [176] This reduction likely arises from the substitution of a large Zn^{2+} ions with smaller Ga^{3+} ions in the lattice. Figure 4.1c presents the FWHM values and corresponding crystallite sizes for the synthesized nanoplates, showing that the crystallite size increased to 34 nm at 24 hours, followed by a decrease to 28 nm at 48 hours, likely due to the material redissolution under prolonged reaction conditions.[177] The dependence of crystallite size on hydrothermal reaction time has been attributed to the crystallization process of spinel microstructures.[178] The $ZnGa_2O_4$ nanoplates synthesized at a reaction time of 24 hours, which exhibit the sharpest XRD peaks and the largest crystallite size of 34 ± 3 nm, were selected for further analysis. Their high crystalline quality is essential for investigating the impact of cation site inversion on the luminescence and photocatalytic properties of $ZnGa_2O_4$, as crystallinity could influence carrier kinetics and defect-related luminescence emission. It is noted that the calculated crystallite size refers to the coherent domain size along the [311] direction and not to the lateral dimensions of the nanoplates.

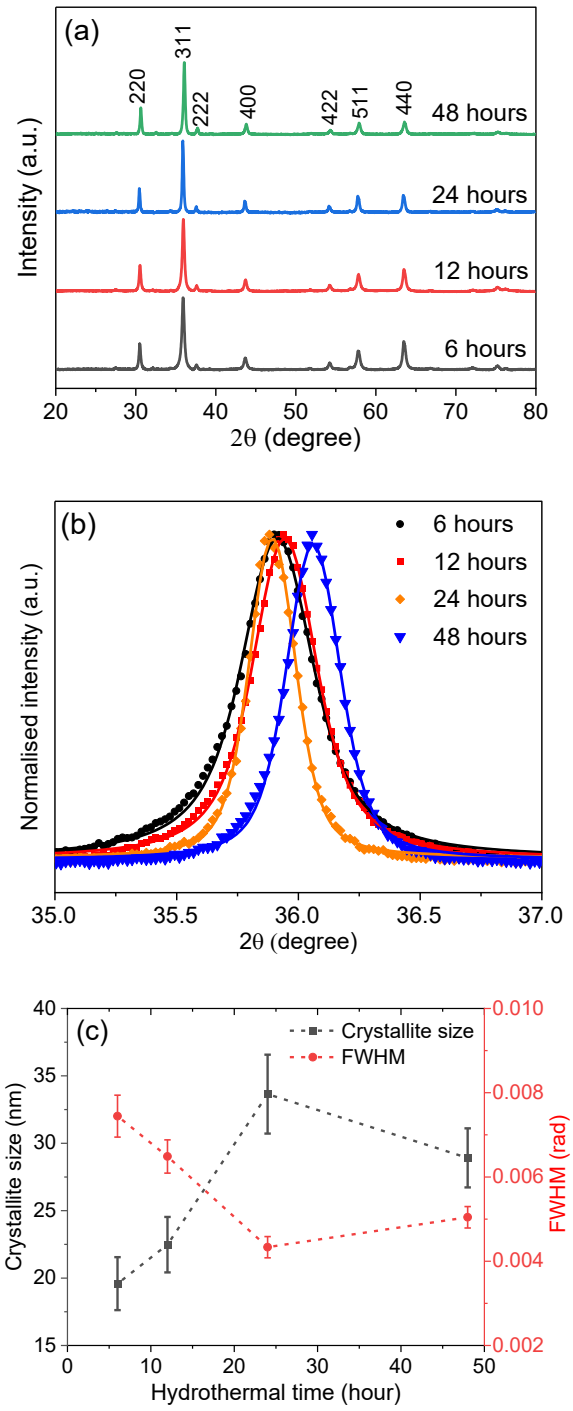

Figure 4.1. (a) XRD patterns of $ZnGa_2O_4$ nanoplates synthesized at different hydrothermal reaction times (6 and 48 hours). (b) Symmetrical (311) XRD profile of the $ZnGa_2O_4$ nanoplates synthesized for a hydrothermal reaction time at 6, 12, 24, and 48 hours. Lorentzian fitting of the profiles provides integral peak widths (β), revealing the narrowest profile and highest crystallinity at 24 hours. (c) Variations of the FWHM of the (311) peak and the crystallite size as a function of reaction time, showing that the largest crystallite size of 34 ± 3 nm is achieved after 24 hours.

The SEM and AFM images in Figure 4.2a, b show that the synthesized $ZnGa_2O_4$ nanoplates have lateral dimensions ranging from 1 to 10 μm and thicknesses between 40 and 50 nm, with a roughness of 3.2 nm measured over an area of 5 × 5 μm^2. TEM and SAED analyses reveal the highly crystalline nature of the nanoplates. The bright field TEM image in Figure 4.2c shows that the nanoplate is comprised of aligned, overlapping platelets with diameters between 200 to 1000 nm. The accompanying SAED pattern displays Bragg spots indexed to the spinel structure with the Fd3m space group and a unit cell parameter of 0.82 nm. This value slightly smaller than the reported value of 0.8335 nm for normal spinel $ZnGa_2O_4$, likely due to the substitution of Zn^{2+} ions with smaller Ga^{3+} ions in the lattice.[179] The HRTEM images in Figure 4.2d reveal lattice spacings of 0.29 and 0.25 nm, corresponding to the (220) and (311) planes of spinel $ZnGa_2O_4$, respectively. The EDX spectrum in Figure 4.2e confirms the presence of Zn, Ga and O in the nanoplates, with no detectable impurities. Quantitative EDX microanalysis suggests a Zn deficiency of up to 15 at%, likely due to the higher volatility of Zn compared to Ga during growth, consistent with previous studies.[180, 181] The Raman spectrum in Figure 4.2f displays two dominant peaks at 415 and 345 cm^{-1}, corresponding to A_{2u} and E_g modes of cubic spinel $ZnGa_2O_4$, respectively.[182] Additionally, the peaks at 474 and 608 cm^{-1} have been attributed to the T_{2g} modes, while the broad peak at 710 cm^{-1} is associated with the A_{1g} mode.[183, 184] Notably, the observed peaks at 628, 653 and 765 cm^{-1}, which are absent in the normal $ZnGa_2O_4$ spinel structure,[185] have been previously reported and assigned to the stretching and bending modes of GaO_4 tetrahedra.[186-188] The observed Raman peaks associated with GaO_4 tetrahedra provide strong evidence of Ga^{3+} ions occupying tetrahedral sites, indicating a partially inverted spinel structure in the $ZnGa_2O_4$ nanoplates. The A_{2u} mode, which is typically silent in Raman spectroscopy, becomes active due to

local symmetry breaking induced by antisite defects, resulting in its observation in the spectrum.[189] These high-frequency Raman peaks are tentatively assigned to Ga^{3+} ions occupying Zn tetrahedral sites. This inversion, a common phenomenon in spinel compounds, occurs when Ga^{3+} occupies both tetrahedral and octahedral lattice sites and $ZnGa_2O_4$ is known to accommodate on ordered structure with an inversion parameter of up to 0.3.[190]

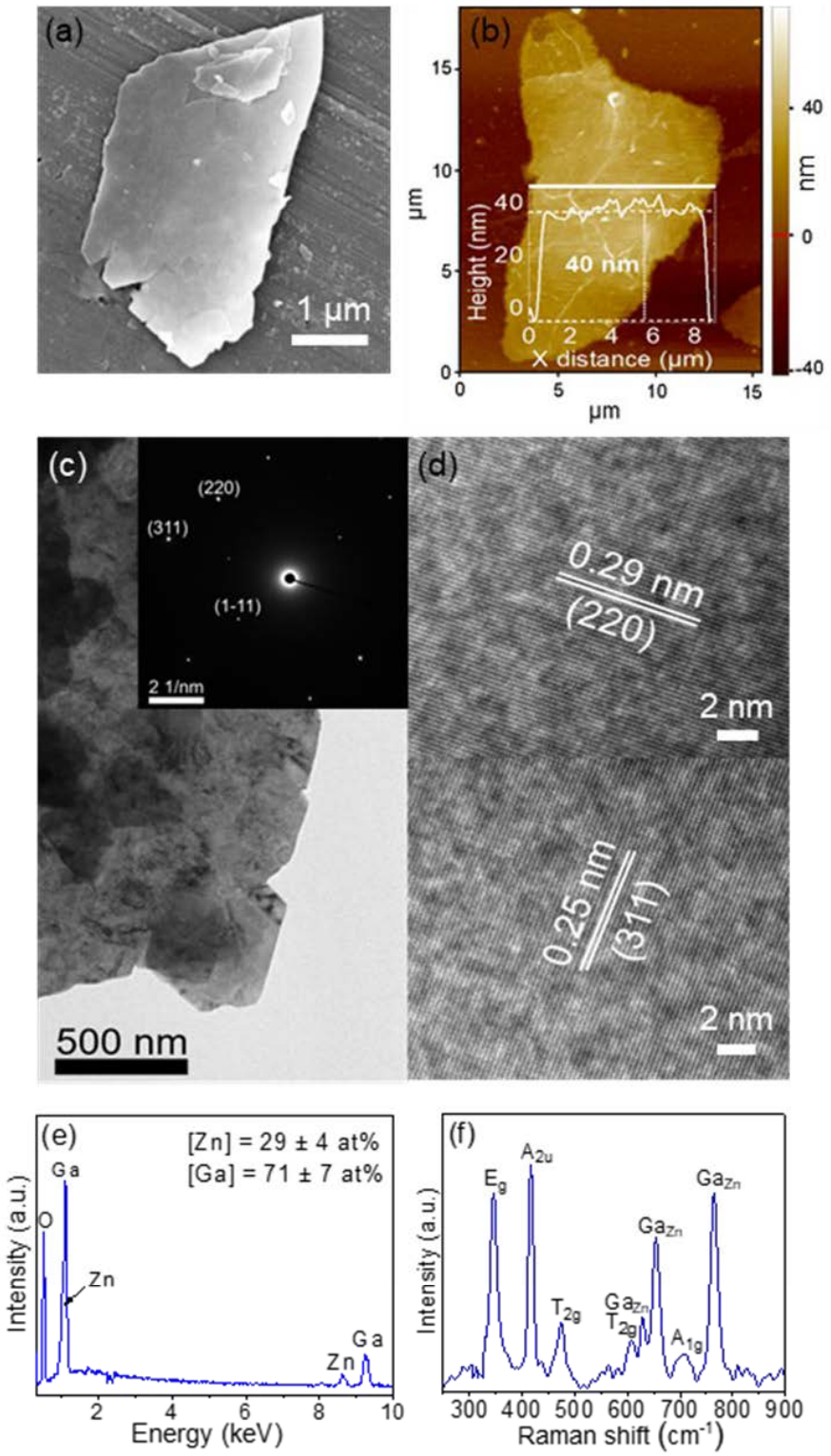

Figure 4.2. (a, b) SEM and AFM images of $ZnGa_2O_4$ nanoplates synthesized after 24 hours hydrothermal reaction, displaying lateral sizes between 1 to 5 µm. The inset in (b) shows the AFM height profile along the line in the image, revealing a thickness of 40 ± 4 nm. (c, d) Low- and high-resolution TEM images of a nanoplate and corresponding SAED pattern along the [-112]

zone axis. The two HRTEM images show lattice fringes for the (220) and (311) planes, with respective lattice spacings of 0.29 and 0.25 nm, confirming the single crystalline nature. (e) EDX spectrum (E_{beam} = 20 kV) showing characteristic X-ray emissions of Zn, Ga and O, with the Zn and Ga atomic percentages calculated from 15 samples. (f) Raman spectrum, showing vibrational modes of spinel $ZnGa_2O_4$, with three additional peaks at 629, 654 and 765 cm-1 attributed to anti-site defects.

Figure 4.3a, b presents the XPS spectra of Zn 2p and Ga 3d core levels for the $ZnGa_2O_4$ nanoplates. Both spectra exhibit asymmetrically broadened peaks towards the high binding energy side, suggesting that Zn^{2+} and Ga^{3+} ions occupy more than one of the available coordination sites. The Zn 2p spectrum is deconvoluted into two sets of doublets corresponding to Zn ions on the tetrahedral (ZnO_4) and octahedral (ZnO_6) sites, with Zn $2p_{3/2}$ peaks located at 1021.9 eV and 1023.9 eV, respectively, as shown in Figure 4.3a. The spin-orbit splitting of Zn $2p_{3/2}$ and $2p_{1/2}$ is kept constant at 23.1 eV for both sites during the fitting process. Similarly, the Ga 3d spectrum is deconvoluted into four peaks corresponding to Ga $3d_{3/2}$ and $3d_{5/2}$ at octahedral and tetrahedral sites, with the main Ga $3d_{3/2}$ peak located at 20.9 and 22.6 eV. The obtained binding energies align well with previously reported values.[9, 191] Peak fitting analysis yields cation inversion parameters (defined as the fraction of divalent cations on octahedral sites or trivalent cation on tetrahedral sites) of 0.25 ± 0.02 for Zn^{2+} and 0.36 ± 0.04 for Ga^{3+} ions. The lower inversion parameter for Zn^{2+} is consistent with the Zn deficiency observed in the EDX microanalysis. The O 1s and valence band (VB) spectra of the nanoplates are shown in Figure 4.3c, d. The O 1s spectrum which is acquired at a photon energy of 1486.6 eV, is deconvoluted into three peaks, representing lattice O^{2-} ions at a binding energy of 530.6 eV, O^{2-} ions with a nearby V_O at 532.1 eV, and surface hydroxyl groups (^{-}OH) groups at 533.0 eV.[192] The deconvolution indicates that high concentrations of V_O and surface ^{-}OH,

as expected for solution-processed nanoplates. The valence band of these nanoplates resolved into three Gaussian peaks, which can be attributed to pure O 2p states (peak I), hydridized O 2p and Zn 3d (peak II), and hydridized O 2p and Ga 3d (peak III). A linear extrapolation of the valence band spectrum reveals that the Fermi level is located at 2.4 eV above the valence band edge.

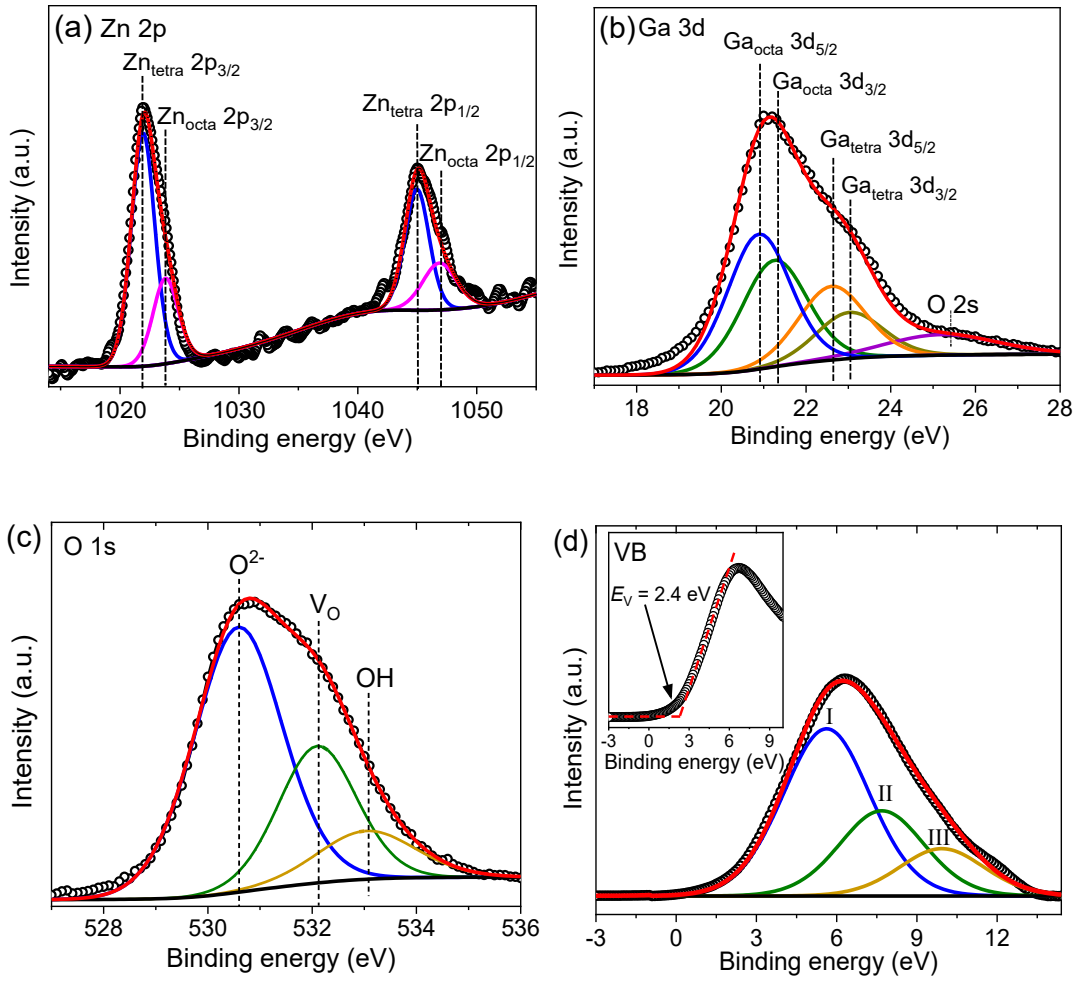

Figure 4.3. XPS spectra of (a) Zn 2p and (b) Ga 3d for the $ZnGa_2O_4$ nanoplates. The Zn 2p doublet is deconvoluted into four Gaussian peaks, corresponding to the $2p_{1/2}$ and $2p_{3/2}$ levels of Zn atoms occupying the tetrahedral and octahedral sites. Similarly, the Ga 3d spectrum is fitted with four components representing the Ga $3d_{3/2}$ and $3d_{5/2}$ levels for Ga atoms at octahedral and tetrahedral sites. The Ga 3d spectrum partially overlaps with the O 2s signal. (c) O 1s spectrum of the synthesized $ZnGa_2O_4$ nanoplates is fitted using a Shirley background and three peaks

corresponding to three different chemical states of oxygen: lattice O^{2-} ions, O^{2-} with a nearby oxygen vacancy (V_O) and surface hydroxyl groups (^{-}OH). (d) a linear extrapolation of the valence band spectrum reveals that the Fermi level is located at 2.4 eV above the valence band edge.

NEXAFS spectra of $ZnGa_2O_4$ and Ga_2O_3 collected in TEY mode illustrated in Figure 4.4 revealing unoccupied electronic states in the CB. In the Ga L_3-edge spectrum of Ga_2O_3 (figure 4.4a), absorption peaks are observed at 1119.6 eV (Ga_1), 1121.9 eV (Ga_2) and 1124.0 eV (Ga_3), corresponding to Ga 4*s*, 3*d*, and 4*p* states hybridized with oxygen. [193] For $ZnGa_2O_4$, these peaks broaden and shift to lower energies due to structural disorder caused by the substitution of trivalent Ga^{3+} for divalent Zn^{2+}, resulting in a ~0.4 eV downward shift of the CB edge compared to Ga_2O_3. In the O K-edge spectrum (Figure 4.4b), both materials exhibit a peak at 535.4 eV (peak O_1), assigned to antibonding orbitals from by the hybridization of O 2*p* states with Ga 4*s* and Zn 4*s* states. The peaks between 539.4 eV and 548.3 eV (O_2 to O_4) correspond to O 2*p* orbitals hybridized with Ga and Zn orbitals. [194, 195] The peak intensities vary significantly between the two materials due to differing oxygen coordination in monoclinic Ga_2O_3 and spinel $ZnGa_2O_4$. Notably, the O-derived CB edge of $ZnGa_2O_4$ also shifts to a lower energy by ~0.5 eV, similar to the Ga spectra. Finally, the Zn L_3-edge spectrum (Figure 4.4c) display four peaks at 1023.5, 1026.3, 1032.3 and 1036.1 eV, corresponding to unoccupied Zn *s*- and *d*-derived states. [195]

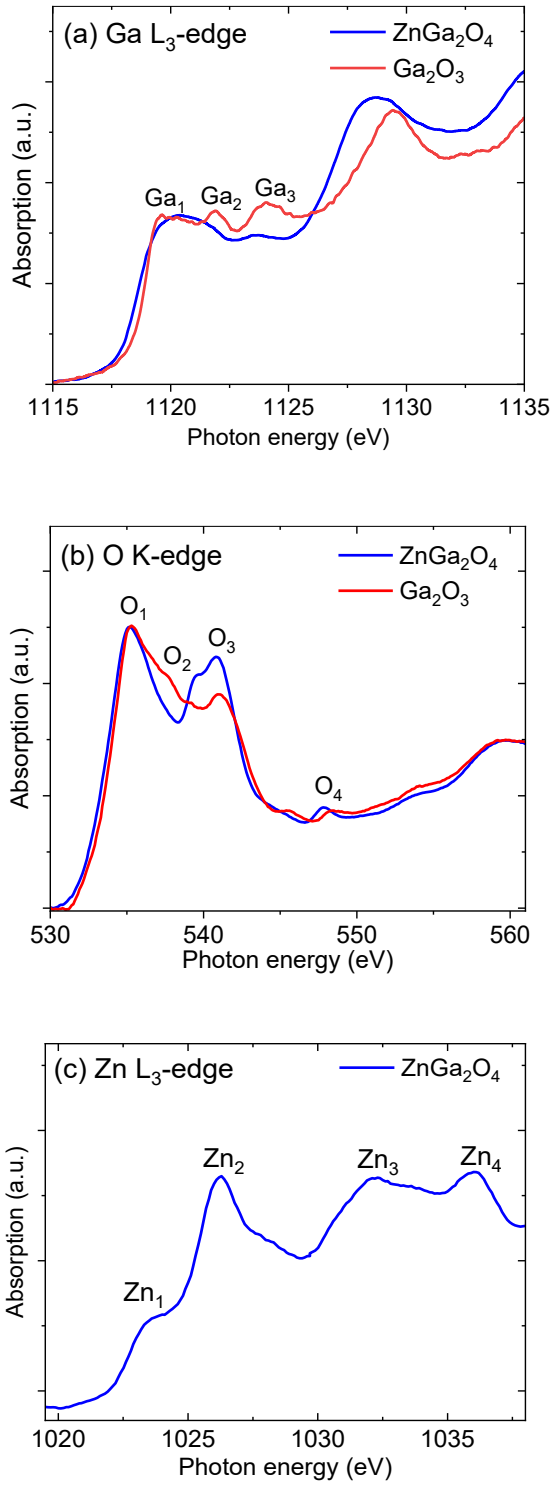

Figure 4.4. NEXAFS spectra of (a) Ga L3-edge, (b) O K-edge and (c) Zn L3-edge collected in TEY mode for $ZnGa_2O_4$ and Ga_2O_3, revealing unoccupied electronic states in the CB.

The optical properties of the $ZnGa_2O_4$ nanoplates are investigated using UV-Vis optical absorption spectroscopy (Figure 4.5a). The nanoplates exhibit high transparency in the UV and visible regions, with a sharp absorption edge at ~ 320 nm. A Tauc analysis yields a bandgap of 3.9 ± 0.1 eV. The luminescence properties of the spinel $ZnGa_2O_4$ nanoplates are further investigated by temperature-resolved CL microanalysis as presented in Figure 4.5b-d. The 24-hour nanoplates were chosen for these analyses because its highest crystallinity. The spectra reveal a distinct intrinsic UV peak at 3.2 eV and an asymmetric, broad visible band centred around 2.26 eV, composed of three overlapping defect-related luminescence peaks. In $ZnGa_2O_4$, holes can be spontaneously self-trapped and recombine radiatively, producing the broad UV emission band, which aligns well with density functional theory (DFT) calculations.[52, 167] The visible band is attributed to three emission peaks arising from radiative recombination channels involving V_O, V_{Zn} and anti-site defects.[167]

The CL spectra are deconvoluted into four peaks, using reported peak positions from the literature. [66, 191, 196] Fitting the UV peak with a Gaussian function yields E_{UV} = 3.2 eV and $FWHM_{UV}$ = 0.76 eV as depicted in Figure 4.5c. This large FWHM for the UV peak is expected since the hole-trapped polaron state is strongly coupled to the lattice, resulting in a broad Gaussian line shape. The green 2.25 eV band at 80 K is fitted with three defect-related Gaussian-like peaks: red luminescence (E_{RL} = 1.75 eV, FWHM = 0.60 eV) and yellow (E_{YL} = 2.07 eV; FWHM = 0.6 eV) and green luminescence (E_{GL} = 2.32 eV; FWHM = 0.67 eV). The broad FWHM of these bands is a common characteristic of defect-related emissions due to their strong electron-phonon coupling with the lattice. The dominant GL emission has been ascribed to Ga_{Zn},[191] consistent with the high degree of Ga inversion in the nanoplates. The RL band has been attributed to V_O defects in the GaO_6 octahedron, resulted from the migration of the O atom from its lattice site,[197] as it emerged

after annealing at ~ 800 °C.[191, 198] This assignment for the RL consistent with our XPS results, which reveal a high concentration of V_O defects in the annealed nanoplates.

Arrhenius analysis of the UV, GL, YL and RL emission band intensities versus temperature is performed to determine the thermal activation energy of their electronic transitions as illustrated in Figure 4.5d. The presence of two distinct linear temperature ranges spanning from 80 to 160 K and 160 to 280 K for both YL and UV bands indicates the existence of two separate activation processes. Activation energies are obtained by fitting straight lines to each of the linear regions over the lower and upper temperature ranges, and the results are summarized in Table 4.1. The weak temperature dependence of the RL suggests that this emission is associated with a phonon-assisted excitation of the GaO_6 site.[198] The temperature profiles of the defect-related YL and GL are completely different, confirming they originate from different electronic transitions. Notably, the YL and UV bands above 160 K, as well as the GL band over the entire temperature range, exhibit remarkably similar activation energies of 10 ± 2 meV, which is comparable with the value estimated for the charge carrier activation in the electrical conduction of $ZnGa_2O_4$ thin films.[8] This similarity suggests that optical transitions in the $ZnGa_2O_4$ nanoplates are mediated by a shallow electronic state, likely associated with Ga_{Zn} donors that act as a competitive recombination center.

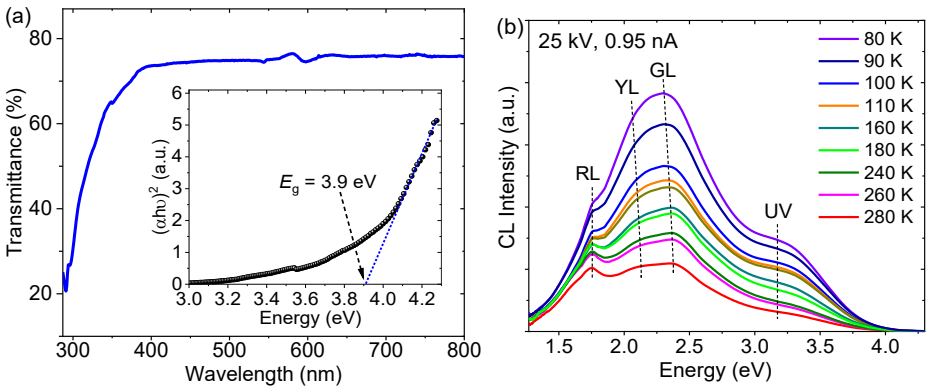

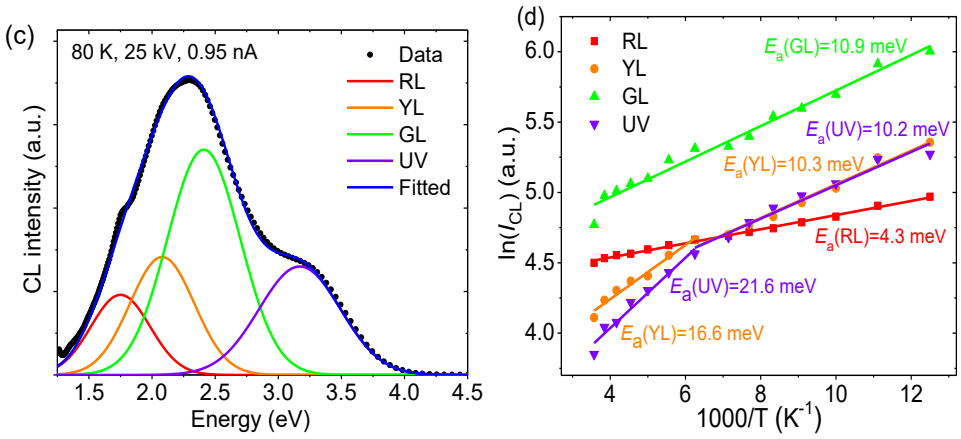

Figure 4.5. (a) Optical transmission spectrum of the synthesized $ZnGa_2O_4$ nanoplates showing transmission of ~ 75% at wavelengths below 390 nm. Inset presents the Tauc plot indicating a bandgap $E_g = 3.9 \pm 0.1$ eV. (b) Temperature-resolved CL spectra of the $ZnGa_2O_4$ nanoplates over the temperature range from 80 K to 280 K. (c) Typical CL spectrum resolved into four Gaussian peaks centred at 1.8, 2.1, 2.3, and 3.2 eV, which represent RL, YL, GL, and UV emission bands, respectively. (d) Arrhenius plots of $\ln(I_{CL})$ versus 1000/K and linear analysis for the four emission bands, yielding the thermal activation energies (E_a) displayed within the graph.

Table 4. 1. Activation energies derived from the Arrhenius analysis of the integrated peak intensities for RL, YL, GL, and UV luminescence bands.

Peak	**Activation energy (meV)**	
	Below 160 K	Above 160 K
RL 1.8 eV	4.3 ± 0.2	
YL 2.1 eV	16.6 ± 2.4	10.3 ± 1.2
GL 2.3 eV	10.9 ± 0.9	
UV 3.2 eV	21.5 ± 3.5	10.2 ± 1.5

Carrier recombination kinetics of the $ZnGa_2O_4$ nanoplates is further investigated using excitation power-dependent CL analysis (Figure 4.6). Here, the CL peak intensities

are measured as a function of e-beam current, which is increased from 0.15 to 29.4 nA, while the beam energy (E_B = 25 keV) remained constant. No noticeable changes in the peak positions and spectral shape of all four emissions were observed, indicating that the nanoplates are highly colour-stable phosphors under electron beam irradiation. Figure 4.6b shows the recombination kinetic behaviours of the four emission peaks in a log-log plot using the power-law model $I_{CL} \propto I_B^k$, where I_{CL} and I_B refer to the integrated intensity of an emission band and the e-beam current, respectively.[160] The power law fits yield the exponent k between 0.59 and 0.68 (± 0.05) for the RL, YL and GL bands; these strongly sublinear dependences confirm these emissions originate from strongly lattice-coupled deep defect levels. [52, 199] Furthermore, the UV band has a sublinear dependence on excitation power, with $k \approx 0.71$, consistent with the localized nature of the self-trapped holes.[52] $ZnGa_2O_4$ phosphors typically exhibit emission in the UV and blue range, peaking in the range of 2.8 to 3.4 eV, and doping this material with transition metals such as Cr, Mn or Eu has been a general approach to realize full colour emission in the visible range.[200-202] This work demonstrates that strong, broadband emission from red to green in $ZnGa_2O_4$ can be achieved by engineering anti-site defects without the utilization of a dopant.

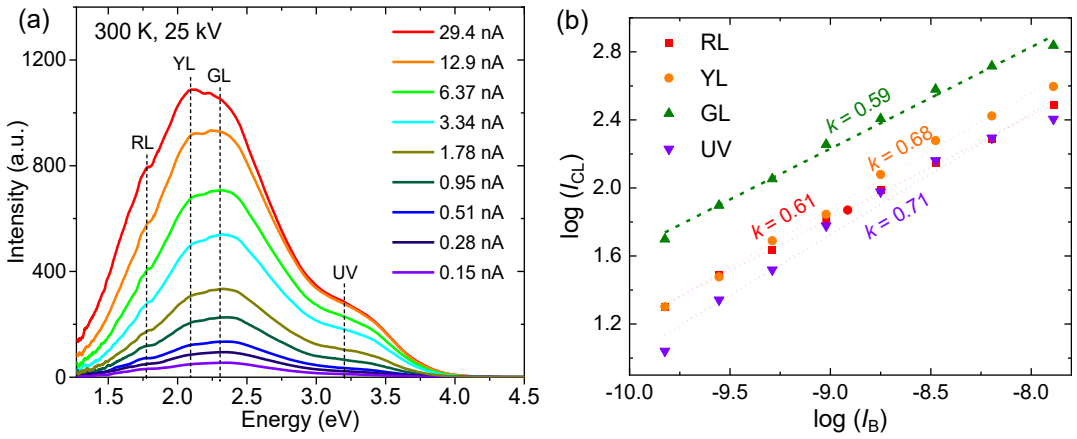

Figure 4.6. (a) Excitation power-resolved CL spectra for the $ZnGa_2O_4$ nanoplates acquired at V_B = 25 keV, I_B = 0.15 – 29.4 nA. (b) Analysis of the integrated peak intensities of the four fitted bands using the power-law model (I_{CL} □ I_B^k). Dashed lines are power law fits to the data, which yields the exponent value k between 0.59 and 0.71 (± 0.05). Carrier recombination involving self- trapped holes and deep levels, such as free-to-bound transitions, typically shows sublinear relationship with excitation power with k < 1 due to their strong lattice coupling [199]. This result is consistent with theoretical assignments of the UV to self-trapped holes and visible bands to deep defect levels in $ZnGa_2O_4$. [52]

The photocatalytic activities of $ZnGa_2O_4$ and Ga_2O_3 are evaluated by monitoring the photodegradation of RhB under UVA light (Figures 4.7 and Figure 4.8). The control experiment, conducted with RhB in the absence of a photocatalyst, shows minimal spectral changes, indicating weak photo-dissociation of RhB under UVA irradiation alone [Figure 4.7a].[75] In contrast, the $ZnGa_2O_4$ nanoplates exhibit substantial photocatalytic performance, reducing the RhB concentration by 91% after 90 minutes (figure 4.8a). During the degradation process, a blueshift in the absorbance peak was observed and the color of the RhB solution gradually changed from pink to colorless (Figure 4.7c). This transformation can be attributed to the formation of degradation intermediates with different optical properties and the cleavage of the conjugated chromophore structure of

RhB during photocatalysis.[203] The degradation kinetics follow a first-order reaction behavior, with the rate constant k is calculated using the rate law, $\ln (A_t/A_o) = -kt$. The rate constant for $ZnGa_2O_4$ is determined to be $k = 0.026$ min^{-1}, significantly higher than the control experiment ($k = 0.002$ min^{-1}) and for Ga_2O_3 ($k = 0.016$ min^{-1}), highlighting the higher photocatalytic efficiency of $ZnGa_2O_4$. The k value for the $ZnGa_2O_4$ nanosheets is comparable to previously reported values of ~ 0.03 min^{-1} under UV light irradiation.[204, 205]

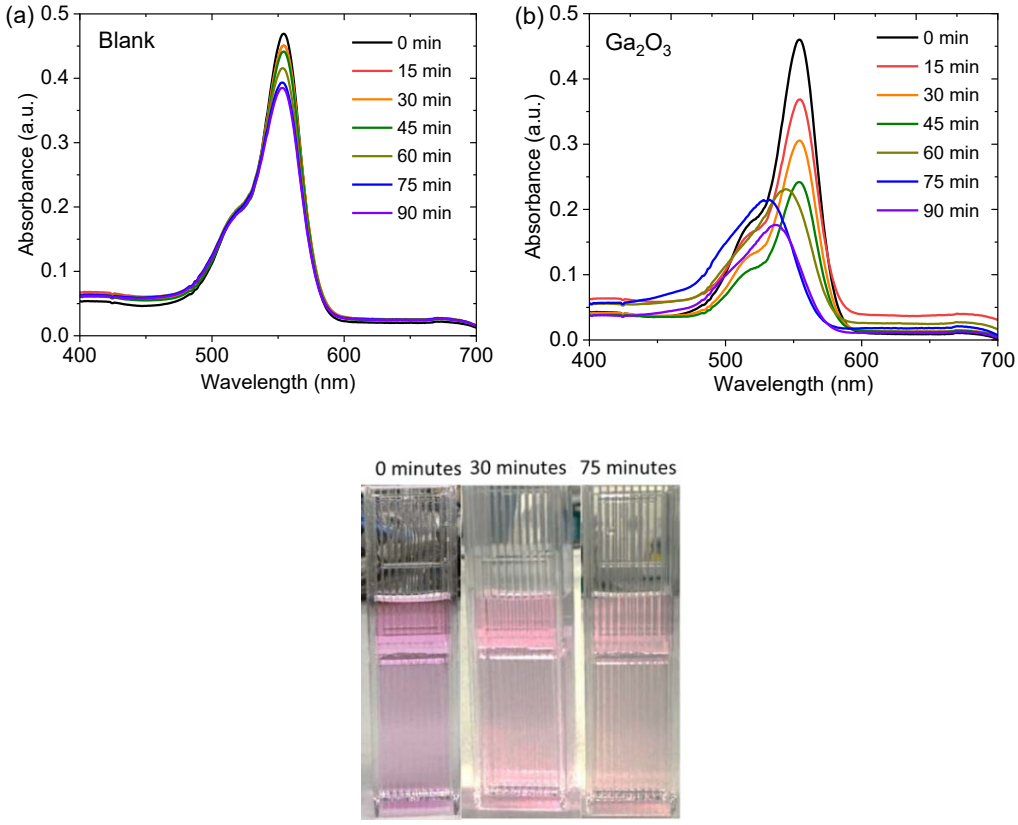

Figure 4.7. (a) Absorption spectra of a 5 μM RhB solution under UVA irradiation without a photocatalyst at various time intervals. While no spectral shift is observed, there is a slight decrease in the characteristic absorption peak at 554 nm, indicating minimal photodegradation of RhB. (b) Absorption spectra of the RhB solution in the presence of Ga_2O_3 photocatalysts, showing a gradual redshift with irradiation time and a photocatalytic degradation effect. (c) discoloration of the RhB solution as a function of UV irradiation time in the presence of $ZnGa_2O_4$ nanoplates.

To investigate the impact of the structural disorder in $ZnGa_2O_4$ on its electronic structure and photocatalytic activity, we analyze the band structures of $ZnGa_2O_4$ and Ga_2O_3 based on the their valence band and O K-edge NEXAFS spectra [Figure 4.8(c)]. Detailed analysis of the unoccupied electronic states of the $ZnGa_2O_4$ CB is provided in Figure 4.4. In Figure 4.8c, the NEXAFS spectra are normalized and aligned according to with the experimentally measured bandgaps (3.9 eV for $ZnGa_2O_4$ and 4.8 eV for Ga_2O_3).[206, 207] The zero eV point on the common axis, aligned with the Fermi level E_F, is determined from the VB photoemission measurement. Near E_F level, two distinct CB peaks and one VB peak are observed, with comparable positions for $ZnGa_2O_4$ and Ga_2O_3. However, $ZnGa_2O_4$ exhibit pronounced band tailing, extending the CB edge closer to the E_F. This band tailing is attributed to the high densities of Ga_{Zn} and V_O defects as revealed by the CL characterization results, which create a continuum that merges with the CB, contributing the Urbach energy. It is known that the Urbach energy plays a crucial role in enhancing the photocatalytic activity by facilitating the generation of trapped electrons and holes as well as increasing optical absorption through band-to-tail and tail-to-tail transitions.[208] During the degradation process, RhB is oxidized directly by holes in the VB, while highly reactive hydroxyl radicals ($^{\bullet}OH$) are generated either through water decomposition or the reaction of holes with hydroxyl groups (OH^-).[84, 208] Simultaneously, photogenerated electrons strongly interact with O_2, leading to the formation of superoxide radicals ($^{\bullet}O_2^-$).[84] The $^{\bullet}OH$ and $^{\bullet}O_2^-$ radicals drive the oxidative degradation of RhB, breaking it into smaller intermediates and sustaining the process until the complete mineralization of RhB into CO_2 and H_2O.[205] Both V_O and Zn_{Ga} are deep-level defects and can act as electron acceptors during photocatalytic degradation, temporarily trapping electrons, which further suppresses electron-hole recombination and improves photocatalytic efficiency. Moreover, the significant defect-induced band tailing in the

$ZnGa_2O_4$ nanoplates enhances light absorption and photocatalytic activity in the UVA region. The improved separation of photogenerated electrons and holes, coupled with the broader light absorption range, ultimately leads to the superior photocatalytic performance of the $ZnGa_2O_4$ nanoplates.

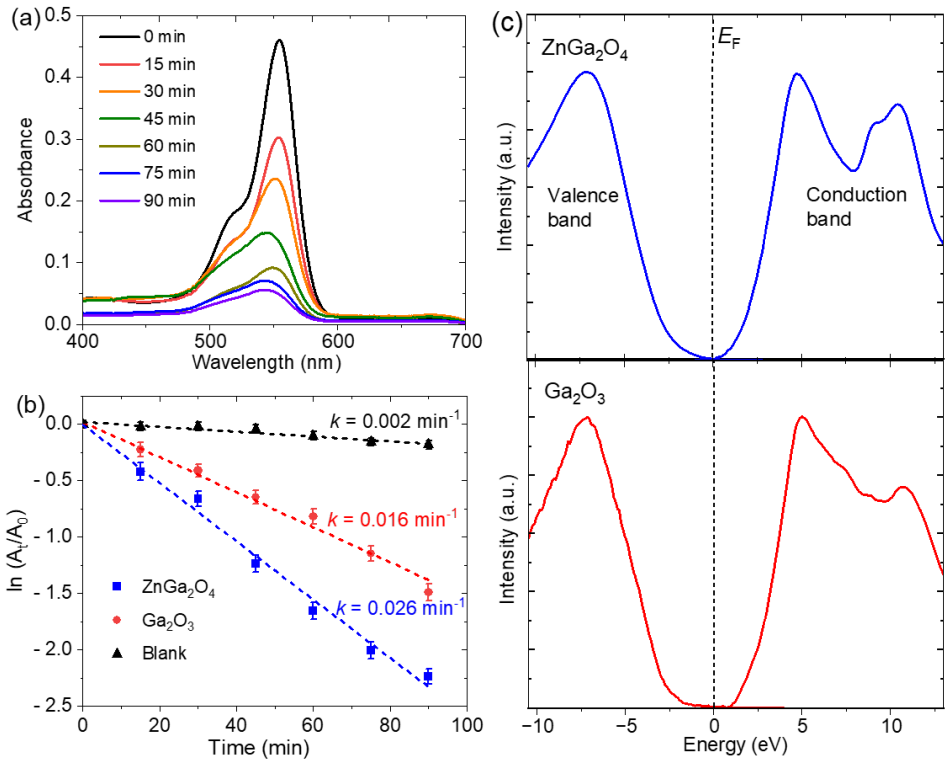

Figure 4.8. (a) Absorption spectra of a 5 μM RhB solution with $ZnGa_2O_4$ photocatalysts at various UV irradiation times between 0 and 90 minutes. (b) Degradation kinetics of RhB in the presence of $ZnGa_2O_4$ and Ga_2O_3, compared with the control experiment (absence of photocatalysts). (c) Band structures of $ZnGa_2O_4$ and Ga_2O_3 derived from valence band photoelectron and O K-edge NEXAFS spectra, presented on a common energy axis.

4.4. Conclusions

In summary, $ZnGa_2O_4$ have been successfully fabricated using a hydrothermal growth method, and post-growth annealing resulted in highly crystalline quality, pure spinel-phase nanoplates. Photoemission and Raman spectroscopy reveal the presence of both

octahedral Zn^{2+} and tetrahedral Ga^{3+}, leading to a partially inverse spinel structure with a cation inversion parameter up to 0.36. The $ZnGa_2O_4$ nanoplates exhibit stable and bright broadband luminescence over the UV and visible ranges, characterized by four emission bands: UV, green, yellow and red. The activation energy of the UV emission, associated with self-trapped holes, is determined to be 10 ± 2 meV. This energy value aligns with the defect-related green and yellow emissions, indicating that optical transitions in the inverse $ZnGa_2O_4$ structure are mediated by a shallow electronic state, likely associated with anti-site Ga_{Zn}. These results highlight the role of spinel cation site inversion in the optical properties of $ZnGa_2O_4$ phosphors. The superior photocatalytic performance of $ZnGa_2O_4$ nanoplates, compared to Ga_2O_3, in the photodegradation of RhB under UVA irradiation is primarily due to the formation of Urbach energy induced by high densities of Ga_{Zn} and Zn_{Ga} defects. These defects enhance the UVA light absorption and improve charge carrier generation, thereby improving photocatalytic efficiency. These findings underscore defect engineering as an effective self-doping strategy for semiconductor processing and photocatalytic technologies.

Chapter 5. Bandgap Tuning of β-$(Al_xGa_{1-x})_2O_3$ Nanosheets via Liquid Metal Interface Engineering

This chapter investigates the exfoliation of β-$(Al_xGa_{1-x})_2O_3$ nanosheets with a high Al concentration using liquid metals. The focus is on engineering the bandgap of β-$(Al_xGa_{1-x})_2O_3$ nanosheets by controlling the concentration of Al in the exfoliated nanosheets. In addition, the effect of incorporating a high Al concentration in β-$(Al_xGa_{1-x})_2O_3$ nanosheets on their optical properties is studied. The chapter presents the use of various characterization techniques, such as XRD, TEM, XPS, EELS, UPS, Raman spectroscopy, and CL, to analyse these properties.

5.1 Abstract

Precise engineering of the electronic band structure in 2D metal oxides is essential for advancing optical and electronic nanodevices, yet achieving compositional control at the nanoscale remains challenging. Here, a low-temperature liquid metal-based synthesis method is used to fabricate β-$(Al_xGa_{1-x})_2O_3$ nanosheets with tuneable composition (x = 0 – 0.88). This approach enables selective aluminium enrichment in nanosheets while preserving the monoclinic crystal structure and adopting the (-201) orientation, similar to conventional β-Ga_2O_3 thin films. The synthesized nanosheets exhibit large lateral dimensions (> 100 μm) and an average thickness of 3.2 ± 0.5 nm, making them suitable for nanoscale device applications. By varying the Al content from 0 to 10 at% in the liquid metal, the bandgap is tuned from 4.50 eV (pure β-Ga_2O_3) to 6.41 eV (β-$(Al_{0.88}Ga_{0.12})_2O_3$). The β-$(Al_xGa_{1-x})_2O_3$ nanosheets retain key β-Ga_2O_3 characteristics, including self-trapped hole formation, ensuring structural and electronic integrity. The liquid metal synthesis method overcomes limitations of conventional deposition techniques, offering a scalable

approach for tailoring 2D metal oxide properties and enabling bandgap-engineered optoelectronic applications.

Keywords: 2D materials; β-AlGaO; monoclinic oxide semiconductors; liquid metal synthesis; bandgap engineering

5.2 Introduction

Ga_2O_3 is an wide bandgap semiconductor with excellent chemical stability, high UV transparency, a large breakdown electric field, making it highly promising for high-power electronics, UV photodetectors and optoelectronics.[4, 209, 210] Bandgap engineering plays a critical role in optimizing the optical and electronic properties of Ga_2O_3, enabling tuneable photodetectors, wavelength-selective optical filters and high-efficiency power devices.[12] Expanding the bandgap range enhances device flexibility, improving operational efficiency and performance. One effective approach to bandgap modulation is making compounds of Ga_2O_3 together with materials such as In_2O_3, ZnO, Al_2O_3 and GaN.[96, 211] Among these, Al_2O_3 (bandgap ~ 8.7 eV) is particularly advantageous due to the similar electronic structures of Al and Ga, which enable seamless incorporation of Al into the β-Ga_2O_3 lattice. As a result, β-$(Al_xGa_{1-x})_2O_3$ alloys is attractive for high power electronics and deep UV photodetectors.[212] However, conventional synthesis techniques for Al incorporation, such as molecular beam epitaxy (MBE) and metal-organic chemical vapor deposition (MOCVD), require high-temperature processing and complex vacuum-based deposition, limiting scalability and bandgap control. The highest Al incorporation achieved in β-$(Al_xGa_{1-x})_2O_3$ has been reported as ~48% via MOCVD,[213] with reports of up to 61% in specific orientations using MBE.[16, 17]

Liquid metal-based synthesis offers an alternative route for fabricating $(Al_xGa_{1-x})_2O_3$. This low-temperature, vacuum-free method enables direct and efficient oxide formation at the liquid metal interface, allowing precise control over Al incorporation, even at high Al *x*-fraction levels, by leveraging the selective surface oxidation of liquid metals to form atomically thin oxides with tailored compositions.[18, 155] In Ga-based liquid metal alloys, elements with lower Gibbs free energy of oxide formation (ΔG_f) preferentially migrate to the surface, where they undergo spontaneous oxidation. This surface-directed oxidation enables the formation of ultrathin oxide nanosheets with tunable stoichiometry. For example, Al, Gd, and Hf exhibit strong segregation tendencies in Ga-based melts, forming Al_2O_3, Gd_2O_3 and HfO_2, respectively.[18] Similar principles have been used to synthesize mixed oxide systems such as indium tin oxide (ITO) and Ga–Sn–Zn alloys via controlled atomic ratio adjustments.[132, 214, 215]

The Ga–Al binary system forms a eutectic alloy with a melting point of 424°C at 47 wt% Al, significantly lower than pure Al (660.3°C), facilitating Al_2O_3 formation at the liquid metal surface.[216] By adjusting the Ga-to-Al ratio, Ga atoms can migrate to the surface, enabling the formation of $(Al_xGa_{1-x})_2O_3$ nanosheets with precisely controlled Al content. This method circumvents the challenges associated with high-temperature synthesis, providing an efficient route for bandgap engineering. Density functional theory (DFT) calculations predict that the monoclinic β-phase structure of $(Al_xGa_{1-x})_2O_3$ is stable and energetically favourable up to 71% Al incorporation,[14] while experimental studies reveal a strong bowing bandgap effect.[217, 218] Beyond composition control, point defects play a crucial role in the optical and electrical properties of $(Al_xGa_{1-x})_2O_3$ alloys. While defect and self-trapped hole (STH) states in Ga_2O_3 have been extensively studied, their impact in high-Al-content alloys remains largely unexplored. Understanding these Al-

mediated transitions is essential for engineering the electronic band structure for optoelectronic and power electronic applications.

In this work, we demonstrate the liquid metal-based synthesis of large-area β-$(Al_xGa_{1-x})_2O_3$ nanosheets with controlled Al incorporation. The structural, electronic and optical properties of these nanosheets are systematically investigated, with a focus on bandgap modulation and defect-related optical features. Our findings provide insights into the scalable synthesis of 2D wide bandgap oxide semiconductors.

5.3. Results and discussion

The $(Al_xGa_{1-x})_2O_3$ nanosheets were fabricated using a squeeze-printing technique, in which liquid Ga–Al alloys (0.01–10 at% Al) were prepared at 250 °C and compressed between two preheated Si/SiO_2 substrates under an inert atmosphere. This process enabled the controlled transfer of ultrathin oxide layers formed on the liquid metal surface. A nitrogen-filled glovebox with O_2 levels of 0.1–0.2% was used to regulate surface oxidation. (Full synthesis details are provided in Chapter 3.)

Optical microscopy confirms the uniform and continuous morphology of the harvested $(Al_xGa_{1-x})_2O_3$ nanosheet (Figure 5.1a), while AFM imaging reveals a nanosheet thickness of 3.2 ± 0.5 nm (Figure 5.1b). These findings demonstrate the efficiency and reproducibility of the squeeze printing technique for fabricating $(Al_xGa_{1-x})_2O_3$ nanosheets. Bright-field transmission electron microscopy (TEM) and selected area electron diffraction (SAED) were performed to analyze the harvested nanosheets deposited onto a lacy carbon grid (Figure 5.1c). The TEM image reveals the smooth, electron-transparent and uniform surface of $(Al_{0.71}Ga_{0.29})_2O_3$ nanosheets harvested from Ga_{99}-Al_1 liquid metal. The corresponding SAED pattern exhibits diffuse halos without distinct diffraction spots or sharp rings, indicating significant structural disorder in the nanosheet and absence of

long-range crystallinity. This observation is consistent with the Near Edge X-ray Absorption Fine Structure (NEXAFS) results discussed below. Energy-dispersive X-ray spectroscopy (EDS) elemental mapping of the Ga Lα, Al Kα and O Kα intensity, acquired using TEM at 200 kV, presented in Figures 5.1d, show a uniform distribution of Ga, Al, and O across the nanosheet, with a notably higher intensity of Al compared to Ga, confirming preferential Al incorporation in the harvested nanosheets. Figure 5.1e displays the Raman spectra of the harvested Ga_2O_3 and $(Al_{0.71}Ga_{0.29})_2O_3$ nanosheets, obtained from pure Ga and Ga_{99}-Al_1 liquid metals, respectively. Both nanosheets exhibit broad Raman peaks with characteristic A_g modes.[219] The $(Al_{0.71}Ga_{0.29})_2O_3$ nanosheet exhibit additional shoulders at ~ 330 and 450 cm^{-1}, attributed to Al-O vibrational modes,[220] indicating the coexistence of Al-O and Ga-O bonds in the lattice. A typical X-ray diffraction (XRD) pattern for the β-$(Al_{0.71}Ga_{0.29})_2O_3$ nanosheets is shown in Figure 5.1f. To enhance the XRD signal strength, three squeeze-printing cycles were performed. Diffraction peaks at 18.4°, 37.8° and 58.9° correspond to the (-201), (-402) and (-603) crystal planes of β-$(Al_{0.71}Ga_{0.29})_2O_3$, [221] confirm the crystalline nature of the nanosheet. Although their crystallinity is lower than that of MBE-grown β-$(Al_xGa_{1-x})_2O_3$ thin films on conventional sapphire substrates at high temperatures (> 800 ºC), as evidenced by the absence of SAED spots, the nanosheets retain a preferential (-201) orientation. The full width at half maximum (FWHM) of the (-402) peak (~ 0.55º) is much broader than in thin films, [222] likely due to incoherent scattering in the ultrathin nanosheets. The absence of the (-401) peak at ~ 30º, typically associated with random oriented β-Ga_2O_3, [223] and the lack of diffraction peaks from other phases indicate a strong preference for the β-(-201) orientation.

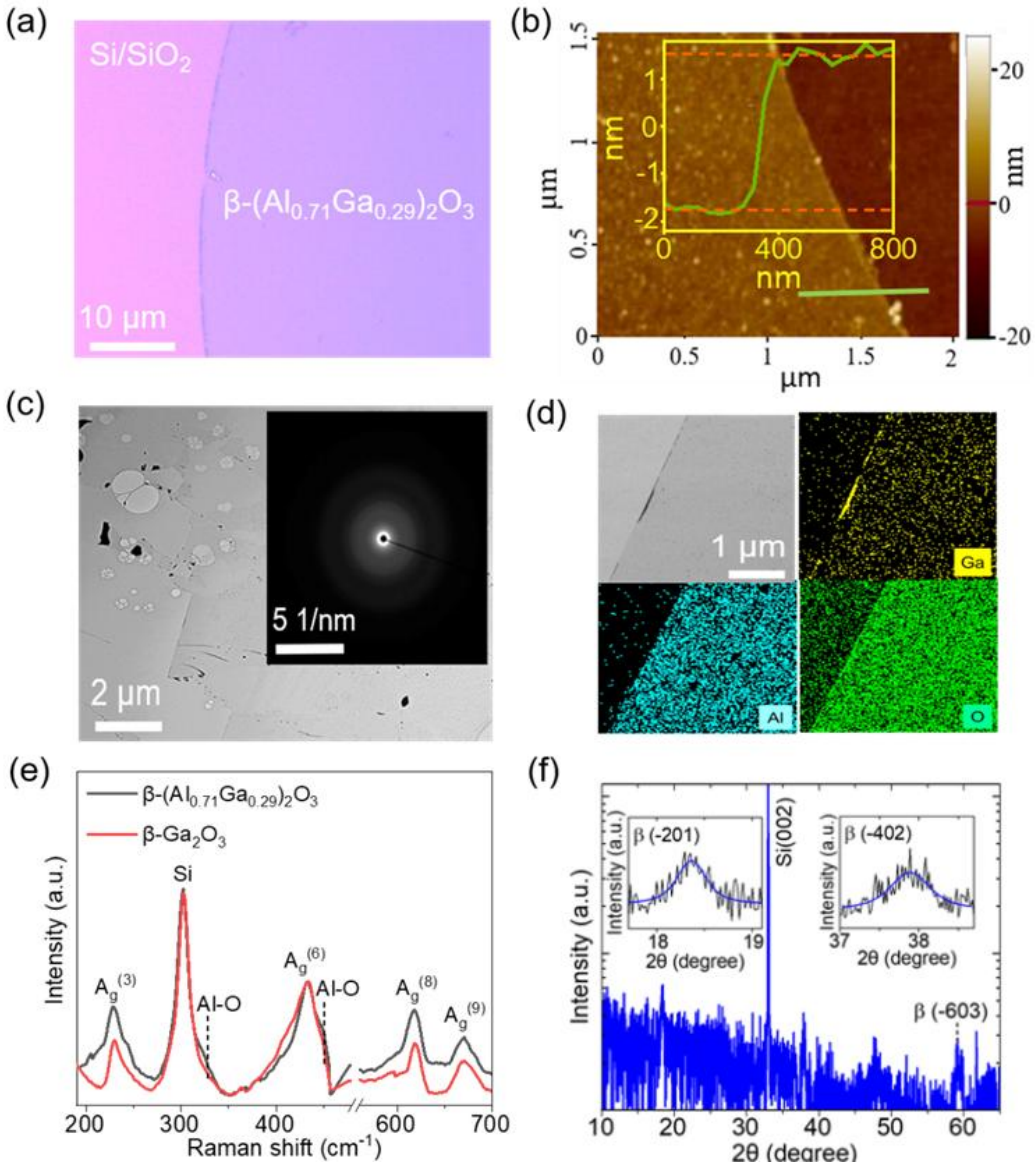

Figure 5.1. (a) Optical image of a single squeezed β-$(Al_{0.71}Ga_{0.29})_2O_3$ nanosheet from Ga_{99}-Al_1 droplets. (b) AFM image of the nanosheet, with the inset showing a height profile indicating a thickness of 3.2 ± 0.5 nm. (c) Bright-field TEM image and corresponding SAED pattern of the nanosheet. (d) TEM image and corresponding EDS elemental maps of Ga Lα, Al Kα and O Kα X-ray intensity. (e) Raman spectra of the β-Ga_2O_3 and β-$(Al_{0.71}Ga_{0.29})_2O_3$ nanosheets, harvested from pure Ga and Ga_{99}- Al_1 liquid metals, respectively. (f) XRD pattern plotted on a logarithmic intensity scale, showing a dominant Si (002) peak and weak β-phase diffraction peaks from the nanosheet, with enlarged views of the (-201) and (-402) reflections.

X-ray Photoelectron Spectroscopy (XPS) and Near Edge X-ray Absorption Fine Structure (NEXAFS) were performed to analyse the atomic composition and chemical states in the β-$(Al_xGa_{1-x})_2O_3$ nanosheets. Figures 5.2a-c present the XPS spectra of Ga 2*p*, Al 2*p* and O 1*s* for the nanosheets harvested from Ga_{99}-Al_1 liquid metal. The Ga $2p_{3/2}$ and Ga $2p_{1/2}$ peaks at 1118.8 and 1145.3 eV, respectively, confirm the Ga^{3+} oxidation state for β-$(Al_xGa_{1-x})_2O_3$ nanosheets.[224] The Al 2*p* spectrum exhibits doublet peaks at 74.0 eV and 74.3 eV, corresponding to Al_2O_3.[225, 226] The O 1*s* spectrum can be deconvoluted into two peaks at 532.3 eV and 530.7 eV, attributed to oxygen in the SiO_2 substrate and β-$(Al_xGa_{1-x})_2O_3$, respectively (Figure 5.2c).[153] Even when the Al content in the liquid alloy is increased to 10 at%, resulting in the formation of $(Al_{0.88}Ga_{0.12})_2O_3$ nanosheets, there is no significant change in the nanosheet thickness or in the Ga and Al chemical states, as shown in Figure 5.3. These XPS results, along with the analysis of NEXAFS data shown in Figure 5-4, indicate that Al and Ga predominantly exist as Al^{3+} and Ga^{3+}, respectively, with no detection of metallic phases, and that the nanosheets possess a disordered monoclinic structure without traces of α-Al_2O_3.

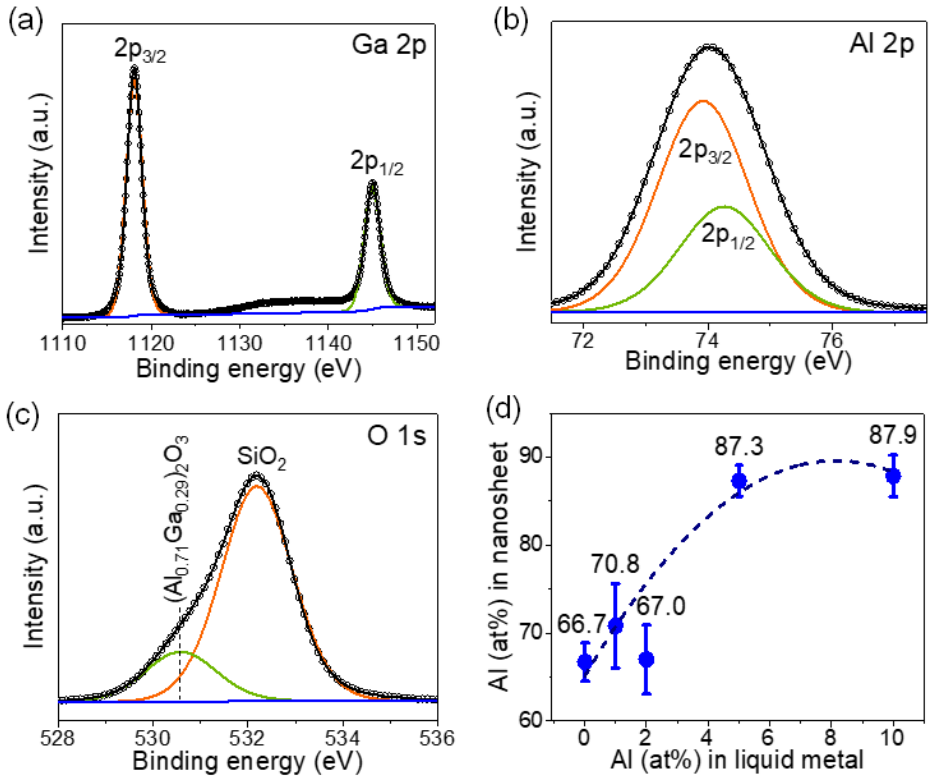

Figure 5.2. (a-c) XPS spectra of Ga 2p, Al 2p, and O 1s in the $(Al_{0.71}Ga_{0.29})_2O_3$ nanosheet harvested from Ga_{99}-Al_1 liquid metal. (d) Variation of Al concentration in the nanosheet as a function of Al content in the Ga-Al droplet. Error bars represent the standard deviation from a minimum of five measurements.

XPS analysis reveals strong Al enrichment in the nanosheets compared with the bulk liquid metal, as shown in Figure 5.2d and Table 5.1. Even a trace amount of 0.01 at% Al in $Ga_{99.99}$-$Al_{0.01}$ liquid metal results in 67 at% Al, corresponding to the composition of $(Al_{0.67}Ga_{0.33})_2O_3$. Increasing the Al concentration from 0.1 to 5 at% in the liquid metal leads to a steady rise of Al content in the nanosheets, reaching a plateau at ~87% for Ga_{95}-Al_5 liquid metal. Beyond this threshold, additional Al in the liquid metal does not further increase Al incorporation in the oxide nanosheet, suggesting a thermodynamic limit to Al enrichment in the interfacial layer. This enrichment pattern indicates that despite its lower atomic fraction in the liquid metal, Al preferentially

concentrates in the interfacial oxide due to its greater thermodynamic stability (ΔG_f reduction), along with solubility and temperature effects.[227] Similar behavior has been observed in other liquid-metal-derived 2D materials. For example, Bi_2O_3-doped SnO nanosheets exhibit higher Sn concentrations in the interfacial oxide than in the bulk Bi-Sn alloy,[132] while TeO_2 dominates the oxide layer in a 5 wt% Te–95 wt% Se eutectic mixture due to greater exophilicity of Te.[228]

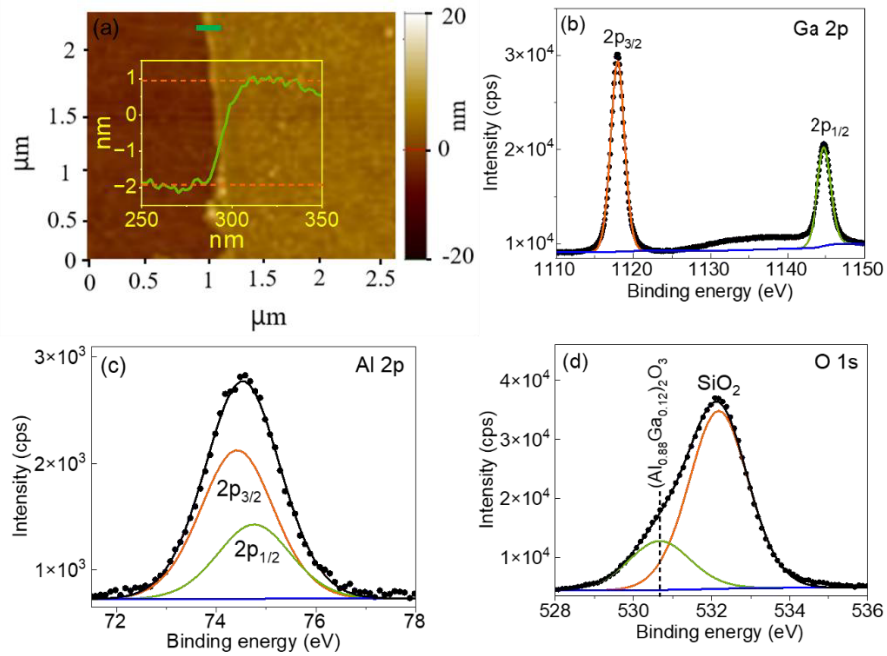

Figure 5.3. (a) AFM image of a $(Al_{0.88}Ga_{0.12})_2O_3$ nanosheet harvested from Ga_{90}-Al_{10} liquid metal. The inset shows a height profile indicating a thickness of 3.0 ± 0.4 nm. (b-d) XPS spectra of Ga 2*p*, Al 2*p*, and O 1*s* in the nanosheet. Comparing with the images and spectra of the nanosheets with lower Al content shown in Figures 1 and 3, no significant variation in nanosheet thickness or changes in the Ga and Al chemical states are observed in the $(Al_{0.88}Ga_{0.12})_2O_3$ nanosheet.

Table 5.1. Composition of Ga-Al liquid alloys and the corresponding Ga and Al atomic percentages in the harvested oxide nanosheets as determined by XPS analysis. Standard deviations are based on five measurements.

Alloy composition	**Oxide Nanosheet**		**Oxide Nanosheet**
	Ga (at%)	**Al (at%)**	
$Ga_{99.99}$-$Al_{0.01}$	33.3 ± 5.1	66.7 ± 5.3	$(Al_{0.67}Ga_{0.33})_2O_3$
Ga_{99}-Al_1	29.2 ± 2.0	70.8 ± 2.1	$(Al_{0.71}Ga_{0.29})_2O_3$
Ga_{98}-Al_2	33.0 ± 5.6	67.0 ± 6.1	$(Al_{0.67}Ga_{0.33})_2O_3$
Ga_{95}-Al_5	12.7 ± 4.1	87.3 ± 4.5	$(Al_{0.87}Ga_{0.13})_2O_3$
Ga_{90}-Al_{10}	12.3 ± 1.0	87.7 ± 1.1	$(Al_{0.88}Ga_{0.12})_2O_3$

Figures 5.4a-c present the NEXAFS spectra of Ga L_3-edge, O K-edge and Al K-edge collected in TEY mode for the harvested β-$(Al_{0.71}Ga_{0.29})_2O_3$ nanosheets, together with β-Ga_2O_3 and α-Al_2O_3 reference films for comparison. The Ga L_3-edge NEXAFS spectra exhibit resonant features corresponding to electronic transitions from the Ga $2p_{3/2}$ core level to unoccupied Ga-derived states. In the β-Ga_2O_3 reference film, three well-defined peaks are observed at ~1119.7 eV (Ga_1), 1121.9 eV (Ga_2) and 1124.0 eV (Ga_3), corresponding to transitions into Ga 4s, 3d, and 4p states hybridized with oxygen orbitals. [193] The β-$(Al_{0.71}Ga_{0.29})_2O_3$ nanosheets exhibit a more pronounced Ga_1 peak, while Ga_2 and Ga_3 merge into a broad peak, indicating significant structural disorder, likely due to Al incorporation into the 2D lattice. The O K-edge NEXAFS spectra show similar absorption features for both the β-$(Al_{0.71}Ga_{0.29})_2O_3$ nanosheets and reference β-Ga_2O_3. The peak at 535.3 eV (O_1) corresponds to hybridization of O 2p states with Ga 4s and 4p orbitals, while peaks between 537.7 eV and 540.8 eV (O_2 and O_3) arise from interactions with Ga and Al orbitals. [229, 230] Compared with β-Ga_2O_3, peaks O_1 and O_3 in β-$(Al_{0.71}Ga_{0.29})_2O_3$ nanosheets are significantly broader, due to the presence of both Ga-O and Al-O bonds. The Al K-edge NEXAFS spectra of β-$(Al_{0.71}Ga_{0.29})_2O_3$ nanosheets and α-Al_2O_3 provide insights into the coordination of Al atoms The spectrum of α-Al_2O_3 exhibits two main peaks at 1566.3 eV (Al_1) and 1571.3 eV (Al_2), corresponding to Al 1s

→ 3p transitions. [231, 232] Notably, the α-Al_2O_3 pre-edge at ~ 1556 eV is absent in the β-$(Al_{0.71}Ga_{0.29})_2O_3$ spectrum, [233] which confirms the nanosheets do not contain any detectable α-Al_2O_3 phase. The XPS results, along with the analysis of NEXAFS data confirm that Al and Ga predominantly exist as Al^{3+} and Ga^{2+}, respectively, with no detection of unalloyed metallic phases, and that the nanosheets possess a monoclinic structure without traces of α-Al_2O_3.

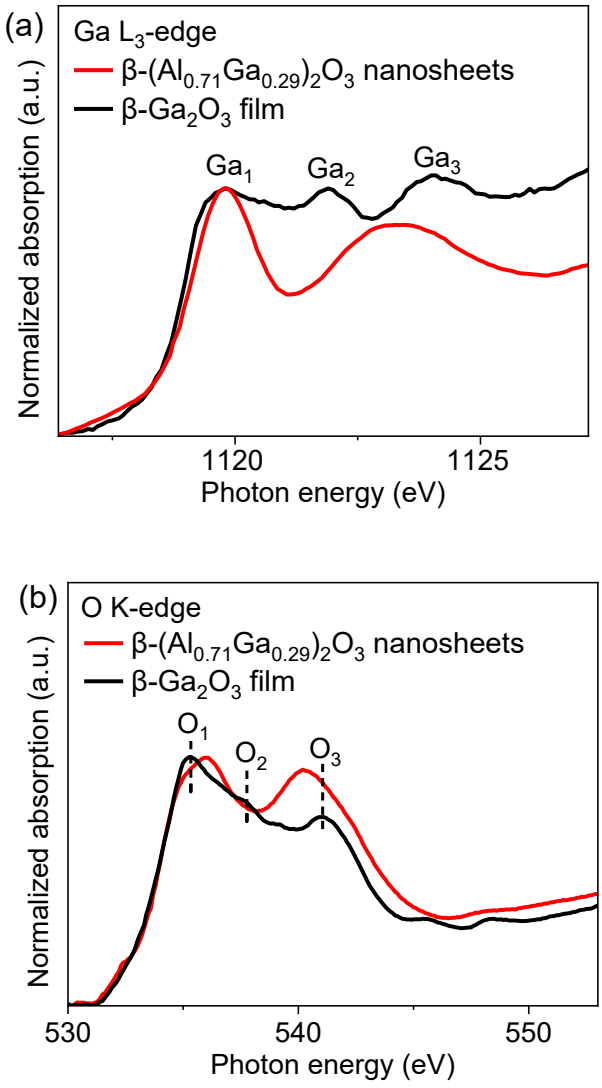

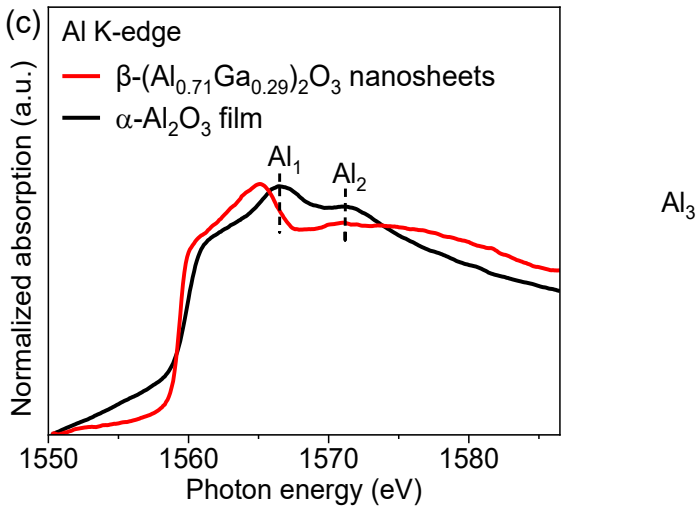

Figure 5.4. NEXAFS spectra of (a) Ga L_3-edge, (b) O K-edge and (c) Al K-edge collected in the total electron yield (TEY) mode for the harvested β-$(Al_{0.71}Ga_{0.29})_2O_3$ nanosheets, shown alongside β-Ga_2O_3 and α-Al_2O_3 reference films for comparison.

Electron energy loss spectroscopy (EELS) was used to estimate the electronic bandgap (E_g) of oxide nanosheets harvested from liquid alloys with Al concentrations ranging from 0 to 10 at% (Figure 5.5a). E_g was determined by extrapolating linear fits to the intensity rise relative the background. For β-Ga_2O_3 nanosheets, E_g = 4.5 eV, slightly lower than the bulk value of 4.8 eV. As shown in the inset of Figure 5.5a, the bandgap of the β-$(Al_xGa_{1-x})_2O_3$ nanosheets increases with Al concentration, in agreement with theoretical predictions.[14] However, an anomalously low bandgap of 5.20 eV is observed for β-$(Al_{0.67}Ga_{0.33})_2O_3$) nanosheets obtained from Ga_{98}-Al_2 liquid alloy, followed by a monotomic increase to 6.41 eV for β-$(Al_{0.88}Ga_{0.12})_2O_3$ nanosheets obtained from Ga_{90}-Al_{10}. This trend is consistent with β-$(Al_xGa_{1-x})_2O_3$ thin films grown by MOCVD, which exhibit bandgap widening up to 6.1 eV at x = 0.84 due to the redistribution of Ga *d* states.[234, 235] The greater bandgap widening in the β-$(Al_xGa_{1-x})_2O_3$ nanosheets is likely due to quantum confinement effects.[236] The work function (ϕ) of the oxide nanosheets is extracted by applying a linear fit to the secondary electron cut-off in ultraviolet

photoelectron spectroscopy (UPS) spectra (Figure 5.5b),[237] yielding 3.03 eV for β-Ga_2O_3 nanosheets. As shown in the inset of Figure 5.5b, ϕ gradually increases to 3.29 eV for β-$(Al_{0.67}Ga_{0.33})_2O_3$ nanosheets (harvested from Ga_{98}-Al_2 liquid alloy) but decreases with further Al incorporation in the nanosheet. Figure 5.5c and its inset illustrate the valence band maximum (VBM) values, extracted from the valence band onset. The VBM for β-Ga_2O_3 nanosheets is 6.20 eV below the vacuum level and gradually increases to 6.90 eV as the Al fraction rises from 0.67 to 0.88 in β-$(Al_xGa_{1-x})_2O_3$ nanosheets. The electronic band structures of β-$(Al_xGa_{1-x})_2O_3$ nanosheets extracted from Al-Ga liquid alloys are shown in Figure 5.5d, with corresponding data presented in Table 5.2.

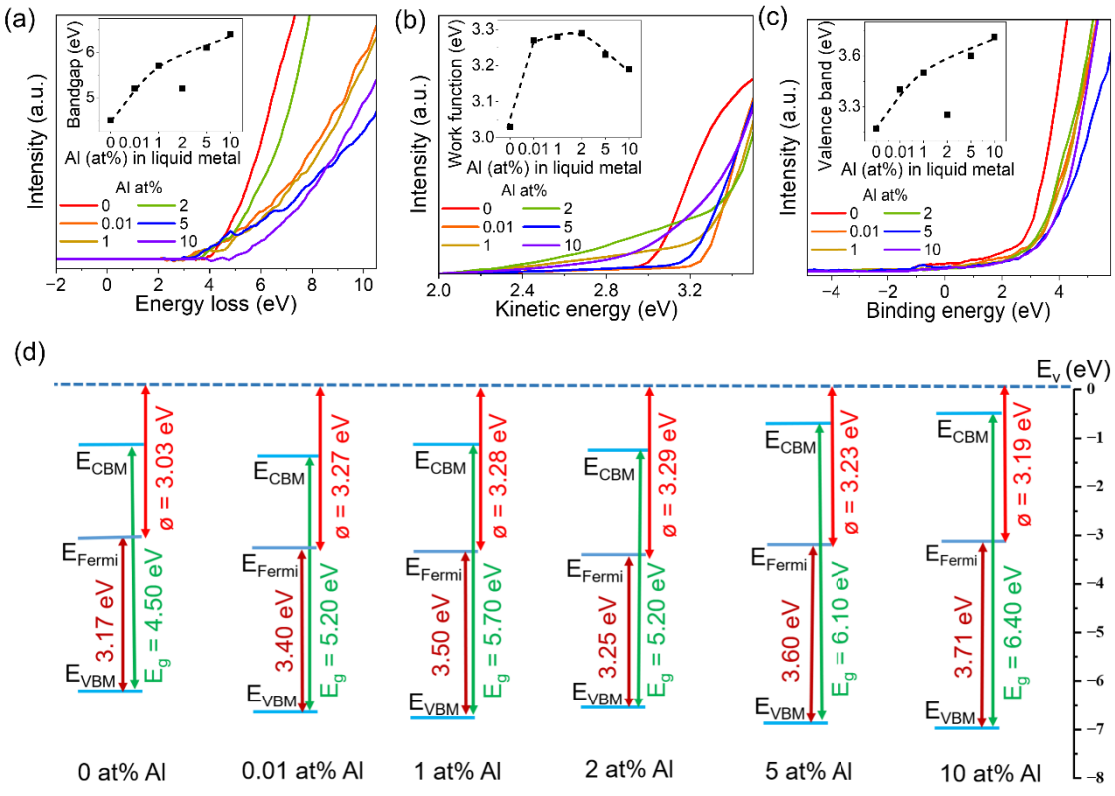

Figure 5.5. (a) EELS spectra of β-$(Al_xGa_{1-x})_2O_3$ nanosheets, with the inset showing their bandgap as a function of Al concentration in the nanosheets. (b) UPS spectra, with the inset illustrating the work function. (c) Valence band spectra, with the inset demonstrating a monotonic shift in valence band onset with increasing Al concentration. (d) Electronic band structures of β-$(Al_xGa_{1-x})_2O_3$ nanosheets derived from the EELS, XPS and UPS results.

Table 5.2. Electronic structure parameters of β-Ga_2O_3 and β-$(Al_xGa_{1-x})_2O_3$ nanosheets harvested from Ga-Al liquid metals with Al concentrations ranging from 0 to 10 at%. The valence band maximum (VBM) and conduction band minimum (CBM) energies are referenced to the vacuum level (zero energy). These values are determined using EELS, UPS secondary electron cut-off and XPS valence band analysis.

Oxide nanosheet	**Bandgap (E_g) (eV)**	**Work function (ϕ) (eV)**	**Valence band maximum (VBM) (eV)**	**Conduction band minimum (CBM) (eV)**
β-Ga_2O_3	4.50	3.03	-6.20	-1.70
β-($Al_{0.67}Ga_{0.33}$)$_2O_3$	5.20	3.27	-6.67	-1.47
β-($Al_{0.71}Ga_{0.29}$)$_2O_3$	5.71	3.28	-6.78	-1.07
β-($Al_{0.67}Ga_{0.33}$)$_2O_3$	5.20	3.29	-6.54	-1.34
β-($Al_{0.87}Ga_{0.13}$)$_2O_3$	6.12	3.23	-6.83	-0.71
β-($Al_{0.88}Ga_{0.12}$)$_2O_3$	6.41	3.19	-6.90	-0.49

Temperature-resolved cathodoluminescence (CL) spectra of β-$(Al_xGa_{1-x})_2O_3$ nanosheets reveal the effect of Al incorporation on their optical properties (Figures 5.6a, b). Below 160 K, the spectra are dominated by emissions from STHs, which are quenched rapidly with increasing temperature due to their thermal instability.[210] These spectra exhibit broad, overlapping emission peaks arising from strong electron-phonon coupling, leading overlapped emissions from STHs and defects. As shown in Figure 5.6c, the CL spectrum of pure β-Ga_2O_3 nanosheets displays predominantly STH-associated UV emission, together with week defect-related green luminescence (GL) and blue luminescence (BL) bands. In contrast, the β-$(Al_{0.71}Ga_{0.29})_2O_3$ nanosheets in Figure 5.6d

show significant changes in emission profile: the GL band is strongly enhanced and the overall emission shifts toward the deep ultraviolet (DUV) region, indicating a widened bandgap and altered defect structure. To elucidate the underlying emission mechanisms, Gaussian peak fitting is applied for spectral deconvolution.[196, 238] For β-Ga_2O_3 nanosheets, the CL spectrum (Figure 5.6c) is deconvoluted into three peaks: a broad UV emission at 3.20 eV (FWHM = 0.75 eV), blue luminescence (BL) at 2.58 eV (FWHM = 0.95 eV) and green luminescence (GL) at 2.10 eV (FWHM = 0.98 eV). The UV peak originates from holes trapped in lattice-coupled polaron states, which relax radiatively, yielding a Gaussian-like band.[210]

The BL and GL peaks are attributed to donor-acceptor pairs (DAP) recombination, likely involving V_O donors, V_{Ga} acceptors and (V_O-V_{Ga}) complexes.[238, 239] For β-$(Al_{0.71}Ga_{0.29})_2O_3$ nanosheets, the CL spectrum (Figure 5.6d) similarly features UV (3.20 eV, FWHM = 0.78 eV), BL (2.60 eV, FWHM = 0.90 eV), and GL (2.10 eV, FWHM = 1.0 eV) peaks. Notably, a deep ultraviolet (DUV) peak emerges at 3.80 eV (FWHM = 0.9 eV). The two UV bands in β-$(Al_{0.71}Ga_{0.29})_2O_3$ are attributed to the radiative recombination from distinct STH states,[240, 241] with the emerged DUV peak is attributed to radiative recombination of an STH localized at an oxygen site adjacent to an Al atom, analogous to dopant-induced hole trapping states in β-Ga_2O_3.[31] The two STH states are separated by 0.6 eV as estimated from the spectral deconvolution. The DUV band exhibits thermal quenching behavior similar to the UV band, becoming nearly undetectable above 200 K. This indicates that Al incorporation into oxide nanosheets introduces a new recombination pathway, extending the emission into the DUV region. As shown in Fig 5.6(c, d) both the BL and GL intensities are higher in β-$(Al_{0.71}Ga_{0.29})_2O_3$ compared with β-Ga_2O_3 nanosheets, suggesting an increased density of V_O defects. Comparison of the CL spectra for β-Ga_2O_3 and β-$(Al_{0.71}Ga_{0.29})_2O_3$ nanosheets (Figure 5.6e) reveals a ~ 60%

reduction in emission intensity, likely due to the lower crystallinity of the alloy oxide nanosheets and random potential fluctuations inherent in the alloy.[242]

Arrhenius analysis (Figures 5.6f) yields activation energies (E_a). The extracted activation energies for β-$(Al_{0.71}Ga_{0.29})_2O_3$ are 2.4 meV (GL), 3.5 meV (BL), 10.9 meV (UV) and 8.1 meV (DUV). These relatively small activation energies indicate weak temperature dependence, likely due to thermal quenching via phonon-assisted excitation of localized states.[238] The higher E_a values for the UV and DUV bands indicate that the STH formation in the nanosheets is highly sensitive to temperature. These findings highlight the potential of β-$(Al_xGa_{1-x})_2O_3$ nanosheets for deep-UV photodetectors as well as optical and power electronic devices, where tunable electronic band structures and defect engineering are critical for performance optimization.

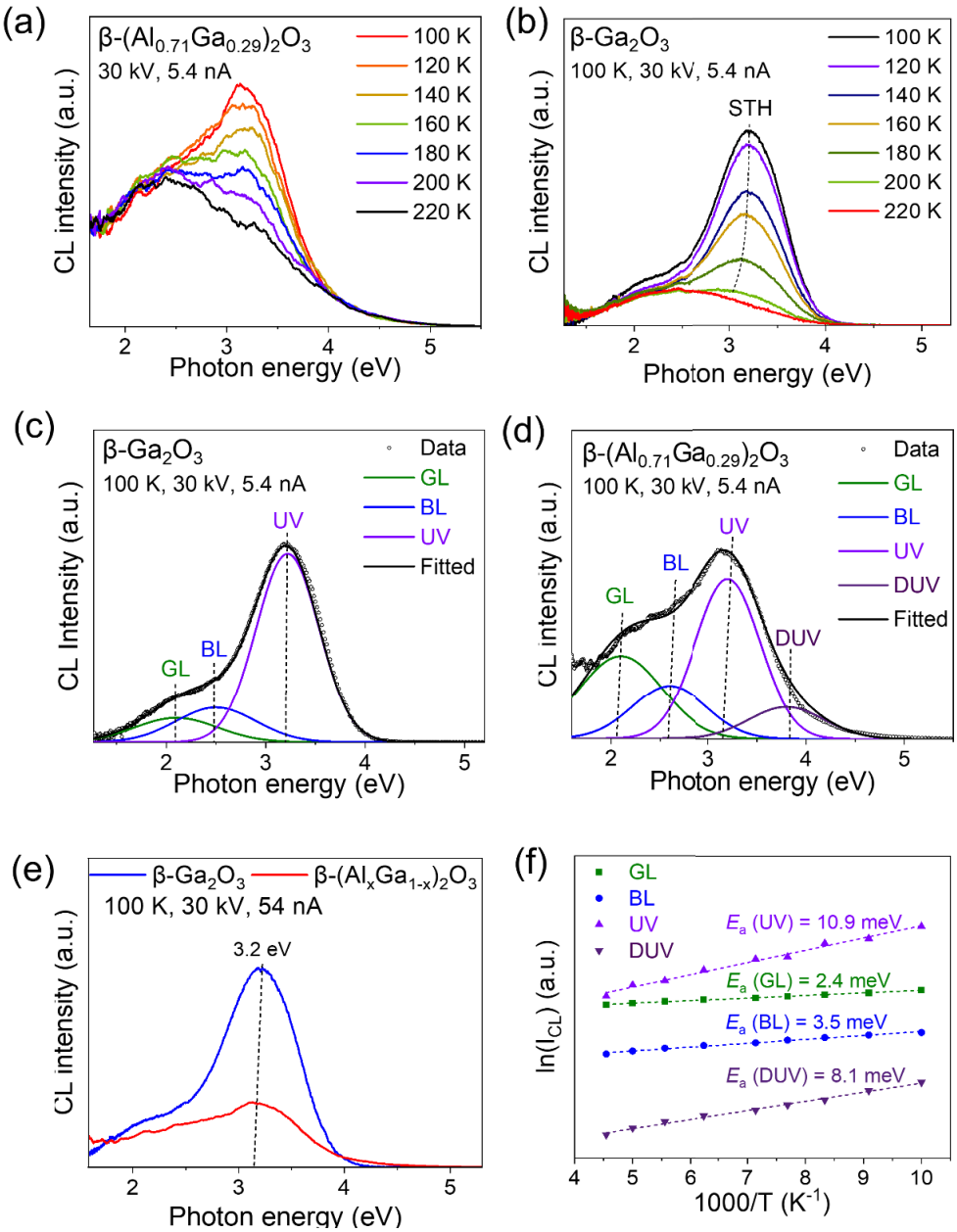

Figure 5.6. (a, b) Temperature-resolved CL spectra of the β-$(Al_{0.71}Ga_{0.29})_2O_3$ and β-Ga_2O_3 nanosheets. (c) CL spectrum of β-Ga_2O_3, deconvoluted into three Gaussian peaks centred at 2.10 eV (GL), 2.58 eV (BL), and 3.20 eV (UV). (d) CL spectrum of β-$(Al_{0.71}Ga_{0.29})_2O_3$, resolved into four components GL, BL and UV, alongside a new DUV at 3.80 eV. (e) CL spectra of harvested β-Ga_2O_3 and β- $(Al_{0.71}Ga_{0.29})_2O_3$ nanosheets acquired at 100 K. (f) Arrhenius analysis of the emission bands, resulting in the thermal activation energies (E_a) indicated in the graph.

5.3. Conclusion

We demonstrated a liquid metal-based synthesis method for β-$(Al_xGa_{1-x})_2O_3$ nanosheets with controlled composition and the (-201) orientation, consistent with thin films fabricated by epitaxial growth. This approach enables bandgap engineering, achieving values from 4.50 eV (pure β-Ga_2O_3) to 6.41 eV (β-$(Al_{0.88}Ga_{0.12})_2O_3$) by varying Al incorporation in the Al-Ga liquid alloy. The nanosheets exhibit nano-crystallinity, large lateral dimensions (> 100 μm) and atomic-scale thickness, making them suitable for optoelectronic and power device applications. The β-$(Al_xGa_{1-x})_2O_3$ nanosheets exhibit robust broadband luminescence, with Al incorporation introducing a distinct deep-UV emission while preserving the dominant β-Ga_2O_3 UV emission associated with self-trapped holes. The ability to synthesize β-$(Al_xGa_{1-x})_2O_3$ nanosheets with tuneable electronic structures via a scalable, low-temperature process offers significant advantages over conventional deposition techniques. These findings open new avenues for the development of next-generation wide-bandgap semiconductors for deep-UV detection and power electronics.

Chapter 6. Conclusions and Outlook

6.1. Summary

This thesis investigated the synthesis and characterization of $ZnGa_2O_4$ nanoplates and β-$(Al_xGa_{1-x})_2O_3$ nanosheets, focusing on their optical and electronic properties. Specifically, it examines how cation site inversion influences the optical and photocatalytic properties of $ZnGa_2O_4$ and how Al incorporation enables bandgap engineering in β-$(Al_xGa_{1-x})_2O_3$.

The first part of this study explored the role of cation site inversion in tuning the properties of $ZnGa_2O_4$ nanoplates, a promising wide-bandgap material for light-emitting and power electronic devices. High-quality, pure spinel-phase $ZnGa_2O_4$ nanoplates were successfully synthesized via a hydrothermal method and exhibited significant anti-site defects**,** where Ga^{3+} ions occupy tetrahedral sites (Ga_{Zn}) and Zn^{2+} ions occupy octahedral sites (Zn_{Ga}). These inversion defects were confirmed by photoemission and Raman spectroscopies, with measured cation inversion parameters of 0.36 ± 0.04 for Ga_{Zn} and 0.25 ± 0.02 for Zn_{Ga}. The nanoplates demonstrated broadband luminescence**,** with a UV emission band at 3.2 eV (associated with self-trapped holes) and multiple visible defect-related emissions. Furthermore, $ZnGa_2O_4$ nanoplates exhibited superior photocatalytic efficiency in degrading Rhodamine B (RhB) under UVA irradiation, outperforming Ga_2O_3 counterparts. This enhancement is attributed to the increased UVA absorption and charge carrier generation induced by inversion defects. These results underscore the significance of cation site inversion in modifying the optical and photocatalytic properties of $ZnGa_2O_4$ nanoplates**,** making it highly suitable for optoelectronic and photocatalytic applications.

The second part of this thesis focused on the synthesis and characterization of β-$(Al_xGa_{1-x})_2O_3$ nanosheets using a low-temperature, liquid metal-based synthesis technique. This method provided precise control over the Al content, enabling bandgap modulation from 4.5 eV (pure β-Ga_2O_3) to 6.4 eV (β-$(Al_{0.88}Ga_{0.12})_2O_3$) by varying the Al concentration in the liquid metal alloy. The Al-enriched nanosheets exhibited distinct optical properties, retaining the self-trapped hole emission of β-Ga_2O_3 around 3.2 eV, while an additional deep-UV emission emerged, which is attributed to singly ionized oxygen vacancies localized at Al–O sites. These findings highlight the effectiveness of selective Al incorporation in tailoring the electronic and optical properties of 2D metal oxide nanosheets**,** paving the way for their application in next-generation optoelectronic devices with tuneable bandgaps.

While this thesis investigated two distinct oxide systems, a unifying principle emerges: controlling defects at the atomic level is essential for tuning the properties of wide-bandgap materials. In $ZnGa_2O_4$, cation site inversion changed how the material emits light and performs in photocatalysis. In β-$(Al_xGa_{1-x})_2O_3$, changing the amount of aluminium adjusted the bandgap and luminescence. The two synthesis methods used—hydrothermal growth and liquid metal-based exfoliation—provided practical ways to create and study these materials. Together, these results offer important insights for designing new oxide semiconductors for use in electronics, light-based technologies, and energy devices.

In summary, this thesis demonstrates how intrinsic cation site inversion in $ZnGa_2O_4$ nanoplates contributes not only to their broadband luminescence but also significantly enhances their photocatalytic activity, outperforming β-Ga_2O_3 in the degradation of RhB under UVA irradiation. These findings emphasize the critical role of

Ga_{Zn} anti-site defects, which introduce shallow electronic states that mediate optical transitions. Additionally, the liquid metal synthesis approach developed here enables precise Al incorporation into β-$(Al_xGa_{1-x})_2O_3$ nanosheets, offering a practical method for bandgap engineering. This strategy introduces distinct deep-UV emission while preserving the self-trapped hole emission of β-Ga_2O_3, paving the way for the design of next-generation optoelectronic materials with tuneable properties.

6.2. Outlook

Building upon the findings of this thesis, several aspects warrant further investigation to deepen the understanding of $ZnGa_2O_4$ nanoplates and β-$(Al_xGa_{1-x})_2O_3$ nanosheets. One important direction is to explore the influence of synthesis conditions, particularly the effect of pH and the initial Zn/Ga ratio, on the formation of anti-site defects in $ZnGa_2O_4$. A systematic study of these parameters could provide insights into defect control and their impact on optical and photocatalytic properties.

For β-$(Al_xGa_{1-x})_2O_3$ nanosheets, further research is needed to understand the effects of high Al concentrations on emission properties, particularly in the green and blue spectral regions, which are relevant to for optoelectronic applications. Additionally, since breakdown field strength is a critical parameter for power electronic devices, future work should investigate not only the breakdown characteristics but also the semiconducting behavior and carrier mobility of β-$(Al_xGa_{1-x})_2O_3$ nanosheets. These properties are essential for evaluating their true suitability for integration into high-power electronic applications. These future studies will contribute to a more comprehensive understanding of defect chemistry and bandgap engineering in these materials, enhancing their potential for next-generation electronic and optoelectronic devices.

References:

(1) Chae, S.; Mengle, K.; Bushick, K.; Lee, J.; Sanders, N.; Deng, Z.; Mi, Z.; Poudeu, P. F.; Paik, H.; Heron, J. T. Toward the predictive discovery of ambipolarly dopable ultra-wide-band-gap semiconductors: The case of rutile GeO_2. *Applied Physics Letters* **2021**, *118* (26).

(2) Seo, J.-H. *Wide bandgap semiconductor based micro/nano devices*; MDPI, 2019.

(3) Pearton, S. J.; Yang, J.; Cary, P. H.; Ren, F.; Kim, J.; Tadjer, M. J.; Mastro, M. A. A review of Ga_2O_3 materials, processing, and devices. *Applied Physics Reviews* **2018**, *5* (1), 011301.

(4) Rafique, S.; Han, L.; Tadjer, M. J.; Freitas, J. A.; Mahadik, N. A.; Zhao, H. Homoepitaxial growth of β-Ga_2O_3 thin films by low pressure chemical vapor deposition. *Applied Physics Letters* **2016**, *108* (18), 182105.

(5) Kyrtsos, A.; Matsubara, M.; Bellotti, E. On the feasibility of p-type Ga_2O_3. *Applied Physics Letters* **2018**, *112* (3), 032108.

(6) Tadjer, M. J.; Lyons, J. L.; Nepal, N.; Freitas, J. A.; Koehler, A. D.; Foster, G. M. Review—Theory and characterization of doping and defects in β-Ga_2O_3. *ECS Journal of Solid State Science and Technology* **2019**, *8* (7), Q3187-Q3194.

(7) Zhang, J.; Shi, J.; Qi, D.-C.; Chen, L.; Zhang, K. H. Recent progress on the electronic structure, defect, and doping properties of Ga_2O_3. *APL Materials* **2020**, *8* (2), 020906.

(8) Chi, Z.; Tarntair, F.-G.; Frégnaux, M.; Wu, W.-Y.; Sartel, C.; Madaci, I.; Chapon, P.; Sallet, V.; Dumont, Y.; Pérez-Tomás, A. Bipolar self-doping in ultra-wide bandgap spinel $ZnGa_2O_4$. *Materials Today Physics* **2021**, *20*, 100466.

(9) Chikoidze, E.; Sartel, C.; Madaci, I.; Mohamed, H.; Vilar, C.; Ballesteros, B.; Belarre, F.; Del Corro, E.; Vales-Castro, P.; Sauthier, G. p-type ultrawide-band-gap spinel $ZnGa_2O_4$: New perspectives for energy electronics. *Crystal Growth & Design* **2020**, *20* (4), 2535-2546.

(10) Frodason, Y. K.; Galeckas, A.; Olsen, V. S.; Weiser, P. M.; Galazka, Z.; Van de Walle, C. G.; Vines, L. Intrinsic origins of broad luminescence in melt-grown $ZnGa_2O_4$ single crystals. *Physical Review Materials* **2024**, *8* (9), 094604.

(11) Seko, A.; Oba, F.; Tanaka, I. Classification of spinel structures based on first-principles cluster expansion analysis. *Physical Review B—Condensed Matter and Materials Physics* **2010**, *81* (5), 054114.

(12) Guo, D.; Guo, Q.; Chen, Z.; Wu, Z.; Li, P.; Tang, W. Review of Ga2O3-based optoelectronic devices. *Materials Today Physics* **2019**, *11*, 100157.

(13) Zhang, F.; Saito, K.; Tanaka, T.; Nishio, M.; Arita, M.; Guo, Q. Wide bandgap engineering of $(AlGa)_2O_3$ films. *Applied Physics Letters* **2014**, *105* (16).

(14) Peelaers, H.; Varley, J. B.; Speck, J. S.; Van de Walle, C. G. Structural and electronic properties of Ga_2O_3-Al_2O_3 alloys. *Applied Physics Letters* **2018**, *112* (24).

(15) Bhuiyan, A. A. U.; Feng, Z.; Johnson, J. M.; Huang, H.-L.; Hwang, J.; Zhao, H. MOCVD growth of β-phase (Al. **2020**.

(16) Oshima, T.; Okuno, T.; Arai, N.; Kobayashi, Y.; Fujita, S. β-Al2xGa2-2xO3 thin film growth by molecular beam epitaxy. *Japanese Journal of Applied Physics* **2009**, *48* (7R), 070202.

(17) Anhar Uddin Bhuiyan, A.; Feng, Z.; Johnson, J. M.; Huang, H.-L.; Hwang, J.; Zhao, H. MOCVD epitaxy of ultrawide bandgap β-$(Al_xGa_{1-x})_2O_3$ with high-Al composition on (100) β-Ga_2O_3 substrates. *Crystal Growth & Design* **2020**, *20* (10), 6722-6730.

(18) Zavabeti, A.; Ou, J. Z.; Carey, B. J.; Syed, N.; Orrell-Trigg, R.; Mayes, E. L.; Xu, C.; Kavehei, O.; O'Mullane, A. P.; Kaner, R. B. A liquid metal reaction environment for

the room-temperature synthesis of atomically thin metal oxides. *Science* **2017**, *358* (6361), 332-335.
(19) Pearton, S. J.; Yang, J. I. Cary Patrick H., F. Ren, J. Kim, MJ Tadjer, M. A. Mastro. *Applied Physics Reviews* **2018**, *5*, 011301.
(20) Higashiwaki, M.; Jessen, G. H. Guest Editorial: The dawn of gallium oxide microelectronics. *Applied Physics Letters* **2018**, *112* (6), 060401
(21) Galazka, Z. β-Ga_2O_3 for wide-bandgap electronics and optoelectronics. *Semiconductor Science and Technology* **2018**, *33* (11), 113001.
(22) Higashiwaki, M.; Murakami, H.; Kumagai, Y.; Kuramata, A. Current status of Ga_2O_3 power devices. *Japanese Journal of Applied Physics* **2016**, *55* (12), 1202A1201.
(23) Mastro, M. A.; Kuramata, A.; Calkins, J.; Kim, J.; Ren, F.; Pearton, S. J. Perspective—opportunities and future directions for Ga_2O_3. *ECS Journal of Solid State Science and Technology* **2017**, *6* (5), P356.
(24) Peelaers, H.; Van de Walle, C. G. Doping of Ga_2O_3 with transition metals. *Physical Review B* **2016**, *94* (19), 195203.
(25) Mengle, K. A.; Shi, G.; Bayerl, D.; Kioupakis, E. First-principles calculations of the near-edge optical properties of β-Ga_2O_3. *Applied Physics Letters* **2016**, *109* (21).
(26) Onuma, T.; Saito, S.; Sasaki, K.; Masui, T.; Yamaguchi, T.; Honda, T.; Higashiwaki, M. Valence band ordering in β-Ga_2O_3 studied by polarized transmittance and reflectance spectroscopy. *Japanese Journal of Applied Physics* **2015**, *54* (11), 112601.
(27) Huynh, T. T.; Lem, L. L. C.; Kuramata, A.; Phillips, M. R.; Ton-That, C. Kinetics of charge carrier recombination in β-Ga_2O_3 crystals. *Physical Review Materials* **2018**, *2* (10), 105203.
(28) Onuma, T.; Fujioka, S.; Yamaguchi, T.; Higashiwaki, M.; Sasaki, K.; Masui, T.; Honda, T. Correlation between blue luminescence intensity and resistivity in β-Ga_2O_3 single crystals. *Applied Physics Letters* **2013**, *103* (4), 041910.
(29) Harwig, T.; Kellendonk, F. Some observations on the photoluminescence of doped β-galliumsesquioxide. *Journal of Solid State Chemistry* **1978**, *24* (3-4), 255-263.
(30) Binet, L.; Gourier, D. Origin of the blue luminescence of β-Ga_2O_3. *Journal of Physics and Chemistry of Solids* **1998**, *59* (8), 1241-1249.
(31) Gake, T.; Kumagai, Y.; Oba, F. First-principles study of self-trapped holes and acceptor impurities in Ga_2O_3 polymorphs. *Physical Review Materials* **2019**, *3* (4), 044603.
(32) Lany, S.; Zunger, A. Polaronic hole localization and multiple hole binding of acceptors in oxide wide-gap semiconductors. *Physical Review B—Condensed Matter and Materials Physics* **2009**, *80* (8), 085202.
(33) He, F.; Qin, Y.; Wang, Y.; Lin, Z.; Su, J.; Zhang, J.; Chang, J.; Hao, Y. Aqueous solution derived amorphous indium doped gallium oxide thin-film transistors. *IEEE Journal of the Electron Devices Society* **2021**, *9*, 373-377.
(34) Varley, J. B.; Janotti, A.; Franchini, C.; Van de Walle, C. G. Role of self-trapping in luminescence and p-type conductivity of wide-band-gap oxides. *Physical Review B—Condensed Matter and Materials Physics* **2012**, *85* (8), 081109.
(35) Yao, J.; Liu, T.; Wang, B. Optical properties for the oxygen vacancies in β-Ga_2O_3 based on first-principles calculations. *Materials Research Express* **2019**, *6* (7), 075913.
(36) Deák, P.; Duy Ho, Q.; Seemann, F.; Aradi, B.; Lorke, M.; Frauenheim, T. Choosing the correct hybrid for defect calculations: A case study on intrinsic carrier trapping in β-Ga_2O_3. *Physical Review B* **2017**, *95* (7), 075208.
(37) Ueda, N.; Hosono, H.; Waseda, R.; Kawazoe, H. Synthesis and control of conductivity of ultraviolet transmitting β-Ga_2O_3 single crystals. *Applied physics letters* **1997**, *70* (26), 3561-3563.

(38) Dong, L.; Jia, R.; Xin, B.; Zhang, Y. Effects of post-annealing temperature and oxygen concentration during sputtering on the structural and optical properties of β-Ga_2O_3 films. *Journal of Vacuum Science & Technology A* **2016**, *34* (6).
(39) Lee, Y.-J.; Schweitz, M. A.; Lee, S.-K.; Koh, J.-H.; Koo, S.-M. Effect of Oxygen Annealing on the Characteristics of Isotype Ga_2O_3/4H-SiC Heterojunction Diodes. *Journal of Nanoelectronics and Optoelectronics* **2020**, *15* (5), 561-565.
(40) Dong, L.; Jia, R.; Xin, B.; Peng, B.; Zhang, Y. Effects of oxygen vacancies on the structural and optical properties of β-Ga_2O_3. *Scientific reports* **2017**, *7* (1), 40160.
(41) Usseinov, A.; Koishybayeva, Z.; Platonenko, A.; Pankratov, V.; Suchikova, Y.; Akilbekov, A.; Zdorovets, M.; Purans, J.; Popov, A. I. Vacancy defects in Ga_2O_3: First-principles calculations of electronic structure. *Materials* **2021**, *14* (23), 7384.
(42) Sun, D.; Gao, Y.; Xue, J.; Zhao, J. Matching vacancy formation energy and defect levels with the density of amorphous Ga_2O_3. *Journal of Materials Science* **2020**, *55*, 9343-9353.
(43) Zacherle, T.; Schmidt, P.; Martin, M. Ab initio calculations on the defect structure of β-Ga_2O_3. *Physical Review B—Condensed Matter and Materials Physics* **2013**, *87* (23), 235206.
(44) Cheng, L.-C.; Huang, C.-Y.; Horng, R.-H. Thickness effect on operational modes of $ZnGa_2O_4$ MOSFETs. *IEEE Journal of the Electron Devices Society* **2018**, *6*, 432-437.
(45) Noto, L. L.; Mbongo, M. Photoluminescence and thermoluminescence properties of $ZnGa_2O_4$ prepared by a microwave assisted solid state reaction. *Physica B: Condensed Matter* **2020**, *578*, 411768.
(46) Chen, P. W.; Huang, S. Y.; Yuan, S. H.; Chen, Y. A.; Hsiao, P. W.; Wuu, D. S. Quasi-single-crystalline $ZnGa_2O_4$ films via solid phase epitaxy for enhancing deep-ultraviolet photoresponse. *Advanced Materials Interfaces* **2019**, *6* (18), 1901075.
(47) Galazka, Z.; Ganschow, S.; Schewski, R.; Irmscher, K.; Klimm, D.; Kwasniewski, A.; Pietsch, M.; Fiedler, A.; Schulze-Jonack, I.; Albrecht, M. Ultra-wide bandgap, conductive, high mobility, and high quality melt-grown bulk $ZnGa_2O_4$ single crystals. *APL Materials* **2018**, *7* (2), 022512.
(48) Look, D. C.; Leedy, K. D.; Horng, R.-H.; Santia, M. D.; Badescu, S. C. Electrical and optical properties of degenerate and semi-insulating $ZnGa_2O_4$: Electron/phonon scattering elucidated by quantum magnetoconductivity. *Applied Physics Letters* **2020**, *116* (25).
(49) Hirano, M. Hydrothermal synthesis and characterization of $ZnGa_2O_4$ spinel fine particles. *Journal of Materials Chemistry* **2000**, *10* (2), 469-472.
(50) Brik, M. G.; Suchocki, A.; Kaminska, A. Lattice parameters and stability of the spinel compounds in relation to the ionic radii and electronegativities of constituting chemical elements. *Inorganic chemistry* **2014**, *53* (10), 5088-5099.
(51) Wang, X.; Qiao, H.; Wang, X.; Xu, Y.; Liu, T.; Song, F.; An, Z.; Zhang, L.; Shi, F. NIR photoluminescence of $ZnGa_2O_4$: Cr nanoparticles synthesized by hydrothermal process. *Journal of Materials Science: Materials in Electronics* **2022**, *33* (24), 19129-19137.
(52) Sabino, F. P.; Chatratin, I.; Janotti, A.; Dalpian, G. M. Hole conductivity through a defect band in $ZnGa_2O_4$. *Physical Review Materials* **2022**, *6* (6), 064602.
(53) Shi, Y.; Ndione, P. F.; Lim, L. Y.; Sokaras, D.; Weng, T.-C.; Nagaraja, A. R.; Karydas, A. G.; Perkins, J. D.; Mason, T. O.; Ginley, D. S. Self-doping and electrical conductivity in spinel oxides: experimental validation of doping rules. *Chemistry of Materials* **2014**, *26* (5), 1867-1873.
(54) Janotti, A.; Van de Walle, C. G. Native point defects in ZnO. *Physical Review B* **2007**, *76* (16), 165202.

(55) Varley, J. B.; Weber, J. R.; Janotti, A.; Van de Walle, C. G. Oxygen vacancies and donor impurities in β-Ga_2O_3. *Applied physics letters* **2010**, *97* (14), 142106.
(56) De Vos, A.; Lejaeghere, K.; Vanpoucke, D. E.; Joos, J. J.; Smet, P. F.; Hemelsoet, K. First-principles study of antisite defect configurations in $ZnGa_2O_4$: Cr persistent phosphors. *Inorganic chemistry* **2016**, *55* (5), 2402-2412.
(57) Yang, W.; Li, J.; Liu, B.; Zhang, X.; Zhang, C.; Niu, P.; Jiang, X. Multi-wavelength tailoring of a $ZnGa_2O_4$ nanosheet phosphor via defect engineering. *Nanoscale* **2018**, *10* (40), 19039-19045.
(58) Chen, M.-I.; Singh, A. K.; Chiang, J.-L.; Horng, R.-H.; Wuu, D.-S. Zinc gallium oxide—A review from synthesis to applications. *Nanomaterials* **2020**, *10* (11), 2208.
(59) Wang, Y.-P.; Zhang, H.-S.; Lin, L.-T.; Zhou, S.-F.; Yao, Y.; Yang, X.-B.; Zhao, Y.-J. Role of intrinsic defects on the persistent luminescence of pristine and Mn doped $ZnGa_2O_4$. *Journal of Applied Physics* **2019**, *125* (9), 095701.
(60) Li, Y.; Duan, X.; Liao, H.; Qian, Y. Self-regulation synthesis of nanocrystalline $ZnGa_2O_4$ by hydrothermal reaction. *Chemistry of materials* **1998**, *10* (1), 17-18.
(61) Hirano, M.; Imai, M.; Inagaki, M. Preparation of $ZnGa_2O_4$ spinel fine particles by the hydrothermal method. *Journal of the American Ceramic Society* **2000**, *83* (4), 977-979.
(62) Liu, W.; Chan, Y.; Cai, J.; Leung, C.; Mak, C.; Wong, K.; Zhang, F.; Wu, X.; Qi, X. D. Understanding the formation of ultrafine spinel $CoFe_2O_4$ nanoplatelets and their magnetic properties. *Journal of Applied Physics* **2012**, *112* (10).
(63) Камзин, А.; Валиуллин, А. Структурные преобразования наночастиц Ni-= SUB=-1-x-=/SUB=-Cu-= SUB=-x-=/SUB=-Fe-= SUB=-2-=/SUB=-O-= SUB=-4-=/SUB=-в зависимости от количества ионов Cu. *Физика твердого тела* **2020**, *62* (7), 1091-1099.
(64) Liu, Q.; Wu, D.; Zhou, Y.; Su, H.; Wang, R.; Zhang, C.; Yan, S.; Xiao, M.; Zou, Z. Single-crystalline, ultrathin $ZnGa_2O_4$ nanosheet scaffolds to promote photocatalytic activity in CO_2 reduction into methane. *ACS applied materials & interfaces* **2014**, *6* (4), 2356-2361.
(65) Park, K.-W.; Yun, Y.-H.; Choi, S.-C. $ZnGa_2O_4$ thin films fabricated by Sol-gel spinning coating process. *Journal of electroceramics* **2006**, *17*, 263-266.
(66) Liu, B.; Bando, Y.; Dierre, B.; Sekiguchi, T.; Tang, C.; Mitome, M.; Wu, A.; Jiang, X.; Golberg, D. The synthesis, structure and cathodoluminescence of ellipsoid-shaped $ZnGa_2O_4$ nanorods. *Nanotechnology* **2009**, *20* (36), 365705.
(67) Kumar, S.; Sarau, G.; Tessarek, C.; Göbelt, M.; Christiansen, S.; Singh, R. Study of high quality spinel zinc gallate nanowires grown using CVD and ALD techniques. *Nanotechnology* **2015**, *26* (33), 335603.
(68) Horng, R.-H.; Huang, C.-Y.; Ou, S.-L.; Juang, T.-K.; Liu, P.-L. Epitaxial growth of ZnGa2O4: A new, deep ultraviolet semiconductor candidate. *Crystal Growth & Design* **2017**, *17* (11), 6071-6078.
(69) Teh, C. M.; Mohamed, A. R. Roles of titanium dioxide and ion-doped titanium dioxide on photocatalytic degradation of organic pollutants (phenolic compounds and dyes) in aqueous solutions: A review. *Journal of Alloys and Compounds* **2011**, *509* (5), 1648-1660.
(70) Mills, A.; Le Hunte, S. An overview of semiconductor photocatalysis. *Journal of photochemistry and photobiology A: Chemistry* **1997**, *108* (1), 1-35.
(71) Linsebigler, A. L.; Lu, G.; Yates Jr, J. T. Photocatalysis on TiO_2 surfaces: principles, mechanisms, and selected results. *Chemical reviews* **1995**, *95* (3), 735-758.
(72) Carp, O.; Huisman, C. L.; Reller, A. Photoinduced reactivity of titanium dioxide. *Progress in solid state chemistry* **2004**, *32* (1-2), 33-177.

(73) Liu, B.; Zhao, X.; Terashima, C.; Fujishima, A.; Nakata, K. Thermodynamic and kinetic analysis of heterogeneous photocatalysis for semiconductor systems. *Physical Chemistry Chemical Physics* **2014**, *16* (19), 8751-8760.
(74) Liu, L.; Huang, J.; Cao, L.; Wu, J.; Fei, J.; Ouyang, H.; Yao, C. Influence of temperature on the morphology and photocatalytic activity of $ZnGa_2O_4$ crystallites prepared by hydrothermal method. *Ceramics International* **2013**, *39* (3), 3165-3171.
(75) Tien, L.-C.; Tseng, C.-C.; Chen, Y.-L.; Ho, C.-H. Direct vapor transport synthesis of ZnGa2O4 nanowires with superior photocatalytic activity. *Journal of alloys and compounds* **2013**, *555*, 325-329.
(76) Zhang, W.; Zhang, J.; Chen, Z.; Wang, T. Photocatalytic degradation of methylene blue by $ZnGa_2O_4$ thin films. *Catalysis Communications* **2009**, *10* (13), 1781-1785.
(77) Yuan, Y.; Huang, J.; Tu, W.; Huang, S. Synthesis of uniform $ZnGa_2O_4$ nanoparticles with high photocatalytic activity. *Journal of alloys and compounds* **2014**, *616*, 461-467.
(78) Song, H.; Zhu, L.; Li, Y.; Lou, Z.; Xiao, M.; Ye, Z. Preparation of $ZnFe_2O_4$ nanostructures and highly efficient visible-light-driven hydrogen generation with the assistance of nanoheterostructures. *Journal of Materials Chemistry A* **2015**, *3* (16), 8353-8360.
(79) Liu, J.; Lu, W.; Wu, H.; Jin, L.; Hu, B.; Li, L.; Wang, Z. In situ synthesis of rice-like $ZnGa_2O_4$ for the photocatalytic removal of organic and inorganic pollutants. *Materials Science in Semiconductor Processing* **2016**, *56*, 251-259.
(80) Chen, D.; Wang, Z.; Ren, T.; Ding, H.; Yao, W.; Zong, R.; Zhu, Y. Influence of defects on the photocatalytic activity of ZnO. *The Journal of Physical Chemistry C* **2014**, *118* (28), 15300-15307.
(81) Kong, M.; Li, Y.; Chen, X.; Tian, T.; Fang, P.; Zheng, F.; Zhao, X. Tuning the relative concentration ratio of bulk defects to surface defects in TiO_2 nanocrystals leads to high photocatalytic efficiency. *Journal of the American Chemical Society* **2011**, *133* (41), 16414-16417.
(82) Zhong, J. B.; Li, J. Z.; Zeng, J.; He, X. Y.; Hu, W.; Shen, Y. C. Enhanced photocatalytic performance of Ga^{3+}-doped ZnO. *Materials Research Bulletin* **2012**, *47* (11), 3893-3896.
(83) Chiu, H.-M.; Wu, J.-M. Opto-electrical properties and chemisorption reactivity of Ga-doped ZnO nanopagodas. *Journal of Materials Chemistry A* **2013**, *1* (18), 5524-5534.
(84) Du, F.; Yang, D.; Sun, Y.; Jiao, Y.; Teng, F.; Fan, H. Electrospun Zn-doped Ga_2O_3 nanofibers and their application in photodegrading rhodamine B dye. *Ceramics International* **2021**, *47* (4), 4963-4971.
(85) Jin, S.; Lu, W.; Stanish, P. C.; Radovanovic, P. V. Compositional control of the photocatalytic activity of Ga_2O_3 nanocrystals enabled by defect-induced carrier trapping. *Chemical Physics Letters* **2018**, *706*, 509-514.
(86) Li, H.; Wu, Z.; Wu, S.; Tian, P.; Fang, Z. $(Al_xGa_{1-x})_2O_3$-based materials: Growth, properties, and device applications. *Journal of Alloys and Compounds* **2023**, *960*, 170671.
(87) Varley, J. B. First-principles calculations of structural, electrical, and optical properties of ultra-wide bandgap $(Al_xGa_{1-x})_2O_3$ alloys. *Journal of Materials Research* **2021**, *36* (23), 4790-4803.
(88) Kim, H. W.; Ko, H.; Chung, Y.-C.; Cho, S. B. Heterostructural phase diagram of Ga_2O_3–based solid solution with Al_2O_3. *Journal of the European Ceramic Society* **2021**, *41* (1), 611-616.
(89) Kaun, S. W.; Wu, F.; Speck, J. S. β-$(Al_xGa_{1-x})_2O_3/Ga_2O_3$ (010) heterostructures grown on β-Ga_2O_3 (010) substrates by plasma-assisted molecular beam epitaxy. *Journal of Vacuum Science & Technology A* **2015**, *33* (4).

(90) Anhar Uddin Bhuiyan, A. F. M.; Feng, Z.; Johnson, J. M.; Chen, Z.; Huang, H.-L.; Hwang, J.; Zhao, H. MOCVD epitaxy of β-$(Al_xGa_{1-x})_2O_3$ thin films on (010) Ga_2O_3 substrates and N-type doping. *Applied Physics Letters* **2019**, *115* (12).
(91) Johnson, J. M.; Huang, H.-L.; Wang, M.; Mu, S.; Varley, J. B.; Uddin Bhuiyan, A. F. M.; Feng, Z.; Kalarickal, N. K.; Rajan, S.; Zhao, H. Atomic scale investigation of aluminum incorporation, defects, and phase stability in β-$(Al_xGa_{1-x})_2O_3$ films. *APL Materials* **2021**, *9* (5).
(92) Ito, H.; Kaneko, K.; Fujita, S. Growth and band gap control of corundum-structured α-$(AlGa)_2O_3$ thin films on sapphire by spray-assisted mist chemical vapor deposition. *Japanese Journal of Applied Physics* **2012**, *51* (10R), 100207.
(93) Kaneko, K.; Suzuki, K.; Ito, Y.; Fujita, S. Growth characteristics of corundum-structured α-$(Al_xGa_{1-x})_2O_3/Ga_2O_3$ heterostructures on sapphire substrates. *Journal of Crystal Growth* **2016**, *436*, 150-154.
(94) Lee, S.-D.; Ito, Y.; Kaneko, K.; Fujita, S. Enhanced thermal stability of alpha gallium oxide films supported by aluminum doping. *Japanese Journal of Applied Physics* **2015**, *54* (3), 030301.
(95) Krueger, B. W.; Dandeneau, C. S.; Nelson, E. M.; Dunham, S. T.; Ohuchi, F. S.; Olmstead, M. A. Variation of band gap and lattice parameters of β−$(Al_xGa_{1-x})_2O_3$ powder produced by solution combustion synthesis. *Journal of the American Ceramic Society* **2016**, *99* (7), 2467-2473.
(96) Song, D.; Li, L.; Li, B.; Sui, Y.; Shen, A. Band gap engineering of N-alloyed Ga_2O_3 thin films. *Aip Advances* **2016**, *6* (6).
(97) Seacat, S.; Lyons, J. L.; Peelaers, H. Orthorhombic alloys of Ga_2O_3 and Al_2O_3. *Applied physics letters* **2020**, *116* (23).
(98) Hu, W.; Li, S.; Hu, Y.; Wan, L.; Jiao, S.; Hu, W.; Talwar, D. N.; Feng, Z. C.; Li, T.; Xu, J. Optical and electronic properties of $(Al_xGa_{1-x})_2O_3/Al_2O_3$ (x> 0.4) films grown by magnetron sputtering. *Journal of Alloys and Compounds* **2021**, *864*, 158765.
(99) Yuan, S.-H.; Ou, S.-L.; Chen, C.-M.; Huang, S.-Y.; Hsiao, B.-W.; Wuu, D.-S. Characterization of aluminum gallium oxide films grown by pulsed laser deposition. *Ceramics International* **2019**, *45* (1), 702-707.
(100) Wang, X.; Chen, Z.; Zhang, F.; Saito, K.; Tanaka, T.; Nishio, M.; Guo, Q. Influence of substrate temperature on the properties of $(AlGa)_2O_3$ thin films prepared by pulsed laser deposition. *Ceramics International* **2016**, *42* (11), 12783-12788.
(101) Yuan, S.-H.; Wang, C.-C.; Huang, S.-Y.; Wuu, D.-S. Improved responsivity drop from 250 to 200 nm in sputtered gallium oxide photodetectors by incorporating trace aluminum. *IEEE Electron Device Letters* **2017**, *39* (2), 220-223.
(102) Wang, C.-C.; Yuan, S.-H.; Ou, S.-L.; Huang, S.-Y.; Lin, K.-Y.; Chen, Y.-A.; Hsiao, P.-W.; Wuu, D.-S. Growth and characterization of co-sputtered aluminum-gallium oxide thin films on sapphire substrates. *Journal of Alloys and Compounds* **2018**, *765*, 894-900.
(103) Oshima, T.; Okuno, T.; Fujita, S. Ga_2O_3 thin film growth on c-plane sapphire substrates by molecular beam epitaxy for deep-ultraviolet photodetectors. *Japanese Journal of Applied Physics* **2007**, *46* (11R), 7217.
(104) Bhuiyan, A. F. M.; Feng, Z.; Huang, H.-L.; Meng, L.; Hwang, J.; Zhao, H. Band offsets at metalorganic chemical vapor deposited β-$(AlxGa_{1-x})_2O_3$/β-Ga_2O_3 interfaces—Crystalline orientation dependence. *Journal of Vacuum Science & Technology A* **2021**, *39* (6).
(105) Berencén, Y.; Xie, Y.; Wang, M.; Prucnal, S.; Rebohle, L.; Zhou, S. Structural and optical properties of pulsed-laser deposited crystalline β-Ga_2O_3 thin films on silicon. *Semiconductor Science and Technology* **2019**, *34* (3), 035001.

(106) Ho, Q. D.; Frauenheim, T.; Deák, P. Origin of photoluminescence in β-Ga_2O_3. *Physical Review B* **2018**, *97* (11), 115163.
(107) Kityk, I. V.; Makowska-Janusik, M.; Fontana, M. D.; Aillerie, M.; Abdi, F. Nonstoichiometric defects and optical properties in $LiNbO_3$. *The Journal of Physical Chemistry B* **2001**, *105* (49), 12242-12248.
(108) Lany, S.; Zunger, A. Many-body GW calculation of the oxygen vacancy in ZnO. *Physical Review B—Condensed Matter and Materials Physics* **2010**, *81* (11), 113201.
(109) Ma, X.; Zhang, Y.; Dong, L.; Jia, R. First-principles calculations of electronic and optical properties of aluminum-doped β-Ga_2O_3 with intrinsic defects. *Results in physics* **2017**, *7*, 1582-1589.
(110) Wu, X.; Selloni, A.; Nayak, S. K. First principles study of CO oxidation on TiO_2 (110): The role of surface oxygen vacancies. *The Journal of chemical physics* **2004**, *120* (9), 4512-4516.
(111) Jensen, W. B. The place of zinc, cadmium, and mercury in the periodic table. *Journal of Chemical Education* **2003**, *80* (8), 952.
(112) Masterton, W. L.; Hurley, C. N. Chemistry: principles and reactions. *(No Title)* **1989**.
(113) Atkins, P. W.; Ratcliffe, R. G.; de Paula, J.; Wormald, M. *Physical chemistry for the life sciences*; Oxford University Press, 2023.
(114) Dickey, M. D. Emerging applications of liquid metals featuring surface oxides. *ACS applied materials & interfaces* **2014**, *6* (21), 18369-18379.
(115) Narh, K. A.; Dwivedi, V. P.; Grow, J. M.; Stana, A.; Shih, W. Y. The effect of liquid gallium on the strengths of stainless steel and thermoplastics. *Journal of materials science* **1998**, *33*, 329-337.
(116) Anderson, T. J.; Ansara, I. The Ga-In (gallium-indium) system. *Journal of phase equilibria* **1991**, *12*, 64-72.
(117) Daeneke, T.; Khoshmanesh, K.; Mahmood, N.; De Castro, I. A.; Esrafilzadeh, D.; Barrow, S. J.; Dickey, M. D.; Kalantar-Zadeh, K. Liquid metals: fundamentals and applications in chemistry. *Chemical Society Reviews* **2018**, *47* (11), 4073-4111.
(118) Allioux, F.-M.; Ghasemian, M. B.; Xie, W.; O'Mullane, A. P.; Daeneke, T.; Dickey, M. D.; Kalantar-Zadeh, K. Applications of liquid metals in nanotechnology. *Nanoscale Horizons* **2022**, *7* (2), 141-167.
(119) Jalili, A. R.; Satalov, A.; Nazari, S.; Rahmat Suryanto, B. H.; Sun, J.; Ghasemian, M. B.; Mayyas, M.; Kandjani, A. E.; Sabri, Y. M.; Mayes, E. Liquid crystal-mediated 3D printing process to fabricate nano-ordered layered structures. *ACS Applied Materials & Interfaces* **2021**, *13* (24), 28627-28638.
(120) Allioux, F.-M.; Merhebi, S.; Ghasemian, M. B.; Tang, J.; Merenda, A.; Abbasi, R.; Mayyas, M.; Daeneke, T.; O'Mullane, A. P.; Daiyan, R. Bi–Sn catalytic foam governed by nanometallurgy of liquid metals. *Nano letters* **2020**, *20* (6), 4403-4409.
(121) Han, J.; Mayyas, M.; Tang, J.; Mousavi, M.; Idrus-Saidi, S. A.; Cai, S.; Cao, Z.; Wang, Y.; Tang, J.; Jalili, R. Liquid metal enabled continuous flow reactor: A proof-of-concept. *Matter* **2021**, *4* (12), 4022-4041.
(122) Zhao, S.; Zhang, J.; Fu, L. Liquid metals: a novel possibility of fabricating 2D metal oxides. *Advanced Materials* **2021**, *33* (9), 2005544.
(123) Aukarasereenont, P.; Goff, A.; Nguyen, C. K.; McConville, C. F.; Elbourne, A.; Zavabeti, A.; Daeneke, T. Liquid metals: an ideal platform for the synthesis of two-dimensional materials. *Chemical Society Reviews* **2022**, *51* (4), 1253-1276.
(124) D'Evelyn, M. P.; Rice, S. A. A pseudoatom theory for the liquid–vapor interface of simple metals: Computer simulation studies of sodium and cesium. *The Journal of chemical physics* **1983**, *78* (8), 5225-5249.

(125) D'Evelyn, M. P.; Rice, S. A. A study of the liquid–vapor interface of mercury: Computer simulation results. *The Journal of chemical physics* **1983**, *78* (8), 5081-5095.
(126) Regan, M. J.; Pershan, P. S.; Magnussen, O. M.; Ocko, B. M.; Deutsch, M.; Berman, L. E. X-ray reflectivity studies of liquid metal and alloy surfaces. *Physical Review B* **1997**, *55* (23), 15874.
(127) Xu, Q.; Oudalov, N.; Guo, Q.; Jaeger, H. M.; Brown, E. Effect of oxidation on the mechanical properties of liquid gallium and eutectic gallium-indium. *Physics of fluids* **2012**, *24* (6).
(128) Akbari, M. K.; Verpoort, F.; Zhuiykov, S. State-of-the-art surface oxide semiconductors of liquid metals: An emerging platform for development of multifunctional two-dimensional materials. *Journal of Materials Chemistry A* **2021**, *9* (1), 34-73.
(129) Regan, M. J.; Tostmann, H.; Pershan, P. S.; Magnussen, O. M.; DiMasi, E.; Ocko, B. M.; Deutsch, M. X-ray study of the oxidation of liquid-gallium surfaces. *Physical Review B* **1997**, *55* (16), 10786.
(130) Eaker, C. B.; Dickey, M. D. Liquid metals as ultra-stretchable, soft, and shape reconfigurable conductors. 2015, SPIE: Vol. 9467, pp 21-29.
(131) Kazem, N.; Hellebrekers, T.; Majidi, C. Soft multifunctional composites and emulsions with liquid metals. *Advanced Materials* **2017**, *29* (27), 1605985.
(132) Ghasemian, M. B.; Zavabeti, A.; Mousavi, M.; Murdoch, B. J.; Christofferson, A. J.; Meftahi, N.; Tang, J.; Han, J.; Jalili, R.; Allioux, F. M. Doping process of 2D materials based on the selective migration of dopants to the interface of liquid metals. *Advanced Materials* **2021**, *33* (43), 2104793.
(133) Norrby, L. J. Why is mercury liquid? Or, why do relativistic effects not get into chemistry textbooks? *Journal of Chemical Education* **1991**, *68* (2), 110.
(134) Lide, D. R. *CRC handbook of chemistry and physics*; CRC press, 2004.
(135) Heine, V. Crystal structure of gallium metal. *Journal of Physics C: Solid State Physics* **1968**, *1* (1), 222.
(136) Qusba, A.; RamRakhyani, A. K.; So, J.-H.; Hayes, G. J.; Dickey, M. D.; Lazzi, G. On the design of microfluidic implant coil for flexible telemetry system. *IEEE Sensors Journal* **2014**, *14* (4), 1074-1080.
(137) Yu, S.; Kaviany, M. Electrical, thermal, and species transport properties of liquid eutectic Ga-In and Ga-In-Sn from first principles. *The Journal of chemical physics* **2014**, *140* (6).
(138) Shpyrko, O. G.; Streitel, R.; Balagurusamy, V. S. K.; Grigoriev, A. Y.; Deutsch, M.; Ocko, B. M.; Meron, M.; Lin, B.; Pershan, P. S. Surface crystallization in a liquid AuSi alloy. *Science* **2006**, *313* (5783), 77-80.
(139) Bozack, M. J.; Bell, A. E.; Swanson, L. W. Influence of surface segregation on wetting of liquid metal alloys. *The Journal of Physical Chemistry* **1988**, *92* (13), 3925-3934.
(140) Shpyrko, O.; Fukuto, M.; Pershan, P.; Ocko, B.; Kuzmenko, I.; Gog, T.; Deutsch, M. Surface layering of liquids: The role of surface tension. *Physical Review B* **2004**, *69* (24), 245423.
(141) Regan, M. J.; Kawamoto, E. H.; Lee, S.; Pershan, P. S.; Maskil, N.; Deutsch, M.; Magnussen, O. M.; Ocko, B. M.; Berman, L. E. Surface layering in liquid gallium: An X-ray reflectivity study. *Physical review letters* **1995**, *75* (13), 2498.
(142) Magnussen, O. M.; Ocko, B. M.; Regan, M. J.; Penanen, K.; Pershan, P. S.; Deutsch, M. X-ray reflectivity measurements of surface layering in liquid mercury. *Physical review letters* **1995**, *74* (22), 4444.

(143) Lei, N.; Huang, Z.; Rice, S. A. Structure of the liquid–vapor interface of a Sn: Ga alloy. *The Journal of chemical physics* **1997**, *107* (10), 4051-4060.
(144) Lei, N.; Huang, Z.; Rice, S. A. Surface segregation and layering in the liquid–vapor interface of a dilute bismuth: gallium alloy. *The Journal of chemical physics* **1996**, *104* (12), 4802-4805.
(145) Tostmann, H.; DiMasi, E.; Shpyrko, O. G.; Pershan, P. S.; Ocko, B. M.; Deutsch, M. II. Surface and interfacial phenomena: Surface phases in binary liquid metal alloys: An X-ray study. *Berichte der Bunsengesellschaft für physikalische Chemie* **1998**, *102* (9), 1136-1141.
(146) Huisman, W. J.; Peters, J. F.; Zwanenburg, M. J.; de Vries, S. A.; Derry, T. E.; Abernathy, D.; van der Veen, J. F. Layering of a liquid metal in contact with a hard wall. *Nature* **1997**, *390* (6658), 379-381.
(147) Ermoline, A.; Dreizin, E. L. Equations for the Cabrera–Mott kinetics of oxidation for spherical nanoparticles. *Chemical Physics Letters* **2011**, *505* (1-3), 47-50.
(148) Cabrera, N.; Mott, N. F. Theory of the oxidation of metals. *Reports on progress in physics* **1949**, *12* (1), 163.
(149) Ghasemian, M. B.; Zavabeti, A.; Abbasi, R.; Kumar, P. V.; Syed, N.; Yao, Y.; Tang, J.; Wang, Y.; Elbourne, A.; Han, J. Ultra-thin lead oxide piezoelectric layers for reduced environmental contamination using a liquid metal-based process. *Journal of Materials Chemistry A* **2020**, *8* (37), 19434-19443.
(150) Mahmood, N.; Khan, H.; Tran, K.; Kuppe, P.; Zavabeti, A.; Atkin, P.; Ghasemian, M. B.; Yang, J.; Xu, C.; Tawfik, S. A. Maximum piezoelectricity in a few unit-cell thick planar ZnO–A liquid metal-based synthesis approach. *Materials Today* **2021**, *44*, 69-77.
(151) Li, J.; Zhang, X.; Yang, B.; Zhang, C.; Xu, T.; Chen, L.; Yang, L.; Jin, X.; Liu, B. Template approach to large-area non-layered Ga-group two-dimensional crystals from printed skin of liquid gallium. *Chemistry of Materials* **2021**, *33* (12), 4568-4577.
(152) Daeneke, T.; Atkin, P.; Orrell-Trigg, R.; Zavabeti, A.; Ahmed, T.; Walia, S.; Liu, M.; Tachibana, Y.; Javaid, M.; Greentree, A. D. Wafer-scale synthesis of semiconducting SnO monolayers from interfacial oxide layers of metallic liquid tin. *ACS nano* **2017**, *11* (11), 10974-10983.
(153) Messalea, K. A.; Carey, B. J.; Jannat, A.; Syed, N.; Mohiuddin, M.; Zhang, B. Y.; Zavabeti, A.; Ahmed, T.; Mahmood, N.; Della Gaspera, E. Bi_2O_3 monolayers from elemental liquid bismuth. *Nanoscale* **2018**, *10* (33), 15615-15623.
(154) Atkin, P.; Orrell-Trigg, R.; Zavabeti, A.; Mahmood, N.; Field, M. R.; Daeneke, T.; Cole, I. S.; Kalantar-Zadeh, K. Evolution of 2D tin oxides on the surface of molten tin. *Chemical Communications* **2018**, *54* (17), 2102-2105.
(155) Cooke, J.; Ghadbeigi, L.; Sun, R.; Bhattacharyya, A.; Wang, Y.; Scarpulla, M. A.; Krishnamoorthy, S.; Sensale-Rodriguez, B. Synthesis and Characterization of Large-Area Nanometer-Thin β-Ga_2O_3 Films from Oxide Printing of Liquid Metal Gallium. *physica status solidi (a)* **2020**, *217* (10), 1901007.
(156) Datta, R. S.; Syed, N.; Zavabeti, A.; Jannat, A.; Mohiuddin, M.; Rokunuzzaman, M.; Yue Zhang, B.; Rahman, M. A.; Atkin, P.; Messalea, K. A. Flexible two-dimensional indium tin oxide fabricated using a liquid metal printing technique. *Nature Electronics* **2020**, *3* (1), 51-58.
(157) Chen, L.; Liu, Y.; Lu, Z.; Huang, K. Hydrothermal synthesis and characterization of $ZnGa_2O_4$ phosphors. *Materials chemistry and physics* **2006**, *97* (2-3), 247-251.
(158) Baykara, M. Z.; Schwendemann, T. C.; Altman, E. I.; Schwarz, U. D. Three-dimensional atomic force microscopy–taking surface imaging to the next level. *Advanced materials* **2010**, *22* (26-27), 2838-2853.

(159) HORIBA. *cathodoluminescence-spectroscopy-EM-add-on-Detector*. n.d. https://www.horiba.com/fra/cathodoluminescence-spectroscopy-em-add-on-detector/ (accessed 1 April 2025).
(160) Ton-That, C.; Phillips, M. Cathodoluminescence microanalysis of ZnO nanowires. In *Semiconductor Nanowires*, Elsevier, 2015; pp 393-407.
(161) Phillips, M. R.; Telg, H.; Kucheyev, S. O.; Gelhausen, O.; Toth, M. Cathodoluminescence efficiency dependence on excitation density in n-type gallium nitride. *Microscopy and Microanalysis* **2003**, *9* (2), 144-151.
(162) Müllhaüser, J.; Brandt, O.; Yang, H.; Ploog, K. Exciton luminescence of single-crystal GaN. *MRS Online Proceedings Library (OPL)* **1995**, *395*, 607.
(163) Singh, R.; Molnar, R.; Ünlü, M.; Moustakas, T. Intensity dependence of photoluminescence in GaN thin films. *Applied physics letters* **1994**, *64* (3), 336-338.
(164) Reshchikov, M.; Korotkov, R. Analysis of the temperature and excitation intensity dependencies of photoluminescence in undoped GaN films. *Physical Review B* **2001**, *64* (11), 115205.
(165) Pearton, S. J.; Yang, J.; Cary IV, P. H.; Ren, F.; Kim, J.; Tadjer, M. J.; Mastro, M. A. A review of Ga2O3 materials, processing, and devices. *Applied Physics Reviews* **2018**, *5* (1), 011301.
(166) Huynh, T. T.; Chikoidze, E.; Irvine, C. P.; Zakria, M.; Dumont, Y.; Teherani, F. H.; Sandana, E. V.; Bove, P.; Rogers, D. J.; Phillips, M. R.; Ton-That, C. Red luminescence in H-doped β− Ga_2O_3. *Physical Review Materials* **2020**, *4* (8), 085201.
(167) Frodason, Y. K.; Galeckas, A.; Olsen, V. S.; Weiser, P. M.; Galazka, Z.; Van de Walle, C. G.; Vines, L. Intrinsic origins of broad luminescence in melt-grown $ZnGa_2O_4$ single crystals. *Physical Review Materials* **2024**, *8* (9), 094604.
(168) Zhao, P.; Li, Y.; Li, L.; Bu, S.; Fan, W. Oxygen vacancy-modified B-/N-Codoped $ZnGa_2O_4$ nanospheres with enhanced photocatalytic hydrogen evolution performance in the absence of a Pt cocatalyst. *The Journal of Physical Chemistry C* **2018**, *122* (20), 10737-10748.
(169) Schweke, D.; Mordehovitz, Y.; Halabi, M.; Shelly, L.; Hayun, S. Defect chemistry of oxides for energy applications. *Advanced Materials* **2018**, *30* (41), 1706300.
(170) Khan, S.; Je, M.; Kim, D.; Lee, S.; Cho, S.-H.; Song, T.; Choi, H. Mapping point defects of brookite TiO2 for photocatalytic activity beyond anatase and P25. *The Journal of Physical Chemistry C* **2020**, *124* (19), 10376-10384.
(171) Salih, A. K.; Phillips, M. R.; Ton-That, C. Enhanced solar-driven water splitting performance using oxygen vacancy rich ZnO photoanodes. *Solar Energy Materials and Solar Cells* **2023**, *259*, 112436.
(172) Elrahoumi, R.; Zhu, L.; Wagner, E.; Maudez, W.; Benvenuti, G.; Phillips, M. R.; Ton-That, C. Doping-induced Ti3+ state and oxygen vacancies in TiO_2: A single-chip combinatorial investigation. *Materials Chemistry and Physics* **2023**, *308*, 128283.
(173) Chen, Z.; Chen, W.; Han, P.; Yang, J.; Wan, Z.; Hu, P.; Teng, F.; Fan, H. Enhanced photocatalytic degradation of tetracycline hydrochloride by hollow nanofiber Ag@ $ZnGa_2O_4$/ZnO with synergistic effects of LSPR and S-scheme interface engineering. *Journal of Materials Chemistry C* **2024**, *12* (43), 17448-17457.
(174) Chen, W.; Kang, T.; Du, F.; Han, P.; Gao, M.; Hu, P.; Teng, F.; Fan, H. A new S-scheme heterojunction of 1D $ZnGa_2O_4$/ZnO nanofiber for efficient photocatalytic degradation of TC-HCl. *Environmental Research* **2023**, *232*, 116388.
(175) Monshi, A.; Foroughi, M. R.; Monshi, M. R. Modified Scherrer equation to estimate more accurately nano-crystallite size using XRD. *World journal of nano science and engineering* **2012**, *2* (3), 154-160.

(176) Hussen, M. K.; Dejene, F. B.; Gonfa, G. G. Effect of citric acid on material properties of $ZnGa_2O_4$: Cr^{3+} nanopowder prepared by sol–gel method. *Applied Physics A* **2018**, *124*, 1-10.
(177) Lucero, J.; Elsaidi, S. K.; Anderson, R.; Wu, T.; Gómez-Gualdrón, D. A.; Thallapally, P. K.; Carreon, M. A. Time dependent structural evolution of porous organic cage CC3. *Crystal Growth & Design* **2018**, *18* (2), 921-927.
(178) Motloung, S.; Tsega, M.; Dejene, F.; Swart, H.; Ntwaeaborwa, O.; Koao, L.; Motaung, T.; Hato, M. Effect of annealing temperature on structural and optical properties of ZnAl2O4: 1.5% Pb2+ nanocrystals synthesized via sol-gel reaction. *Journal of Alloys and Compounds* **2016**, *677*, 72-79.
(179) Kramer, M. J.; Mendelev, M. I.; Napolitano, R. E. In situ observation of antisite defect formation during crystal growth. *Physical review letters* **2010**, *105* (24), 245501.
(180) Wang, L.; Zhang, W.; Liu, N.; Zhang, T.; Wang, Z.; Wu, S.; Zhan, Z.; Ye, J. Epitaxial growth and stoichiometry control of ultrawide bandgap $ZnGa_2O_4$ films by pulsed laser deposition. *Coatings* **2021**, *11* (7), 782.
(181) Oshima, T.; Niwa, M.; Mukai, A.; Nagami, T.; Suyama, T.; Ohtomo, A. Epitaxial growth of wide-band-gap $ZnGa_2O_4$ films by mist chemical vapor deposition. *Journal of crystal growth* **2014**, *386*, 190-193.
(182) Errandonea, D.; Kumar, R. S.; Manjón, F. J.; Ursaki, V.; Rusu, E. Post-spinel transformations and equation of state in $ZnGa_2O_4$: Determination at high pressure by in situ x-ray diffraction. *Physical Review B* **2009**, *79* (2), 024103.
(183) López-Moreno, S.; Rodríguez-Hernández, P.; Muñoz, A.; Romero, A.; Manjón, F.; Errandonea, D.; Rusu, E.; Ursaki, V. Lattice dynamics of ZnAl2O4 and $ZnGa_2O_4$ under high pressure. *Annalen der Physik* **2011**, *523* (1-2), 157-167.
(184) Khan, J. A.; Maithani, Y.; Horng, R. H.; Singh, J. Investigating mechanical properties of sintered $ZnGa_2O_4$ ceramics using nanoindentation. *Ceramics International* **2022**, *48* (18), 27064-27075.
(185) Relvas, M.; Soares, M.; Pereira, S.; Girão, A.; Costa, F.; Monteiro, T. Trends in Cr3+ red emissions from $ZnGa_2O_4$ nanostructures produced by pulsed laser ablation in a liquid medium. *Journal of Physics and Chemistry of Solids* **2019**, *129*, 413-423.
(186) Rao, R.; Rao, A.; Xu, B.; Dong, J.; Sharma, S.; Sunkara, M. Blueshifted Raman scattering and its correlation with the [110] growth direction in gallium oxide nanowires. *Journal of Applied Physics* **2005**, *98* (9), 094312.
(187) Onuma, T.; Fujioka, S.; Yamaguchi, T.; Itoh, Y.; Higashiwaki, M.; Sasaki, K.; Masui, T.; Honda, T. Polarized Raman spectra in β-Ga_2O_3 single crystals. *Journal of crystal growth* **2014**, *401*, 330-333.
(188) Hee, P.; Christensen, R.; Ledemi, Y.; Wren, J. E.; Dussauze, M.; Cardinal, T.; Fargin, E.; Kroeker, S.; Messaddeq, Y. Properties and structural investigation of gallophosphate glasses by 71 Ga and 31 P nuclear magnetic resonance and vibrational spectroscopies. *Journal of Materials Chemistry C* **2014**, *2* (37), 7906-7917.
(189) Manjón, F.; Mari, B.; Serrano, J.; Romero, A. Silent Raman modes in zinc oxide and related nitrides. *Journal of applied physics* **2005**, *97* (5).
(190) Li, N.; Duan, X.; Yu, F.; Jiang, H. Effects of preparation method and temperature on the cation distribution of $ZnGa_2O_4$ spinel studied by X-ray photoelectron spectroscopy. *Vacuum* **2017**, *142*, 1-4.
(191) Yang, W.; Li, J.; Liu, B.; Zhang, X.; Zhang, C.; Niu, P.; Jiang, X. Multi-wavelength tailoring of a $ZnGa_2O_4$ nanosheet phosphor via defect engineering. *Nanoscale* **2018**, *10* (40), 19039-19045.

(192) Jiang, L.; Li, J.; Huang, K.; Li, S.; Wang, Q.; Sun, Z.; Mei, T.; Wang, J.; Zhang, L.; Wang, N. Low-temperature and solution-processable zinc oxide transistors for transparent electronics. *ACS omega* **2017**, *2* (12), 8990-8996.
(193) Chen, Y.; Sakata, O.; Morita, H.; Matsuda, A.; Jia, F.; Seo, O.; Kumara, L. S. R.; Ina, T.; Kobayashi, E.; Kim, J. Electronic states of gallium oxide epitaxial thin films and related atomic arrangement. *Applied Surface Science* **2022**, *578*, 151943.
(194) Chiou, J.; Jan, J.; Tsai, H.; Bao, C.; Pong, W.-F.; Tsai, M.-H.; Hong, I.-H.; Klauser, R.; Lee, J.; Wu, J. Electronic structure of ZnO nanorods studied by angle-dependent x-ray absorption spectroscopy and scanning photoelectron microscopy. *Applied physics letters* **2004**, *84* (18), 3462-3464.
(195) Choi, S.; Phillips, M. R.; Aharonovich, I.; Pornsuwan, S.; Cowie, B. C.; Ton-That, C. Photophysics of point defects in ZnO nanoparticles. *Advanced Optical Materials* **2015**, *3* (6), 821-827.
(196) Yamamura, K.; Zhu, L.; Irvine, C. P.; Scott, J. A.; Singh, M.; Jallandhra, A.; Bansal, V.; Phillips, M. R.; Ton-That, C. Defect compensation in nitrogen-doped β-Ga_2O_3 nanowires: implications for bipolar nanoscale devices. *ACS Applied Nano Materials* **2022**, *5* (9), 12087-12094.
(197) He, X.; Wang, M.; Meng, J.; Hu, J.; Jiang, Y. The effect of vacancy defects on the electronic properties of β-Ga_2O_3. *Computational Materials Science* **2022**, *215*, 111777.
(198) Kim, J.; Kang, H.; Kim, W.; Kim, J.; Choi, J.; Park, H.; Kim, G.; Kim, T.; Hwang, Y.; Mho, S. Color variation of ZnGa 2 O 4 phosphor by reduction-oxidation processes. *Applied physics letters* **2003**, *82* (13), 2029-2031.
(199) Ton-That, C.; Weston, L.; Phillips, M. Characteristics of point defects in the green luminescence from Zn-and O-rich ZnO. *Physical Review B* **2012**, *86* (11), 115205.
(200) Zhang, Y.; Wu, Z.; Geng, D.; Kang, X.; Shang, M.; Li, X.; Lian, H.; Cheng, Z.; Lin, J. Full color emission in $ZnGa_2O_4$: simultaneous control of the spherical morphology, luminescent, and electric properties via hydrothermal approach. *Advanced Functional Materials* **2014**, *24* (42), 6581-6593.
(201) Zou, L.; Xiang, X.; Wei, M.; Li, F.; Evans, D. G. Single-crystalline $ZnGa_2O_4$ spinel phosphor via a single-source inorganic precursor route. *Inorganic chemistry* **2008**, *47* (4), 1361-1369.
(202) Gu, Z.; Liu, F.; Li, X.; Howe, J.; Xu, J.; Zhao, Y.; Pan, Z. Red, green, and blue luminescence from $ZnGa_2O_4$ nanowire arrays. *The Journal of Physical Chemistry Letters* **2010**, *1* (1), 354-357.
(203) Xi, J.; Zhang, Y.; Chen, X.; Hu, Y. A simple sol–gel hydrothermal method for the synthesis of defective TiO_2 nanocrystals with excellent visible-light photocatalytic activity. *Research on Chemical Intermediates* **2020**, *46*, 2205-2214.
(204) Nathiya, D.; Alhaji, N.; Jahangir, A. M.; Fathima, M. I.; Gatasheh, M. K.; Hatamleh, A. A.; Zehra, S.; Ayeshamariam, A. Synthesis and characterization of $ZnGa_2O_4$ composites and its photocatalytic properties for energy applications. *Environmental Research* **2022**, *204*, 112073.
(205) Li, Z.; Li, B.; Liu, Z.; Li, D.; Ge, C.; Fang, Y. Controlled synthesis of $ZnGa_2O_4$ nanorod arrays from hexagonal ZnO microdishes and their photocatalytic activity on the degradation of RhB. *RSC Advances* **2014**, *4* (89), 48590-48595.
(206) Ratcliff, L. E.; Oshima, T.; Nippert, F.; Janzen, B. M.; Kluth, E.; Goldhahn, R.; Feneberg, M.; Mazzolini, P.; Bierwagen, O.; Wouters, C. Tackling Disorder in γ-Ga_2O_3. *Advanced Materials* **2022**, *34* (37), 2204217.
(207) Kurmaev, E.; Wilks, R.; Moewes, A.; Finkelstein, L.; Shamin, S.; Kuneš, J. Oxygen x-ray emission and absorption spectra as a probe of the electronic structure of strongly

correlated oxides. *Physical Review B—Condensed Matter and Materials Physics* **2008**, *77* (16), 165127.
(208) Archana, K. J.; Preetha, A. C.; Balasubramanian, K. Influence of Urbach energy in enhanced photocatalytic activity of Cu doped ZnO nanoparticles. *Optical Materials* **2022**, *127*, 112245.
(209) Pearton, S.; Yang, J.; Cary, P. H.; Ren, F.; Kim, J.; Tadjer, M. J.; Mastro, M. A. A review of Ga_2O_3 materials, processing, and devices. *Applied Physics Reviews* **2018**, *5* (1).
(210) Wang, Y.; Dickens, P. T.; Varley, J. B.; Ni, X.; Lotubai, E.; Sprawls, S.; Liu, F.; Lordi, V.; Krishnamoorthy, S.; Blair, S. Incident wavelength and polarization dependence of spectral shifts in β-Ga_2O_3 UV photoluminescence. *Scientific reports* **2018**, *8* (1), 18075.
(211) Zhang, Y.; Tang, T.-T.; Girit, C.; Hao, Z.; Martin, M. C.; Zettl, A.; Crommie, M. F.; Shen, Y. R.; Wang, F. Direct observation of a widely tunable bandgap in bilayer graphene. *Nature* **2009**, *459* (7248), 820-823.
(212) Zhang, F.; Saito, K.; Tanaka, T.; Nishio, M.; Arita, M.; Guo, Q. Wide bandgap engineering of $(AlGa)_2O_3$ films. *Applied Physics Letters* **2014**, *105* (16).
(213) Bhuiyan, A.; Feng, Z.; Johnson, J. M.; Huang, H.-L.; Hwang, J.; Zhao, H. MOCVD growth of β-phase $(Al_xGa_{1-x})_2O_3$ on $(\bar{2}01)$ β-Ga_2O_3 substrates. *Applied Physics Letters* **2020**, *117* (14).
(214) Dobosz, A.; Daeneke, T.; Zavabeti, A.; Zhang, B. Y.; Orrell-Trigg, R.; Kalantar-Zadeh, K.; Wójcik, A.; Maziarz, W.; Gancarz, T. Investigation of the surface of Ga–Sn–Zn eutectic alloy by the characterisation of oxide nanofilms obtained by the touch-printing method. *Nanomaterials* **2019**, *9* (2), 235.
(215) Ghasemian, M. B.; Zavabeti, A.; Allioux, F. M.; Sharma, P.; Mousavi, M.; Rahim, M. A.; Khayyam Nekouei, R.; Tang, J.; Christofferson, A. J.; Meftahi, N. Liquid Metal Doping Induced Asymmetry in Two-Dimensional Metal Oxides. *Small* **2024**, 2309924.
(216) Jayaganthan, R.; Hajra, J. Thermodynamics and phase equilibria in the AlGa system. *Materials Science and Engineering: B* **1996**, *38* (1-2), 96-102.
(217) Wakabayashi, R.; Hattori, M.; Yoshimatsu, K.; Horiba, K.; Kumigashira, H.; Ohtomo, A. Band alignment at β-$(Al_xGa_{1-x})_2O_3$/β-Ga_2O_3 (100) interface fabricated by pulsed-laser deposition. *Applied Physics Letters* **2018**, *112* (23).
(218) Wang, T.; Li, W.; Ni, C.; Janotti, A. Band gap and band offset of Ga_2O_3 and $(Al_xGa_{1-x})_2O_3$ alloys. *Physical Review Applied* **2018**, *10* (1), 011003.
(219) Uddin Bhuiyan, A.; Meng, L.; Huang, H.-L.; Sarker, J.; Chae, C.; Mazumder, B.; Hwang, J.; Zhao, H. Metalorganic chemical vapor deposition of β-$(Al_xGa_{1-x})_2O_3$ thin films on (001) β-Ga_2O_3 substrates. *APL Materials* **2023**, *11* (4).
(220) Vural, S.; Sari, Ö. Synthesis and characterization of SDS assistant α-alumina structures and investigation of the effect of the calcination time on the morphology. *Colloid and Polymer Science* **2019**, *297*, 107-114.
(221) Li, J.; Chen, X.; Ma, T.; Cui, X.; Ren, F.-F.; Gu, S.; Zhang, R.; Zheng, Y.; Ringer, S. P.; Fu, L. Identification and modulation of electronic band structures of single-phase β-$(Al_xGa_{1-x})_2O_3$ alloys grown by laser molecular beam epitaxy. *Applied Physics Letters* **2018**, *113* (4).
(222) Mi, W.; Li, X.; Ding, Y.; Wang, D.; Xu, M.; Xiao, L.; Zhang, X.; Chen, X.; Li, B.; Luo, L. Effects of seed layer thickness and post-annealing process on crystalline quality of β-Ga_2O_3 films prepared on Si (100) substrate by RF magnetron sputtering. *Vacuum* **2023**, *214*, 112235.
(223) Tang, X.; Li, K.-H.; Liao, C.-H.; Zheng, D.; Liu, C.; Lin, R.; Xiao, N.; Krishna, S.; Tauboada, J.; Li, X. Epitaxial growth of β-Ga_2O_3 (-201) thin film on four-fold symmetry

CeO_2 (001) substrate for heterogeneous integrations. *Journal of Materials Chemistry C* **2021**, *9* (44), 15868-15876.
(224) Syed, N.; Zavabeti, A.; Messalea, K. A.; Della Gaspera, E.; Elbourne, A.; Jannat, A.; Mohiuddin, M.; Zhang, B. Y.; Zheng, G.; Wang, L. Wafer-sized ultrathin gallium and indium nitride nanosheets through the ammonolysis of liquid metal derived oxides. *Journal of the American Chemical Society* **2018**, *141* (1), 104-108.
(225) Lizarbe, A. J.; Major, G. H.; Fernandez, V.; Fairley, N.; Linford, M. R. Insight note: X-ray photoelectron spectroscopy (XPS) peak fitting of the Al 2p peak from electrically isolated aluminum foil with an oxide layer. *Surface and Interface Analysis* **2023**, *55* (9), 651-657.
(226) Kumar, N.; Biswas, K. Cryomilling: An environment friendly approach of preparation large quantity ultra refined pure aluminium nanoparticles. *Journal of Materials Research and Technology* **2019**, *8* (1), 63-74.
(227) Goff, A.; Aukarasereenont, P.; Nguyen, C. K.; Grant, R.; Syed, N.; Zavabeti, A.; Elbourne, A.; Daeneke, T. An exploration into two-dimensional metal oxides, and other 2D materials, synthesised via liquid metal printing and transfer techniques. *Dalton Transactions* **2021**, *50* (22), 7513-7526.
(228) Zavabeti, A.; Aukarasereenont, P.; Tuohey, H.; Syed, N.; Jannat, A.; Elbourne, A.; Messalea, K. A.; Zhang, B. Y.; Murdoch, B. J.; Partridge, J. G. High-mobility p-type semiconducting two-dimensional β-TeO_2. *Nature Electronics* **2021**, *4* (4), 277-283.
(229) Tourtin, F.; Armand, P.; Ibanez, A.; Tourillon, G.; Philippot, E. Gallium phosphate thin solid films: structural and chemical determination of the oxygen surroundings by XANES and XPS. *Thin Solid Films* **1998**, *322* (1-2), 85-92.
(230) Wang, Z.; Li, C.; Liu, L.; Sham, T.-K. Electronic Structures and Optical Properties of α-Al2O3Nanowires. 2013, IOP Publishing: Vol. 430, p 012065.
(231) Hu, Y. F.; Xu, R. K.; Dynes, J. J.; Blyth, R. I. R.; Yu, G.; Kozak, L. M.; Huang, P. M. Coordination nature of aluminum (oxy) hydroxides formed under the influence of tannic acid studied by X-ray absorption spectroscopy. *Geochimica et Cosmochimica Acta* **2008**, *72* (8), 1959-1969.
(232) Wang, Z.; Li, C.; Liu, L.; Sham, T.-K. Probing defect emissions in bulk, micro-and nano-sized α-Al2O3 via X-ray excited optical luminescence. *The Journal of Chemical Physics* **2013**, *138* (8).
(233) Cabaret, D.; Brouder, C. Origin of the pre-edge structure at the Al K-edge: The role of atomic vibrations. In *Journal of Physics: Conference Series*, 2009; IOP Publishing: Vol. 190, p 012003.
(234) Liu, F.; Li, Y.; Cheng, H.; Jin, C.; Liu, C. Structural, Optical, and Electronic Properties of Epitaxial β-$(Al_xGa_{1-x})_2O_3$ Films for Optoelectronic Devices. *Advanced Optical Materials* **2024**, *12* (21), 2400724.
(235) Bhuiyan, A.; Feng, Z.; Johnson, J. M.; Huang, H.-L.; Hwang, J.; Zhao, H. Band offsets of (100) β-$(Al_xGa_{1-x})_2O_3$/β-Ga_2O_3 heterointerfaces grown via MOCVD. *Applied Physics Letters* **2020**, *117* (25).
(236) Singh, M.; Zakria, M.; Pannu, A. S.; Sonar, P.; Smith, C.; Mahasivam, S.; Ramanathan, R.; Tran, K.; Tawfik, S.; Murdoch, B. J. Defect-Free, Few-Atomic-Layer Thin ZnO Nanosheets with Superior Excitonic Properties for Optoelectronic Devices. *ACS nano* **2024**, *18* (26), 16947-16957.
(237) Baddorf, A. P. Identifying the secondary electron cutoff in ultraviolet photoemission spectra for work function measurements of non-ideal surfaces. *Scientific Reports* **2023**, *13* (1), 13452.

(238) Irvine, C. P.; Stopic, A.; Westerhausen, M. T.; Phillips, M. R.; Ton-That, C. Enhancement of excitonic and defect-related luminescence in neutron transmutation doped β-Ga_2O_3. *Physical Review Materials* **2022**, *6* (11), 114603.
(239) Salih, A. K.; Fiedler, S.; Irvine, C. P.; Matar, F.; Phillips, M. R.; Ton-That, C. Defect passivation and enhanced UV emission in β-Ga_2O_3 via remote fluorine plasma treatment. *Applied Surface Science* **2025**, *687*, 162250.
(240) Milisavljevic, I.; Wu, Y. Fabrication of tunable bandgap epitaxial β-$(Al_xGa_{1-x})_2O_3$ films using a spin-coating method. *International Journal of Applied Ceramic Technology* **2023**, *20* (2), 725-734.
(241) Frodason, Y. K.; Johansen, K.; Vines, L.; Varley, J. Self-trapped hole and impurity-related broad luminescence in β-Ga2O3. *Journal of Applied Physics* **2020**, *127* (7).
(242) Pavesi, L.; Guzzi, M. Photoluminescence of Al x Ga1− x As alloys. *Journal of Applied Physics* **1994**, *75* (10), 4779-4842.